CRUSH SIMULATION AND EXPERIMENTAL MODEL VALIDATION FOR LAMINATED COMPOSITE STRUCTURES

by

Vaughan Allen Thomson

Submitted in fulfillment of the academic requirements for the degree of

Master of Science
in
Engineering

at

The University of KwaZulu-Natal
School of Mechanical Engineering

Supervisor: Prof. E.V.Morozov

Durban, South Africa

December 2004

This work is dedicated to the memory of

Norman Richard Thomson
1945 - 1999

In the well known words of Matt Groening

'You're damned if you do and you're damned if you don't.'
- Bart Simpson

Acknowledgements

Gratitude to those whose contributions have been instrumental in the realisation of this manuscript must firstly be expressed to my supervisor Professor Evgeny Morozov, without whose assistance, encouragement and guidance this research work would never have been possible.

Thanks are also due to Dr Chris von Klemperer whose technical advice and laboratory assistance aided the development of experimental work, as well as Graham Kidson (*Durban Institute of Technology*) – 'got to love those strain amplifiers'.

Thanks also to Professor Gerald Nurick, Dr Trevor Cloete, Ross Hartley and Neville Jacob from the University of Cape Town, *Blast Impact and Survivability Research Unit* for their assistance with high strain rate testing and the *National Research Foundation* for their financial support. Finally, thumbs up to workshop manager Mike Smith, School of Mechanical Engineering staff, fellow postgrads and 'the man upstairs' who always hears my prayers.

Preface

The author hereby declares this dissertation to be his own unaided work except where due acknowledgement is made to others. This dissertation is submitted for the degree of Master of Science in Engineering to the University of KwaZulu-Natal, Durban and has not been submitted previously for any other degree or examination.

Abstract

The primary aim of this study is to develop a modelling approach useful for modelling the response of thin-walled fibre reinforced composite components (particularly laminates) to crushing loads, with the overall direction being towards a reliable methodology for modelling crash scenarios involving composite structures. As such, experimental work is completed in order to characterise the material being studied, as well as to obtain physical data for the crushing of a composite component. The results of numerical modelling are compared with the experimental data in order to evaluate the performance of the implemented models.

A review of published literature for the progressive damage modelling of laminated composite materials provides the background for selection of a material model for modelling the real behaviour of the elementary ply of the laminated material. This model is to be implemented into a Finite Element code using a material characterisation process that is based on the material's experimentally recorded behaviour. Experimentation to investigate the effect of variations in reinforcement orientation and distribution on the crush response of a composite demonstrator component is also undertaken. This experimentally recorded data provides information on the physical response of a real composite component under varied load cases and with varied internal structure. Capturing of data in this way provides a wider scope of physical data for comparison with the predictions of the simulation algorithm and opens the door for further developments aimed at optimising a component's crash response through manipulation of internal structure.

Simulation of the demonstrator component's response to a constant velocity crushing load shows the predictions resulting from the underlying modelling methodology and comparison of the predicted response with the data recorded from physical testing provides a basis for evaluating the performance of the models, as applied. With a known level of confidence provided through the experimental validation program, modelling of the demonstrator's response to impact loading conditions provides predictions of the demonstrator crash response.

CONTENTS

List of Figures

List of Tables

CHAPTER 1

INTRODUCTION

The work presented here is a study into the response of laminated Fibre Reinforced Polymer (FRP) composite components to crushing loads and is geared towards the design of composite components subjected to this type of loading. The study originates from an investigation into the crashworthiness of composite automotive structures and aims to develop algorithms for the simulation of composite components' response to crushing loads, so that designers may have a reliable approach for the virtual prototyping of structures that are subjected to this kind of loading. Validation of the work for crashworthiness applications (which also includes such areas as aerospace, motorsport and boating) requires investigation into cases of impact, involving increased rates of loading that result in high rates of strain in the material.

The general crashworthiness design of a complete structure would involve a complex analysis considering the response of a combination of structural members, generally including metal and composite components subjected to different modes of deformation. The energy absorbed during the destruction of each structural member/component then depends upon the mode of deformation and the material used for its construction. Attention for vehicle crashworthiness studies is directed towards passenger safety during an impact event. In structural terms this translates to design of a structure that will deform sufficiently to prevent large transfers of momentum to the vehicle occupant, whilst limiting excessive deformation so that a survival space exists which prevents harmful crushing of the vehicle occupant(s). A distinct advantage of the fibre composites over metals (and other isotropic materials) lies in their high specific strength which allows for their inclusion (in impact prone structures) as lightweight crash absorbing members. Manipulation of the load response for composite components can also be achieved, by controlling the fibre orientations and fibre distribution over the component.

This investigation focuses on modelling the crushing (and impact) response of individual composite components and aims to demonstrate a feasible modelling methodology for such cases. Once the composite component modelling methodology can be validated, through concurrent experimental work, the confidence level for integration of the modelling approach into the solution of the more general crashworthiness problem is increased. Modelling of the components' load response is accomplished using Finite Element Modelling (FEM) techniques and the performance of the instituted models is to be evaluated against experimental data (which the instituted models are meant to simulate). A review of available approaches for the progressive damage modelling of laminated composites provides the background for selection of a suitable material model and already implemented models used to predict the impact response of laminated structures (particularly for crashworthiness studies) drive the selection of the modelling approach to be taken here. A particular challenge faced when trying to predict the behaviour of composite structures subject to large deformations (as is the case in crashworthiness applications), is to capture the effect of the material micromechanical behaviour on the macroscopic structural response over the full load range.

1.1 Progressive damage modelling of laminates

Modelling the crush response of composite components requires prediction of the material's response right up to the point of ultimate failure. To this end, composite materials under load generally experience internal material failure before any change in the material macroscopic appearance (and response) is observed. Different modes of internal failure have been identified and accepted for fibre composite materials (e.g. Agarawal and Broutman, 1990) with the prevalence of any failure mode under a given loading being dependant upon the direction and nature of loading at the infinitesimal material level. The four accepted modes of failure are:

(i) matrix microcracking
(ii) fibre/matrix debonding
(iii) fibre breaking
(iv) delamination

The progressive nature of composite failure leads to the progressive damage modelling for composite materials in order to predict the material and structural response over large displacements. Progressive damage modelling of fibre composite materials is integrated into mathematical models using continuum damage mechanics (CDM) as a basis and various approaches have been developed (and implemented) in order to capture the effect of the progressive internal material failures on the overall material macroscopic response. In order to model the behaviour of a laminate (made up of a number of plies) damage must be applied at the material ply level since stresses vary from one ply to the next. The ply is then either considered as a whole (Ladeveze and Le Dantec, 1992) or the fibre and matrix behaviours are considered separately and then combined to give the ply behaviour (Haug and De Rouvray, 1992).

The Ladeveze model accounts for matrix microcracking and fibre/matrix debonding using continuum damage mechanics theory. Damage is implemented by a reduction in the material stiffness expressed as:

$$E = E_0(1-d) \tag{1.1}$$

where E_0 is the initial modulus, E the damaged modulus and d the damage parameter lying in the range $0 \le d \le 1$. Separate damage parameters are introduced for stiffness reduction in the principal fibre directions and for in-plane shear, with damage evolution functions used to describe the damage development in terms of damage energy release rates. A critical damage energy release rate is set for values greater than which the composite is considered fully damaged ($d = 1$). Limit strains are used to indicate fibre breakage and a plasticity model is also introduced to account for material plastic strain.

Work presented by Ladeveze and Le Dantec (1992) demonstrates the application of the model to two different carbon fibre reinforced epoxy systems and the model predictions are compared with tension tests for several laminate stacking sequences. Comparison is also made with the results obtained using classical laminate theory (CLT) with failure defined via a Tsai-Hill failure criterion. The results obtained using the Ladeveze elementary ply damage model show improved correlation with the experimental results (when compared with the predictions of the CLT model). The model is developed based on a unidirectional elementary ply and conditions are imposed on the damage propagation in order to capture experimentally observed phenomena for unidirectional materials.

Johnson et al. (2001) extended the Ladeveze model to include delamination effects by describing a contact sliding interface condition between the elementary plies. Development of this model is for a fabric reinforced ply modelled as a homogeneous orthotropic elastic or

elastic-plastic material. A mixed mode delamination failure condition is used to encompass tensile and shear delamination failures at the sliding interface. Validation of the model was accomplished through comparison with experimental observations for the ballistic impact of simply supported carbon fabric/epoxy plates and, later for the ballistic impact of glass fabric/epoxy cylindrical shells (Johnson and Holzapfel, 2002). Both the Ladeveze and the extended model were implemented in the commercially available PAM-CRASH code.

Yen et al. (Materials Sciences Corporation) employ Hashin failure functions (Hashin, 1980) to predict fibre and matrix failure modes at the ply level. The model accounts for delamination effects and was employed in the simulation of the low energy ballistic impact of a unidirectional laminated cylindrical shell. The work presented shows good correlation between load time histories obtained from simulation and experiment and illustrates how the inclusion of fibre damage improves the agreement with experimental results. The algorithm was implemented under a user defined sub-routine in the commercial LS-DYNA code and is essentially a linear elastic model with separate failure criteria for different failure modes. Stiffness reduction is applied for fibres in compression so that a residual load may be supported after the compressive axial strength is exceeded.

The bi-phase model was introduced for the crashworthiness studies of automotive components (Haug and De Rouvray, 1992) and uses the measured elastic properties of a unidirectional ply, together with the known fibre properties and fibre volume fraction, to deduce the orthotropic elastic properties of the matrix material minus the fibres. The elementary layer is then described by two components: a one dimensional (fibre) phase and an orthotropic (matrix) phase. Modulus damage is implemented as for the Ladeveze model (Eq. (1.1)) with damage defined seperately for the separate material phases. Damage at any given time is the sum of volumetric damage, due to a volumetric equivalent strain measure, and shear damage, due to a shear equivalent strain measure. The model also allows for separate definition of tensile and compressive behaviour in the principal material directions.

Haug and De Rouvray (1992) outline how the bi-phase material model may be applied in one of two ways, firstly by using two material phases as in the classical case, or, secondly, by using the orthotropic 'matrix' alone to represent an homogenised fibre/resin system (modified case). The classical approach is deemed well suited to unidirectional plies, whereas the modified approach is recommended when modelling fabric plies or a pair of cross plies within one shell layer. Validation of the model was performed for composite automotive sub assemblies, which included the modelling of sandwich constructions. The work was extended for the predictive crashworthiness modelling of a full composite car cabin, for the cases of full frontal and pole side impacts. Through comparison with experimental results, the authors conclude that the crash simulation code PAM-CRASH can be used as a design aid for the conception of new composite structures at a feasible level, when augmented with the options for composite crashworthiness simulation.

The work of Coutellier and Rozycki (2000) concerns the use of both the Ladeveze and bi-phase models for the simulation of metal/fibre-epoxy composite plates subjected to dynamic bending and metal/fibre-epoxy tubes under axial compression. In order to describe the metal/composite construction, a multi-layered multi-material finite element is employed in the PAM-CRASH code. Agreement within 12% of critical experimental forces, displacements and times was obtained for simulations employing both the bi-phase and Ladeveze models.

1.2 Crashworthiness of thin-walled composite structures

The survey of available literature pertaining to the progressive damage modelling of laminates already highlights some investigations into the crashworthiness of thin-walled composite components. Haug and De Rouvray (1992) investigate the crashworthiness of a full composite

car cabin employing the bi-phase progressive damage model, whereas other investigators (Johnson et al., 2001; Yen et al. of Matls Sciences Corp.; Coutellier and Rozycki; 2001) employ progressive damage models for the modelling of laminated composite structures response to impact loading. For application of the respective models, the commercial FE codes PAM-CRASH and LS-DYNA have been employed. Modelling using the LS-DYNA code was accomplished using user defined material models, whereas a significant effort has been exercised into incorporation of suitable material models into the primary PAM-CRASH code.

Other studies involving the crashworthiness of thin-walled composite components are presented by Hamada (1997), Bravo et al. (1993), Savona et al. (2001) and Dehn et al. (1999). The work of Hamada (1997) investigates the use of braided composite I-beams as effective crash absorbing elements for automotive crashworthiness. A useful comparison of the energy absorbing performance of composite tubes under various boundary conditions (including changes in temperature, moisture level and weathering) is provided. The author concludes that braided I-beams can be used effectively for impact energy absorption under vehicle lateral and frontal collisions. Bravo et al. (1993) consider a combination of transverse shear, lamina bending and local buckling effects on the crash energy absorption of a glass fabric/epoxy composite tube. The FE codes LS-DYNA3D and ABAQUS/Explicit were employed to model the crushing of the tube and the authors report good agreement between theory and experiment. The work of Savona et al. (2001) and Dehn et al. (1999) are experimental investigations into the crash energy absorption of composite tubes, with a number of similar experimental studies having been earlier produced (Schmueser and Wickliffe, 1987; Hull, 1983; Berry and Hull, 1984). Capello and Nigrelli (2001) employ a user built FE model, in the explicit LS-DYNA3D code, to predict the impact response of a racing car composite nose cone. Comparison of critical displacements and forces obtained from experiment and simulation show good agreement. It is, however, not clear what material model was employed for simulation of the composite nose cone.

In general, the survey of available literature pertaining to the crashworthiness of composite components shows substantial investigative effort devoted to the triggering and sustaining of energy absorbing axial crushing modes for tubular crash absorbing devices. In these cases the importance of maintaining a localised crush zone (involving energy absorption through a combination of fiber breaking, fibre splitting, frond formation, matrix cracking and delamination - without the prevalence of buckling and bending collapse modes) is highlighted. Haug and De Rouvray (1992) suggest the use of alternative failure modes that are more easily triggered and controlled, such as membrane tearing modes. Their work was focused rather on the prediction of composite components response to impact loads, where the crushing failure is dominated by bending and tearing of the composite walls. This is of significant practical importance for the design of impact prone structural components which are not special energy absorbing devices. Using this kind of approach, the energy absorbing performance of the structure can be improved, with the components failing in a predictable and repeatable way.

For model implementation, the commercial FE codes, PAM-CRASH, LS-DYNA3D and ABAQUS/Explicit have all been employed to predict the impact response of composite structures. Although the studies employing LS-DYNA3D and ABAQUS/Explicit indicate good agreement between experimental and simulated data, not all of the publications clarify the material models employed. Published work involving application of LS-DYNA3D and ABAQUS all involve the use of user defined models whereas a substantial amount of work has been conducted to incorporate experimentally validated progressive damage models for composite materials into the primary PAM-CRASH code.

1.3 Modelling the crash behaviour of laminated structures

It was already pointed out that a significant amount of research effort has been dedicated to studying the energy absorption for the axial crushing of composite structures, typically with tubular cross section (Schmueser and Wickliffe, 1987; Hull, 1983; Berry and Hull, 1984; Savona et al., 2001; Dehn et al., 1999). The work of Mamalis et al. (1998) is a comprehensive experimental overview of the axial crushing and bending collapse of composite tubes of varied cross-sectional shape. The attention to this area of research is driven by the ability of the composites to absorb a greater amount of energy per unit mass under controlled progressive axial crushing. The collapse of a thin-walled structural component under crushing type impact loads, on the other hand, occurs due to a combination of bending and tearing of the structural shell as crushing progresses and may include cases of local and global buckling. For the general crash of a complete vehicular structure, a complex combination of axial and bending collapse will occur depending upon the nature of the collision (e.g.: head on, side impact or an offset collision) and the orientation of the various sub-structures to the impact loads. Following the work of Haug and De Rouvray (1992), the work here aims to predict the composite structural component's response to impact loads, dominated by bending and membrane loading of the thin-walled structure.

The critical areas of work that must be addressed for implementation and validation of the modelling methodology are:

Material Characterisation – For this part of the work, the material constants (and other parameters) that are required for implementation of the selected material model must be determined. For accurate characterisation, material coupons representative of the material used in the final components construction are tested. Theoretical predictions and/or published data also present themselves as sources for the required material characterisation parameters.

Material Model Calibration – Following material characterisation, simulation of some simple load cases (such as tensile and compressive tests) verifies that the chosen model and calculated material parameters are representative of the real material's behaviour.

Component Model Validation – Following the testing of a real composite component with an appropriate geometry, simulation of the test is completed using an appropriate FE model that employs the calibrated material description. Comparison of the simulated response with experimental data serves to evaluate the performance of the instituted model and modelling methodology.

Once a significant level of confidence is demonstrated through model validation, the *predictive modelling* of the component's response to alternative load cases can be implemented. Further experimental work can then be used to evaluate the predictive potential of the modelling approach.

Earlier research conducted at the University of Natal (Selvarajalu, 2003; Morozov, 2003) involved the identification of a number of FE codes in order to ascertain their suitability for the analysis of fibre reinforced composites' response to impact loading. The codes examined were LS-DYNA, PAM-CRASH, MSC.DYTRAN, MSC.PATRAN, MSC.MARC, ABAQUS/Explicit and ABAQUS/Standard. Consistent with the trend in impact modelling observed from published literature (§ 1.2), the LS-DYNA and PAM-CRASH codes were shortlisted and some preliminary modelling, involving tensile and bending simulations was performed using both LS-DYNA and PAM-CRASH. From this investigation the PAM-CRASH code was seen to offer a more readily implementable solution to the problem of modelling composite components response to crushing impact loads. On the other hand, an advantage of the LS-DYNA code is that user models are more easily defined, as the option to define specific material behaviour in the LS-DYNA environment is more readily available. However, from the

reviewed literature, the composite material options already available in the PAM-CRASH code have been demonstrated to produce results that are in good agreement with experimentally recorded behaviour. Instead of investing added effort into defining specific user models in an FE code such as LS-DYNA, it is seen as more beneficial, in a practical sense, to test the hypothesis that the available composite material options in the PAM-CRASH code do indeed offer a feasible solution for the virtual prototyping of composite components that are prone to impact loading. It is also sought to develop a practical modelling methodology that allows efficient implementation of finite element models for the virtual prototyping of laminated structures for crashworthiness applications.

Investigation of a component's response to impact loading begins with an investigation into the quasi-static material and component behaviour. The common geometry for quasi-static and impact loading means that the only outstanding feature for cases involving impact is the material response (inertia effects are taken into account by equations of motion). High rates of strain are associated with impact loading and materials may display altered stress-strain behaviour under increasing strain rate. Accounting for the material strain rate effect is usually applied by scaling the materials quasi static curve, based on experimental data obtained from material testing at high rates of strain. This supports an experimental program that firstly addresses the material and component's quasi-static behaviour, following which the program may be extended to incorporate cases of dynamic loading and material characterisation at high rates of strain. The design and manufacture of a suitable demonstrator component is required for implementation of the testing program.

With PAM-CRASH selected as the analysis tool, selection of the material model to be employed is required so that the necessary material characterisation parameters can be identified and obtained. The material models identified in the review of progressive damage models for composites (§ 1.1) that are tailored to suit the PAM-CRASH code are the Ladeveze (or global ply) model (Ladeveze and Le Dantec, 1992), the bi-phase model (Haug and De Rouvray, 1992) and the extended global ply model employed by Johnson and co-workers (Johnson et al., 2001). Fabric reinforcements have been selected for this investigation since they are used in the construction of structural components with complex geometry. The global ply material model includes damage propagation laws that are designed to capture experimentally observed phenomena for unidirectional materials, making the global ply model less suitable for modelling the behaviour of fabric reinforced composites. The extended global ply model, on the other hand, has been developed for modelling of fabric reinforced composites but is yet to be included in the primary PAM-CRASH code (at the time of conception of this study) and is reserved as a possibility for future research. The modified bi-phase model (which treats the ply as an homogenised orthotropic layer) has been identified (§ 1.1) as being suitable for the modelling of fabric reinforced composites and is thus selected for this study.

CHAPTER 2

CRASHWORTHINESS MODELLING

A review of the progressive damage modelling for laminated composites and the application of such models to crashworthiness problems (§ 1) led to the selection of the modified bi-phase model (Haug and De Rouvray, 1992) for the modelling of fabric plies. The simulation of laminated composites' response to crushing loads is to be conducted using the PAM-CRASH finite element code which is tailored to the solution of structural problems involving impact and already contains an implementation of the bi-phase material model. The PAM-CRASH Material Type 130 is an application of the bi-phase model to a multi-layered shell element which is well suited to the modelling of thin-walled laminates. The four noded shell element employed possesses six nodal degrees of freedom and is of the Mindlin-Reissner type (Belytschko et al., 1984), taking transverse shear deformations into account.

2.1 The PAM-CRASH analysis tool

(PAM-Crash Theory Notes, 2000)

The PAM-CRASH code allows for modelling of 3D structures using arbitrary combinations of brick, plate and shell elements, beam and bar elements and discrete elements for description of the structure. For typical crashworthiness simulations plates and shells are used to model thin-walled parts. Beams and bars model structural components such as stiffening frames and suspension members, whereas brick elements are typically used for the modelling of crushable foams.

Application of the finite element method for the solution of a structural response problem leads to discretised, coupled and nonlinear equations of motion in each degree of freedom describing the force response for the structure under investigation. Integration of these equations in the time domain is required for problem solution and this may be completed using implicit or explicit numerical methods. Both methods use time discretisation for solution of the unknown displacements, velocities and accelerations of each degree of freedom at a given discrete point in time (using the known state of the structure at the previous point in time as a starting point). Standard implicit methods (for time integration) require linearisation of the set of nonlinear equations of motion and lead to sets of coupled algebraic equations which must be solved iteratively in order to achieve dynamic equilibrium at a considered point in time. Explicit methods, on the other hand, do not require linearisation and lead to a set of uncoupled algebraic equations. Solution of such systems is trivial and computer time per simulation time step is much less than the computer time needed to solve for large coupled systems of algebraic equations of the implicit methods.

The time increment of explicit methods, however, is restricted for solution stability, while, in principle, the time increment for unconditionally stable implicit methods is not restricted in size. In typical crashworthiness studies (over relatively short durations and involving large distortions of the structural parts) this advantage has no bearing, since the structural states must be known at many discrete points in time in order to allow for an accurate tracking of the complex physical phenomena during crash events (and to account for material and geometrical

nonlinearities). In crashworthiness studies, therefore, the explicit time integration methods have proven computationally advantageous.

An overview of the other basic considerations that must be made when undertaking the numerical simulation of some physical phenomenon are:

	DECISION	OPTIONS
1)	Select analysis level	2D or 3D
2)	Formulate partial differential equations (PDE's) governing the problem	Lagrangian, Eulerian or Arbitrary Lagrange-Euler (ALE)
3)	Discretise the PDE's to obtain a system of ordinary differential equations (ODE's)	finite elements (FE) or finite differences (FD)
4)	Perform a time integration of the differential eqns to obtain the problem solution	explicit or implicit solution
5)	Program the selected procedure	scalar or vectorised and/or multi-tasked

The members of the PAM-CRASH code are mainly used for the dynamic analysis of structures and are defined as three-dimensional (3D), Lagrangian finite element, explicit vectorised/multi-tasked codes for the nonlinear dynamic analysis of structures. The Lagrangian approach refers to the choice of independent variables for the problem. For this formulation, each particle is characterised by its initial conditions and its actual coordinates are functions of the initial conditions and time.

$$x = x(x_0, y_0, z_0, t)$$
$$y = y(x_0, y_0, z_0, t)$$
$$z = z(x_0, y_0, z_0, t)$$

Mesh points coincide with material points in the Lagrangian formulation and thus have time dependant coordinates. This is opposed to the Eulerian formulation, for which particles 'flow' through a stationary (time independant) mesh. An Arbitrary Lagrange Euler (ALE) approach has material 'flowing' through a mesh (Eulerian) which moves according to a user defined pattern (Lagrangian).

2.2 The bi-phase model – PAM-CRASH material 130

(PAM-CRASH Solver Notes, 2000)

The bi-phase model is a heterogeneous material model adapted to unidirectional continuous fibre reinforced composites or composite fabrics (Fig. 2.1). The material stiffness and strength are calculated by superimposing the effects of an orthotropic material phase (matrix minus fibres) and a one dimensional material phase (fibres). Each phase (fibre, matrix) has its own rheological law, e.g., an elastic/brittle orthotropic or micro-fracturing brittle damage law for the matrix phase and a unidirectional elastic-brittle damage law for the fibres.

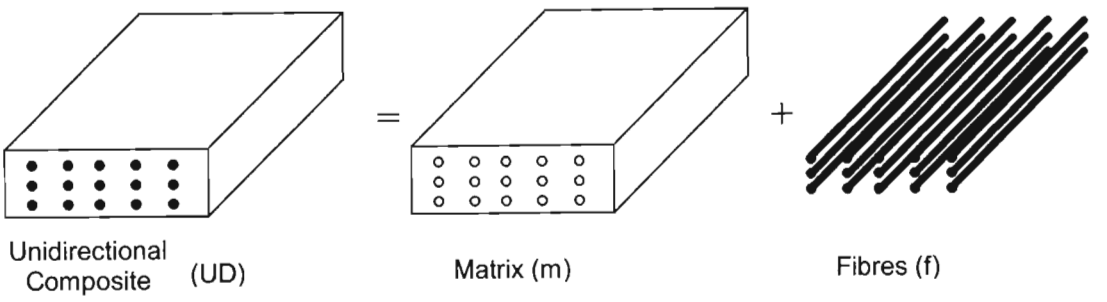

Fig. 2.1 Bi-phase composite model

Orthotropic material law

The stress-strain relation for orthotropic materials is at the foundation of the bi-phase model and is given as:

$$\begin{bmatrix} \varepsilon_{11} \\ \varepsilon_{22} \\ \varepsilon_{33} \\ \\ \varepsilon_{12} \\ \varepsilon_{23} \\ \varepsilon_{13} \end{bmatrix} = \begin{bmatrix} \frac{1}{E_1} & -\frac{\nu_{21}}{E_2} & -\frac{\nu_{31}}{E_3} & & & \\ -\frac{\nu_{12}}{E_1} & \frac{1}{E_2} & -\frac{\nu_{32}}{E_3} & & 0 & \\ -\frac{\nu_{13}}{E_1} & -\frac{\nu_{23}}{E_2} & \frac{1}{E_3} & & & \\ & & & \frac{1}{G_{12}} & 0 & 0 \\ & 0 & & 0 & \frac{1}{G_{23}} & 0 \\ & & & 0 & 0 & \frac{1}{G_{13}} \end{bmatrix} \begin{bmatrix} \sigma_{11} \\ \sigma_{22} \\ \sigma_{33} \\ \\ \sigma_{12} \\ \sigma_{23} \\ \sigma_{13} \end{bmatrix} \tag{2.1}$$

Where the directions 1, 2 and 3 are the directions of material orthotropy and the Poisson's ratio ν_{12} defines the ratio of strain in direction 2 resulting from a unit strain in direction 1. The remaining Poisson's ratios (ν_{23}, ν_{13}) follow the same rule and E_1, E_2, E_3, G_{12}, G_{23} and G_{13} are the material elastic moduli. For a laminated shell, orthotropy directions are defined in the plane of the shell element, with the 1-axis coinciding with the fibre direction (warp direction for fabric plies), the 2-axis being perpendicular to this (within the plane of the ply) and the 3-axis pointing normal to the plane of the ply. The material parameters are defined with respect to this natural system of orthotropy (principal material directions).

Elastic behaviour

For the bi-phase model, the elastic constants E_1, E_2, E_3, G_{12}, G_{23} and G_{13} are the properties of the orthotropic material obtained after subtracting the influence of the fibres, which are considered only to influence the composite in one direction (the fibre direction). As outlined by Haug and De Rouvray (1992) and reviewed in § 1.1, 'Using the bi-phase material model, the orthotropic character of the cloth and of the unidirectional composite layers of a stackup can be modelled in two principal ways: either using two material phases, namely fibres plus matrix ('classical' model), or using one material phase, namely an orthotropic matrix only ('modified' model). In the first approach ('classical bi-phase model) the material orthotropicity is represented primarily by the fibre phase. In the second case ('modified' bi-phase model) the orthotropic character of the fibre reinforced material is represented by the suitably specified orthotropic constants of only the 'matrix' material, and no fibre properties need be specified. The first approach is usually more suited to represent unidirectional composite plies, while the second approach may be more convenient to represent, for example, cloth layers or a pair of cross-plies within one shell layer'. Using the 'modified' approach, the material is modelled as a

single orthotropic layer and separate fibre and matrix properties need not be specified (see Degenerate bi-phase models, below).

When using the 'classical' approach, the orthotropic matrix parameters can be deduced from the measured unidirectional composite properties (UD). For the particular case of a transversely orthotropic material, the following relationships are obtained (PAM-CRASH Solver Notes, 2000).

Known or measured unidirectional ply properties:

E_1^{UD}, E_2^{UD}, G_{12}^{UD}, ν_{12}^{UD} = in-plane material constants

E_{true}^{f} = true fibre modulus

α_f = fibre volume fraction

Calculated quantities:

$$\nu_{21}^{UD} = \nu_{12}^{UD} E_2^{UD} / E_1^{UD}$$

$$N^{UD} = 1 - \nu_{12}^{UD} \nu_{21}^{UD}$$

$$E_1^f = \alpha_f E_{true}^f$$

For the bi-phase model, the material stiffness matrices are given by:

$$\mathbf{C}^{UD} = \mathbf{C}^{f} + \mathbf{C}^{m} \tag{2.2}$$

Where

$$C^{UD} = \begin{bmatrix} E_1^{UD}/N^{UD} & E_2^{UD}\nu_{12}^{UD}/N^{UD} & 0 \\ E_1^{UD}\nu_{21}^{UD}/N^{UD} & E_2^{UD}/N^{UD} & 0 \\ 0 & 0 & G_{12}^{UD} \end{bmatrix}$$

$$C^{f} = \begin{bmatrix} E_1^f & 0 & 0 \\ 0 & 0 & 0 \\ 0 & 0 & 0 \end{bmatrix} \tag{2.3}$$

$$C^{m} = \begin{bmatrix} E_1^m/N^m & E_2^m\nu_{12}^m/N^m & 0 \\ E_1^m\nu_{21}^m/N^m & E_2^m/N^m & 0 \\ 0 & 0 & G_{12}^m \end{bmatrix}$$

and

$$N^m = 1 - \nu_{12}^m \nu_{21}^m$$

Solution for the unknown matrix phase constants is obtained from Eq. (2.2)

$$\mathbf{C}^{m} = \mathbf{C}^{UD} - \mathbf{C}^{f}$$

Giving

$$E_1 = E_1^m = E_1^{UD} - E_1^f$$

$$E_2 = E_2^m = \frac{E_2^{UD}}{1 + (\nu_{12}^{UD})^2 \left(E_2^{UD} / E_1^{UD}\right)\left(E_1^f / \left(E_1^{UD} - E_1^f\right)\right)}$$

$$\nu_{12} = \nu_{12}^m = \nu_{12}^{UD} \tag{2.4}$$

$$\nu_{21} = \nu_{21}^m = \frac{\nu_{21}^{UD}}{\left(1 - E_1^f N^{UD} / E_1^{UD}\right)}$$

$$G_{12} = G_{12}^m = G_{12}^{UD}$$

Tensile and compressive data

Because of different behaviour exhibited by many composites under tensile and compressive loading, the bi-phase model allows for separate definition of material parameters for tension and compression. Even in cases where the composite's elastic behaviour is symmetric the damage behaviour typically is not. For the purpose of modelling, the matrix material is considered to be in tension when the first strain invariant ($\varepsilon_{kk} = \varepsilon_{11} + \varepsilon_{22} + \varepsilon_{33}$) is positive, for which case the material's tensile parameters are used. Fibers are in tension when the strain in the fibre direction, ε_{11}, is positive. Tensile and compressive ultimate values are specified when augmenting a failure criterion to the bi-phase model.

Degenerate bi-phase models

Particularly suited to modelling of fabric reinforced plies (Haug and De Rouvray, 1992), a degenerate bi-phase model obtained by neglecting the fibre phase can be used to model a quasi homogeneous orthotropic material behaviour that can be brittle-elastic or elastic fracturing. If the matrix phase is neglected, the model corresponds to a one dimensional material with non-vanishing properties in the fibre direction only.

Damage behaviour

Damage for the bi-phase model is implemented by a reduction in stiffness, as given by:

$$\mathbf{C}(d) = \mathbf{C}_0 \times (1 - d) \tag{2.5}$$

Where $\mathbf{C}$ is the instantaneous stiffness matrix, $\mathbf{C}_0$ is the initial undamaged stiffness matrix and d is a unitless scalar damage parameter that is a function of strain. As for the material elastic constants, damage for the bi-phase model is defined separately for cases of tension and compression, and may propagate independently for matrix and fibres. Damage is separated into volumetric and shear components as given by

$$d(\varepsilon) = d_v(\varepsilon_v) + d_s(\varepsilon_s) \tag{2.6}$$

where d_v is the volumetric damage, due to a volumetric equivalent strain measure, ε_v, and d_s is a shear induced damage, due to an equivalent shear strain measure, ε_s. The expressions for volumetric and equivalent shear strain (using Einstein's summation convention) are,

$$\begin{aligned} \varepsilon_v &= \varepsilon_{kk} \\ \varepsilon_s &= \left[(1/2) e_{ij} e_{ij}\right]^{1/2}, \text{ with } e_{ij} = \varepsilon_{ij} - (1/3)\varepsilon_{kk}\delta_{ij} \end{aligned} \tag{2.7}$$

Which are expanded as follows:

$$\varepsilon_v = tr(\boldsymbol{\varepsilon}) = tr\begin{bmatrix} \varepsilon_{11} & \varepsilon_{12} & \varepsilon_{13} \\ \varepsilon_{12} & \varepsilon_{22} & \varepsilon_{23} \\ \varepsilon_{13} & \varepsilon_{23} & \varepsilon_{33} \end{bmatrix} = \varepsilon_{11} + \varepsilon_{22} + \varepsilon_{33} \tag{2.8}$$

$$\begin{aligned} \varepsilon_s &= \sqrt{\frac{1}{2} tr\left(\begin{bmatrix} \varepsilon_{11} & \varepsilon_{12} & \varepsilon_{13} \\ \varepsilon_{12} & \varepsilon_{22} & \varepsilon_{23} \\ \varepsilon_{13} & \varepsilon_{23} & \varepsilon_{33} \end{bmatrix} - \frac{1}{3}\begin{bmatrix} tr(\boldsymbol{\varepsilon}) & 0 & 0 \\ 0 & tr(\boldsymbol{\varepsilon}) & 0 \\ 0 & 0 & tr(\boldsymbol{\varepsilon}) \end{bmatrix}\right)^2} \\ &= \sqrt{\frac{1}{3}\left[\left(\varepsilon_{11}^2 + \varepsilon_{22}^2 + \varepsilon_{33}^2 - \varepsilon_{11}\varepsilon_{22} - \varepsilon_{22}\varepsilon_{33} - \varepsilon_{11}\varepsilon_{33}\right) + 3\varepsilon_{12}^2 + 3\varepsilon_{23}^2 + 3\varepsilon_{13}^2\right]} \end{aligned} \tag{2.9}$$

Equivalent strain expressions for the matrix material under uniaxial tension or compression (in the fibre direction) are obtained by making the following substitutions into Eqs (2.8) - (2.9):

$$\begin{aligned} \varepsilon_{22} &= -\nu_{12}\varepsilon_{11} \\ \varepsilon_{33} &= -\nu_{13}\varepsilon_{11} \\ \varepsilon_{12} &= \varepsilon_{23} = \varepsilon_{13} = 0 \end{aligned} \tag{2.10}$$

Giving:

$$\begin{aligned} \varepsilon_v^m &= (1 - \nu_{12} - \nu_{13})\varepsilon_{11} \\ \varepsilon_s^m &= \frac{\varepsilon_{11}}{\sqrt{3}}(1 + \nu_{12} + \nu_{13} - \nu_{12}\nu_{13} + \nu_{12}^2 + \nu_{13}^2)^{1/2} \end{aligned} \tag{2.11}$$

and for the fibre phase (also under uniaxial loading in the fibre direction)

$$\begin{aligned} \varepsilon_v^f &= \varepsilon_{11} \\ \varepsilon_s^f &= 0 \end{aligned} \tag{2.12}$$

Description of the damage functions, $d_v(\varepsilon_v)$ and $d_s(\varepsilon_s)$, is accomplished by choosing three critical damage points from the relevant stress-strain diagram (Fig. 2.2), they are the initial damage point (i), the intermediate damage point (1) and the ultimate damage point (u). The damage function is then assumed to be linearly piecewise between the critical damage points and is subject to the limits $0 \le d \le 1$. These limits on the damage value bound the material stress-strain curve to lie somewhere between the elastic material curve (for that direction of loading) and the zero axis for stress. A material with zero damage follows the elastic material definition and a material with damage equal to unity follows the zero stress axis, since no load can be supported for the fully damaged material (the material stiffness matrix is identically zero). Evolution of damage begins when the initial damage point is passed (measured in terms of strain), since $d = 0$ for $0 \le \varepsilon \le \varepsilon_i$. The damage value then increases linearly over the range $\varepsilon_i \le \varepsilon \le \varepsilon_1$, where damage equals d_1 when strain equals ε_1. Damage continues linearly over the range $\varepsilon_1 \le \varepsilon \le \varepsilon_u$, until the ultimate damage point is reached ($d = d_u$ when $\varepsilon = \varepsilon_u$). For $\varepsilon > \varepsilon_u$, the damage value grows asymptotically from d_u to 1.

Parameters required for the fibre phase are the true fibre modulus, E_{true}^f, fibre volume fraction, α_f, and fibre damage parameters (as described above). When the fabric ply is modelled as a quasi homogeneous layer these values are all set to zero (degenerate bi-phase model). In this

case, as is established from the material law, description of the orthotropic material requires nine independent elastic constants. These are the elastic moduli in the principal material directions (E_1, E_2, E_3), the shear moduli (G_{12}, G_{13}, G_{23}) and the Poisson's ratios (ν_{12}, ν_{13}, ν_{23}), as shown in Table 2.1. The full set of material characterisation parameters required for description of the quasi homogeneous model are shown in Table 2.2, with the parameters entered separately for tensile and compressive characterisation.

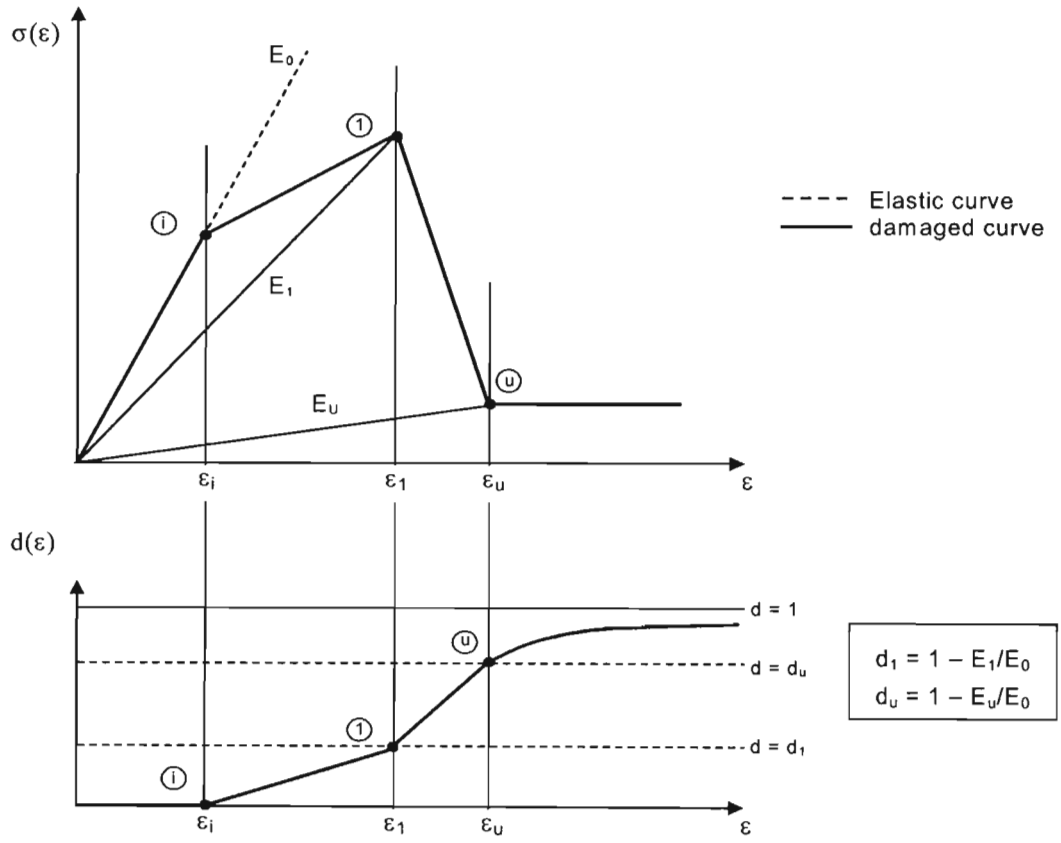

Fig.2.2 Damage description for the bi-phase model

Table 2.1 Nine independent elastic constants to describe orthotropic material

Elastic Moduli	Shear moduli	Poisons Ratios
E_1	G_{12}	ν_{12}
E_2	G_{23}	ν_{23}
E_3	G_{13}	ν_{13}

Table 2.2 Parameters required for fabric ply characterisation (tension and compression)

Material constants			**Damage Parameters**	
Tensile moduli	Shear moduli	Poisons ratios	Critical strains	Damage values
E_1	G_{12}	ν_{12}	ε_i	-
E_2	G_{23}	ν_{23}	ε_1	d_1
E_3	G_{13}	ν_{13}	ε_u	d_u

CHAPTER 3

MATERIAL CHARACTERISATION

Characterisation of a composite requires the experimental testing of suitably designed specimens loaded in a way that will allow determination of important material constants and other parameters necessary for the design procedure. The description of a material's behaviour for crashworthiness modelling requires knowledge of the material response over the complete load range since the material behaviour must be predicted right up to failure. Elastic constants and strengths are the basic mechanical properties of the material and (as established from the material law, Eq. (2.1)) description of three-dimensional orthotropy requires nine independent elastic constants, whereas only four independent elastic constants are required for the special case of two-dimensional orthotropy. The application of the bi-phase model (§ 2.2) for modelling of thin-walled laminates is accomplished in the PAM-CRASH code using a multi-layered 'Mindlin-Reissner' shell element (Belytschko et al., 1984) which takes transverse shear deformations and changes of plate thickness into account. This requires specification of the full set of material characterisation parameters, consisting of nine basic material constants and the material damage parameters for the separate cases of tensile and compressive loading.

Material characterisation for the purpose of this study aims to quantify the modelling parameters necessary for simulation of the demonstrator component (§ 4) which is manufactured using identical plies, employing E-glass fabric 1102 (suppliers *AMT, South Africa*, see Table 3.1(a)) and Ampreg 20 epoxy resin (*SP systems International*, see Table 3.1(b)). The specimens are thus manufactured using the same constituents and processing parameters used to manufacture the demonstrator.

3.1 Tensile characterisation

A discussion of the bi-phase material model has already been provided (§ 2.2) and the set of material characterisation parameters required for implementation of the material model were identified. The parameters E_1, E_2, E_3, G_{12}, G_{13}, G_{23} ν_{12}, ν_{13}, ν_{23}, ε_i, ε_1, ε_u, d_1 and d_u are necessary for both tensile and compressive loadings, requiring testing of laminated specimens in tension and compression. Following is a presentation of the specimens used for tensile testing, the results that were obtained and the calculation process used to quantify the material characterisation parameters.

3.1.1 Tensile testing of laminated specimens

Laminated material specimens are manufactured so that specimens representing the material make-up of the laminated demonstrator component may be tested to failure. For this reason the ply construction and manufacturing process used to manufacture the laminated specimens is chosen to replicate the construction and conditions of prototype manufacture. The specimens are manufactured using a hot vacuum bagging process (Fig. 3.1), operating at the same vacuum pressure, curing time and curing temperature (Table 3.2) that is used for the manufacture of the laminated demonstrator. The tensile specimen geometry is shown in Fig. 3.2 (as per ASTM D3039-76). Specimens are made up of 8 layers of the 2x2 twill weave glass fabric, with

290g/m² surface density (Table 3.1(b)), in combination with an Ampreg 20 epoxy resin system (Table 3.1(a)). Note that the reinforcement is a balanced woven fabric (fibre count and hence orthotropic properties are the same in the 0° and 90 ° directions and are, in fact, symmetrical about the 45° orientation).

Five specimens were prepared (Fig. 3.3) with attached strain gauges (Fig. 3.4) and tested at a loading rate of 2mm/min, using a Lloyds testrig. The destroyed specimens and failures are shown in Figs 3.5 – 3.6 and the resulting stress-strain curves are provided in Fig. 3.7. Measurements for the five specimens are shown in Table 3.3. Poisson's ratio was found by comparison of longitudinal and transverse strain readouts, giving $\nu_{12} = 0.17$.

Table 3.1(a) 1102 glass fabric reinforcement specifications (*AMT, South Africa*)

Fabric Specifications: 1102 E-Glass	
Fibre designation	EC 9 68x3
Fabric weave	2 x 2 twill
Fabric weight	290g/m²
Warp / weft	Balanced - 50% / 50%
Thread count	7
Flexural Modulus **	18000MPa
Flexure Strength **	500MPa
Lamina thickness **	0.29mm

** for 40% fibre volume fraction epoxy laminate

Table 3.1(b) Ampreg 20 epoxy resin specifications (*SP Systems International*)

PROPERTY	UNITS	Value
Tensile strength	(MPa)	75.2
Tensile modulus	(GPa)	3.81
Flexural modulus	(GPa)	2.58
Elongation at break	%	1.7
Density	g/cm^3	1.176

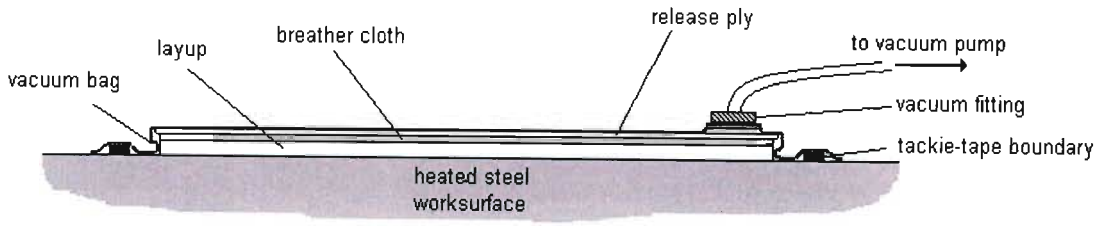

Fig. 3.1 Hot vacuum bagging of the laminated plate specimens

Table 3.2 Parameters for hot processing of Ampreg 20 resin

Ampreg 20 Processing Parameters	
Cure temperature:	70 °C
Cure time:	35 min
Vacuum pressure:	0.8 bar

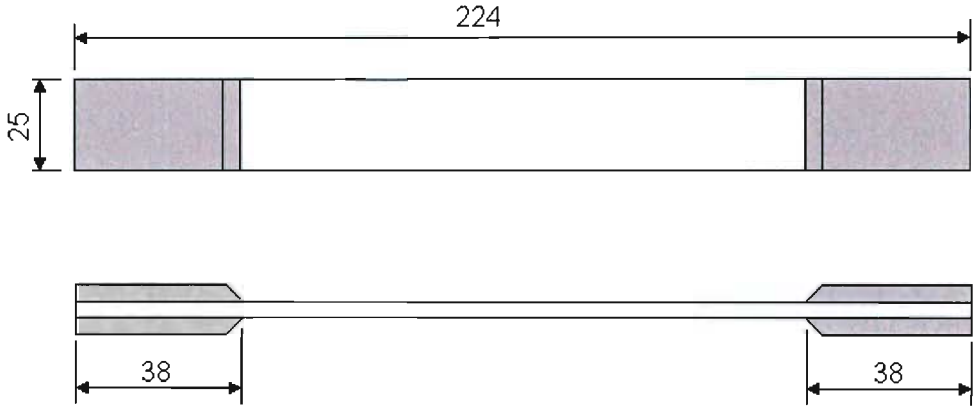

Fig. 3.2 Laminated specimen geometry (mm)

Table 3.3 Laminated tension specimen measurements

Specimen #	width (mm)	thickness (mm)	UTS (MPa)	Ultimate Strain -
Lam01	24.50	2.40	300	0.0192
Lam02	24.45	2.30	286	0.0188
Lam03	24.40	2.45	281	0.0175
Lam04	24.50	2.40	273	0.0186
Lam05	24.55	2.40	235	0.0138

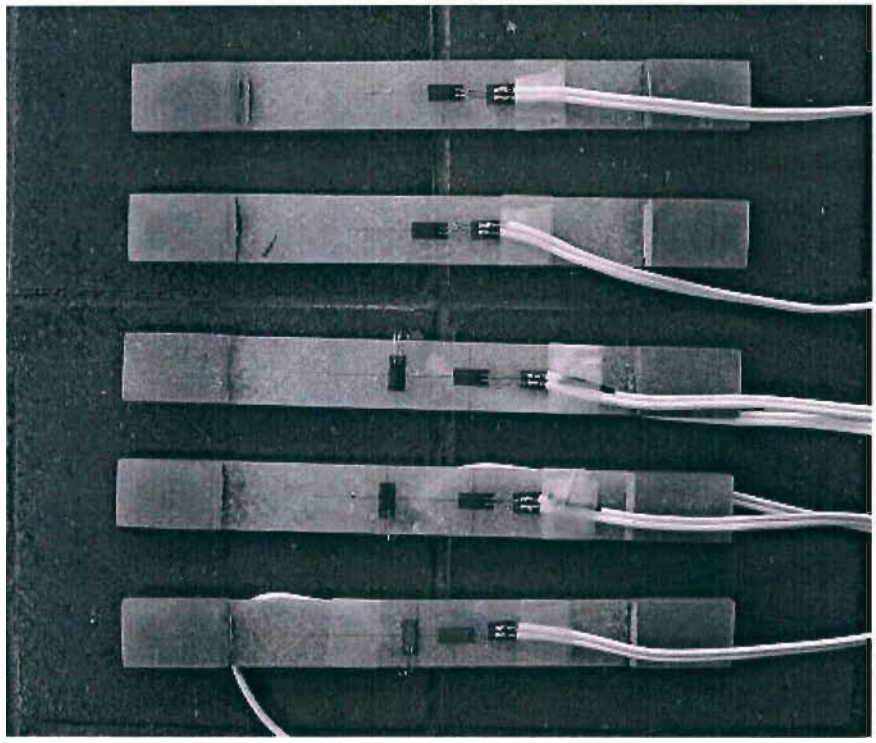

(a) Before testing

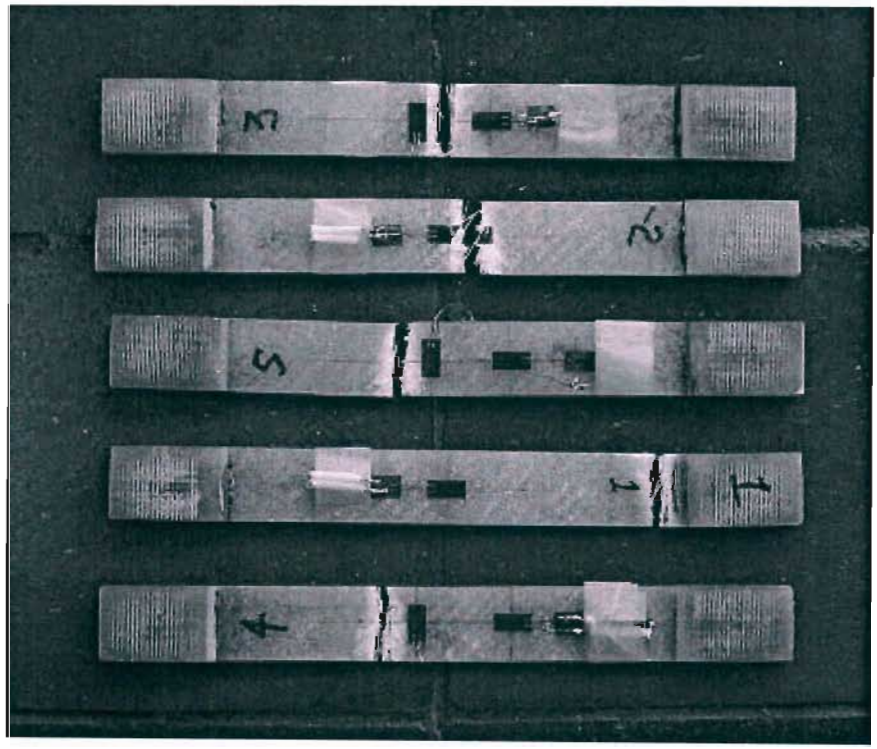

(b) After testing

Fig. 3.3 Laminated specimens

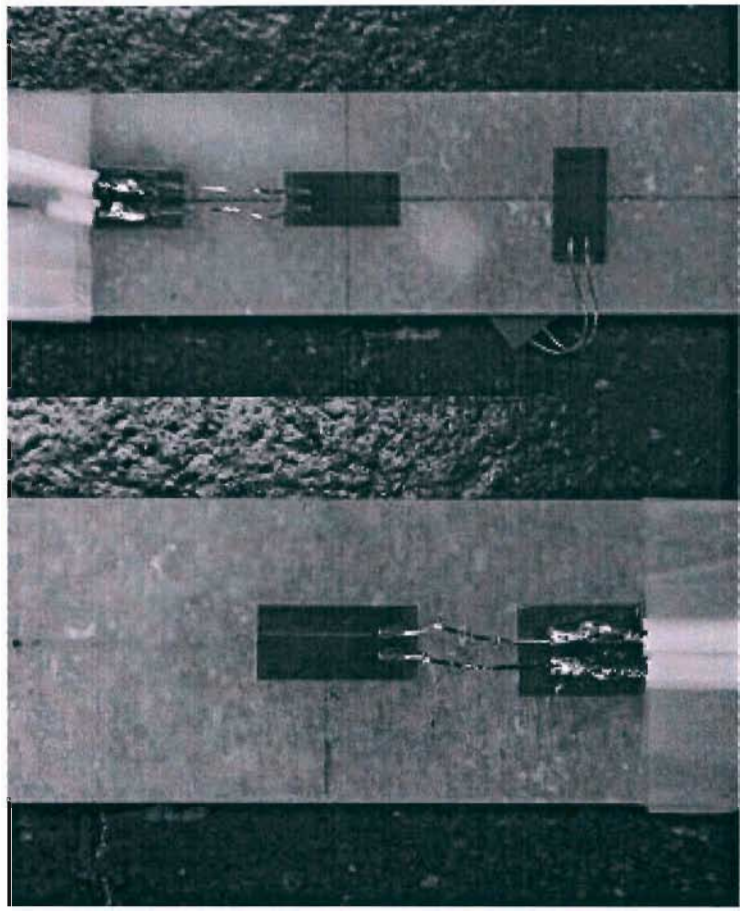

Fig. 3.4 Close-up showing strain gauge attachment

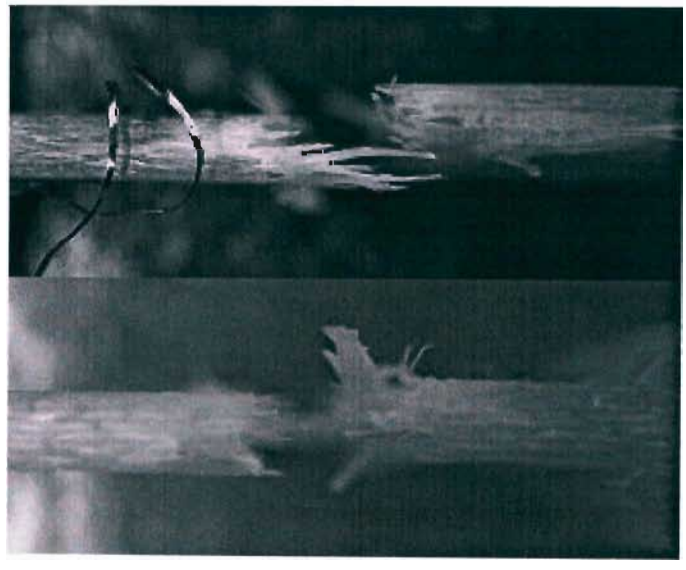

Fig. 3.5 Failure through thickness

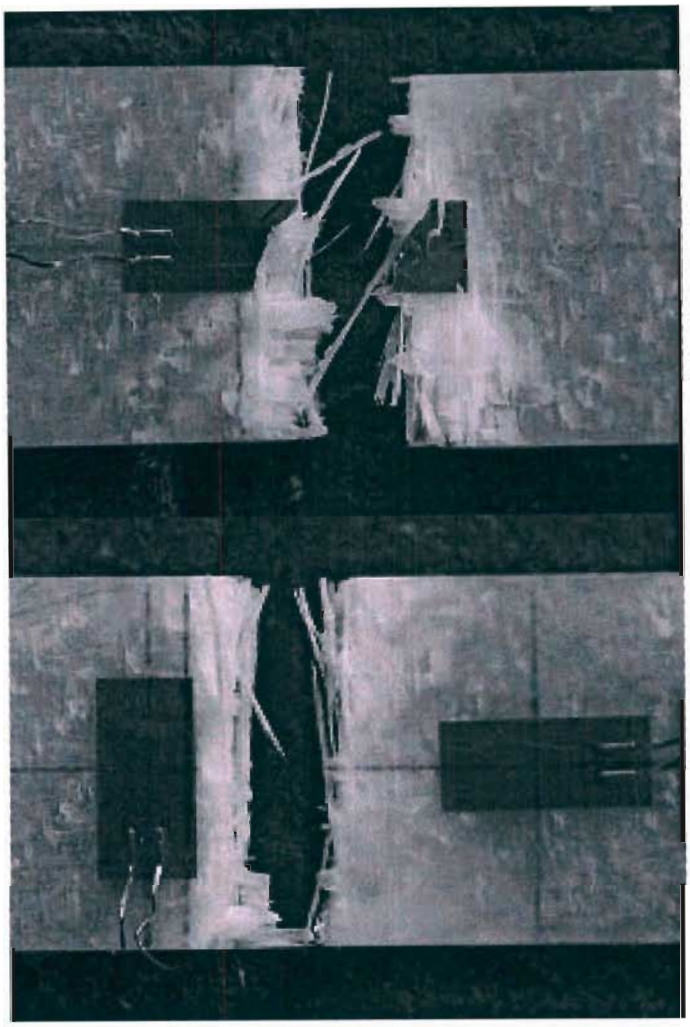

Fig. 3.6 Failure across plate

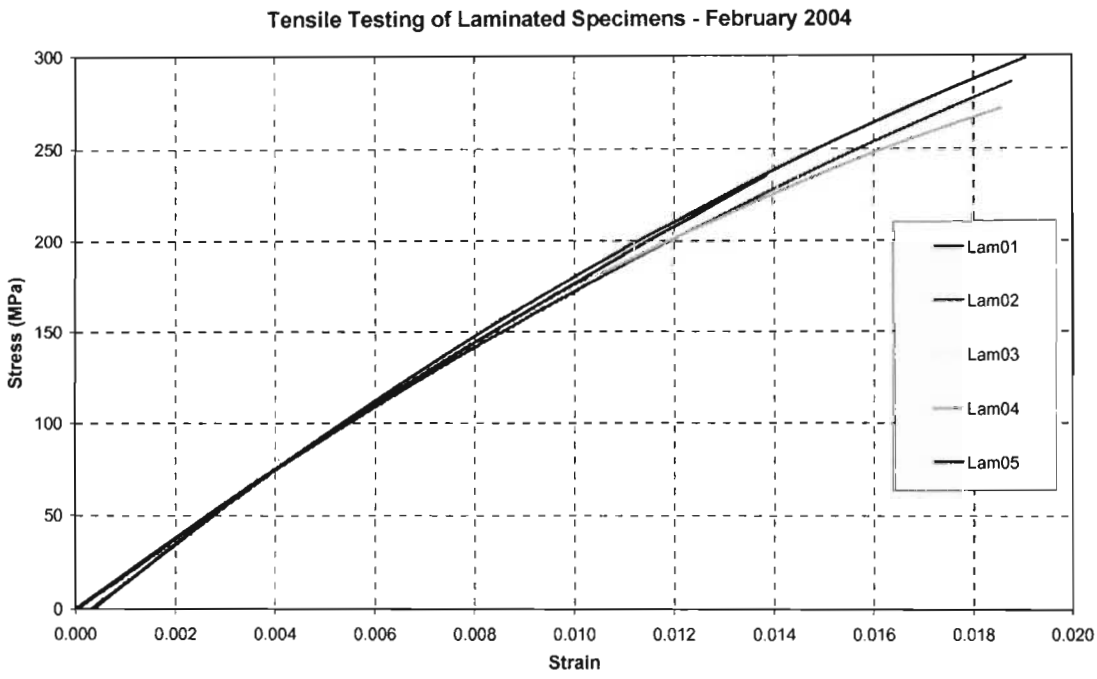

Fig. 3.7 Laminate stress-strain curves

3.1.2 Tensile characterisation parameters

Characterisation of the material's tensile response for input into the PAM-CRASH bi-phase material model (material 130) requires the spectrum of material characterisation parameters shown in Table 3.4. Of the required parameters, E_1, E_2, ν_{12}, ε_i, ε_1, ε_u, d_1 and d_u are obtained from the tensile curve (since a balanced fabric has been used $E_1 = E_2$). The remaining values (E_3, G_{12}, G_{23}, G_{13}, ν_{23}, ν_{13}) are taken from literature (Naik, 1994; Vasiliev and Morozov, 2001) to be representative of the woven fabric glass-epoxy laminate under investigation. Further, since a woven balanced construction is used, $G_{23} = G_{13}$ and $\nu_{23} = \nu_{13}$.

Table 3.4 Parameters required for tensile material characterisation

Material constants			Damage Parameters	
Tensile Modulii	Shear modulii	Poisons ratios	Critical strains	Damage values
E_1	G_{12}	ν_{12}	ε_{iv}	-
E_2	G_{23}	ν_{23}	ε_{1v}	d_1
E_3	G_{13}	ν_{13}	ε_{uv}	d_u

The tensile stress-strain curve obtained for specimen Lam02 (§ 3.1.1) is selected as representative of the laminated material's average response and is shown in Fig 3.8, together with the three critical points required for calculation of the material elastic modulus and damage parameters. From Fig. 3.8:

$$E_{11} = \frac{\sigma_i}{\varepsilon_i} = \frac{170}{0.0100} = 17GPa$$

Poisson's ratio, ν_{12}, has been determined from experiment by comparing longitudinal and transverse strains and has a value of

$$\nu_{12} = 0.17$$

A typical value of 0.3 is used for the out of plane Poisson's ratios, giving:

$$\nu_{23} = \nu_{13} = 0.3$$

Description of the damage behaviour requires the selection of critical points from the tensile curve as described in § 2.2. Since the material (in tension) immediately loses load carrying capability at the point of ultimate failure, the final damage point (u) is chosen at a point close to zero stress and at a slightly higher strain than the material's strain at ultimate failure (see Fig. 3.8). Here a clear distinction needs to be drawn between the modelled material's ultimate damage point (u) and the real material's ultimate failure point. For the purpose of damage modelling these points are usually not the same. At failure the physical material (at the failure location) can no longer support load and, theoretically, the material damage should be equal to 1, for modelling purposes, however, the final damage value is usually chosen to have some value less than but close to 1, in order to ensure solution stability. This is why the ultimate damage point is chosen by the user as a point close to zero stress at some strain slightly higher than the material strain measured at failure. This does create some subjectability regarding the material characterisation but model calibration runs, which simulate the material's response to a tensile test, are used to ensure that a satisfactory result is obtained using the calculated modelling parameters.

The critical points extracted from the tensile curve (Fig. 3.8) are:

(i): $(\varepsilon_i, \sigma_i) = (0.0100, 170\text{MPa})$
(1): $(\varepsilon_1, \sigma_1) = (0.0188, 285\text{MPa})$
(u): $(\varepsilon_u, \sigma_u) = (0.0200, 20\text{Mpa})$

In order to characterise damage, the strains involved must be converted to their volumetric equivalents using Eq. (2.11):

$$\begin{aligned}\varepsilon_v &= (1-\nu_{12}-\nu_{13})\varepsilon_{11} \\ &= (1-0.17-0.3)\varepsilon_{11} \\ &= 0.53\varepsilon_{11}\end{aligned} \tag{3.1}$$

Substituting the uniaxial strains (ε_i, ε_1, ε_u) read from the graph into Eq. (3.1):

$$\begin{aligned}\varepsilon_{iv} &= 0.0053 \\ \varepsilon_{1v} &= 0.0100 \\ \varepsilon_{uv} &= 0.0106\end{aligned}$$

The damage values are calculated from:

$$E = E_0(1-d) \tag{3.2}$$

Giving

$$\begin{aligned}d &= 1-\frac{E}{E_0} \\ &= 1-\frac{\sigma}{E_0\varepsilon}\end{aligned} \tag{3.3}$$

The damage values are then found as follows:

$$\begin{aligned}d_1 &= 1-\frac{\sigma_1}{E_0\varepsilon_1} \\ &= 1-\frac{285}{17000(0.0188)} \\ &= 0.12\end{aligned} \qquad \begin{aligned}d_u &= 1-\frac{\sigma_u}{E_0\varepsilon_u} \\ &= 1-\frac{20}{17000(0.0200)} \\ &= 0.95\end{aligned}$$

The value for the in-plane shear modulus (G_{12}) reported by Naik (1994) for a similar glass fabric reinforced epoxy system is used as a representative value for modelling of the investigated material, giving:

$$G_{12} = 5.5\text{GPa}.$$

The out of plane shear modulus values ($G_{23} = G_{13}$) are set equal to a typical unidirectional shear modulus for a glass-epoxy system (Vasiliev and Morozov, 2001), and the material stiffness in the thickness direction (E_3) is taken as the transverse modulus for the same glass-epoxy system, giving:

$$G_{23} = G_{13} = 3.4\text{ MPa}.$$

$$E_3 = 13\text{ GPa}$$

A summary of the tensile material characterisation parameters is provided in Table 3.5.

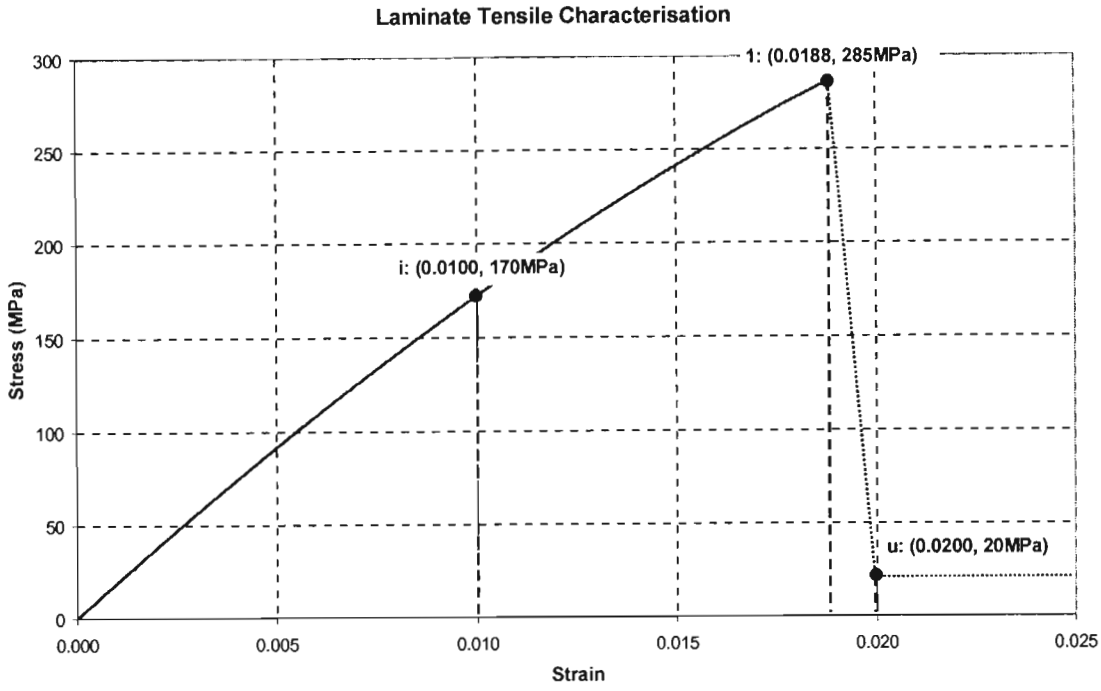

Fig. 3.8 Critical points for tensile characterisation

Table 3.5 Material tensile characterisation parameters

Material Constants						Damage Parameters			
tensile modulii (GPa)		shear modulii (GPa)		Poisson's ratios		critical strains		damage values	
E_1	17	G_{12}**	5.5	ν_{12}	0.17	ε_{iv}	0.0053	-	-
E_2	17	G_{23}*	3.4	ν_{23}	0.30	ε_{1v}	0.0100	d_1	0.12
E_3*	13	G_{13}*	3.4	ν_{13}	0.30	ε_{uv}	0.0106	d_u	0.95

* (Vasiliev and Morozov, 2001); ** (Naik, 1994)

3.2 Compressive characterisation

In order to address the selected material's behaviour under high strain rate loading, compressive Hopkinson split bar testing (Al-Mousawi et al., 1997; Gray, 2000) was identified as the most feasible option, especially since access to the apparatus existed without the need for developing the technique and apparatus independently. Specimens tested in compression using the Hopkinson split bar (HSB) are typically cylindrical with an aspect ratio, L/D, close to unity. This has been shown to produce interpretable and accurate results, however it is also suggested that specimens for materials with low sound speed, such as the composite under investigation, should have a smaller aspect ratio of around 0.5, in order to promote specimen ring up (Wu and Gorham, 1997; Gray et al., 1997). The specimen ring up refers to the time taken for the specimen to reach dynamic equilibrium, an important aspect of high strain rate testing. Investigation into the effect of specimen size and aspect ratio for Hopkinson compression testing was not included in the scope of work for this study and so the specimen geometry has been selected based on a review of Hopkinson testing and laboratory advice.

The specimens used have a length and diameter of 10mm, giving an L/D ratio of 1. These specimens were tested in compression at quasi-static load rates using an MTS servo-hydraulic rig and at dynamic loading rates using a Hopkinson split bar (*BISRU Lab, UCT*). In order to expedite model implementation, the quasi-static data obtained from the cylindrical specimens is used to describe the laminate for modelling purposes. Future modelling will require the testing of plate specimens in compression in order to validate the compressive characterisation.

3.2.1 Dynamic testing procedure

Apparatus

In order to characterise the behaviour of the investigated materials at higher rates of loading, Hopkinson Split Pressure Bar (HSPB) testing is employed. An illustration of a typical Hopkinson Compression Setup is shown in Fig. 3.9, with the primary components being:

Gas gun – fires the striker bar into the input bar. The gun used is shown in Fig. 3.10.

Speed trap – records the speed of the striker just before impact.

Striker bar – fired from the gas gun into the input bar in order to set up a travelling compression wave in the input bar material.

Input bar – carries the compressive pulse to the specimen. A strain gauge attached to the bar surface records the travelling incident and reflected pulses.

Output bar – provides a face for the specimen to be compressed against. A strain gauge on the output bar is used to record the transmitted pulse.

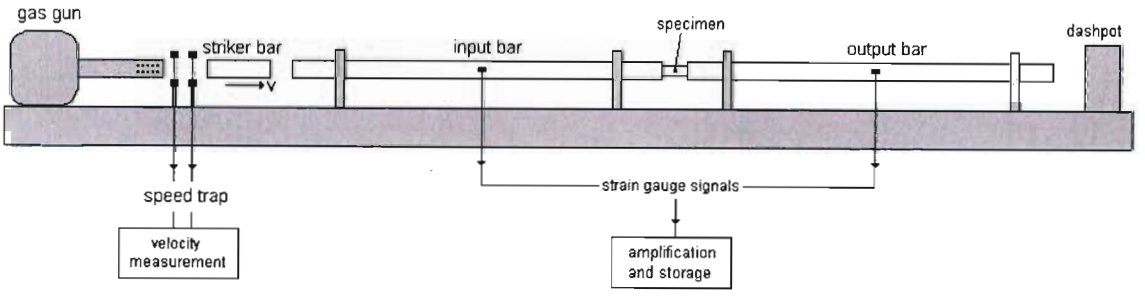

Fig. 3.9 Schematic of typical Hopkinson split pressure bar

As per the experimentally verified Hopkinson Split Bar theory (Spotts, 1964; Gray, 2000) during a Hopkinson test, a pressure wave of well defined amplitude and duration is set up in the input bar material when it is impacted upon by the striker bar. This wave travels along the input bar towards the specimen (which is sandwiched between the input and output bars) and when the travelling wave impacts upon the specimen (at the bar/specimen interface), some of the wave is transferred to the specimen and some reflects back along the input bar. This happens again at the second interface where the specimen is in intimate contact with the output bar. By measuring the amplitude and duration of the primary pulse travelling through the bars (using strain gauges attached to the surface of the bars) a dynamic stress-strain curve can be constructed for the material under investigation.

The desired output, for the purpose of material characterisation, is a series of stress-strain curves $\sigma = \sigma(\varepsilon)$ at various strain rates. A surface $\sigma = \sigma(\varepsilon, \dot{\varepsilon})$ (which is a function of two dimensions) can then be fitted to the data. When this data is input into a suitable numerical model, the designer is able to describe how the material behaves at various rates of loading and can hence use the model to predict how the material will respond when loaded under impact conditions. On the other hand, if there is an insignificant change in material response at the strain rates of interest, then it is not necessary to include the strain rate effect in the numerical model and quasi-static data is sufficient. In either case, the results of Hopkinson testing are used, firstly to determine whether a significant strain rate effect is evident and, if so, to then fit a surface to the data for the purpose of numerical modelling.

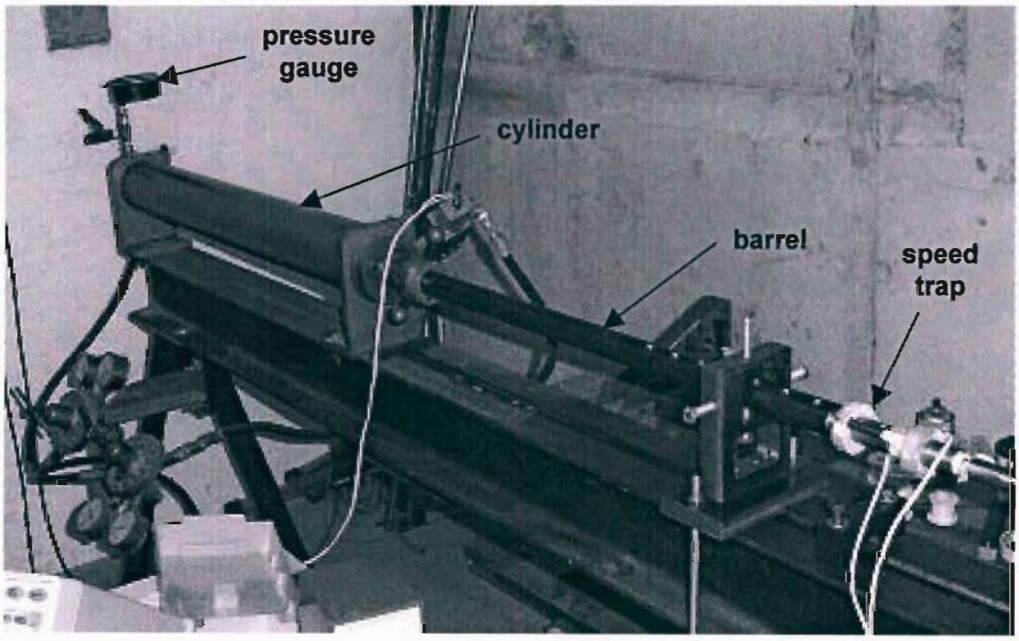

Fig. 3.10 Gas gun used to fire striker bar (*BISRU Lab, UCT*)

Data Processing

The data processing algorithm used to convert the voltage pulses, which provide a record of the input and output bar surface strains during the impact event, is illustrated in Fig. 3.11. The raw voltage pulses are converted to pressure bar strains, using:

$$\varepsilon = \left(\frac{4}{FGK}\right) \times \frac{V_{OUT}}{V_{IN}} \tag{3.4}$$

where
ε = strain
V_{OUT} = bridge output voltage
V_{IN} = bridge excitation voltage
F = gauge factor
G = amplifier gain
K = bridge configuration constant

Time shifting of the pulses is completed to align the incident, reflected and transmitted pulse. The magnitude of the shift in time is equal to the time taken for the pulse to reach the gauge location whilst travelling through the bar material and is calculated using:

$$\Delta t = C_0 L_G \tag{3.5}$$

where Δt = required pulse shift
C_0 = wave speed for bar material
L_G = distance covered by pulse between gauge and interface

The force at the specimen/bar interfaces are calculated using (Gray, 2000, p.9):

$$F_1 = AE(\varepsilon_i + \varepsilon_r)$$
$$F_2 = AE\varepsilon_t \tag{3.6}$$

and specimen strain rate may be found from (Kaiser, 1998, p.28):

$$\frac{d\varepsilon_S}{dt} = \frac{C_0(\varepsilon_t - \varepsilon_i + \varepsilon_r)}{L_S} \tag{3.7}$$

where F_1 = force at interface 1
F_2 = force at interface 2

subscripts: i - incident, r - reflected, t - transmitted

A = bar cross sectional area
E = bar elastic modulus
ε_i, ε_r, ε_t = bar strains

ε_S = specimen strain
C_0 = bar wave speed
L_S = specimen length

Specimen stress is then calculated from force over area:

$$\sigma_S = \frac{1}{A_S} F_2 \tag{3.8}$$

where A_S = specimen cross sectional area

Specimen strain is the time integral of specimen strain rate:

$$\varepsilon_S(t_i) = \int_{t_0}^{t_i} \frac{d\varepsilon}{dt} dt \tag{3.9}$$

The stress-strain data output from the HSPB data processing algorithm (Fig. 3.11) still contains noise. The noisy stress-strain data is filtered using a first order low pass filter, implemented using the MATLAB Simulink software (Fig. 3.12).

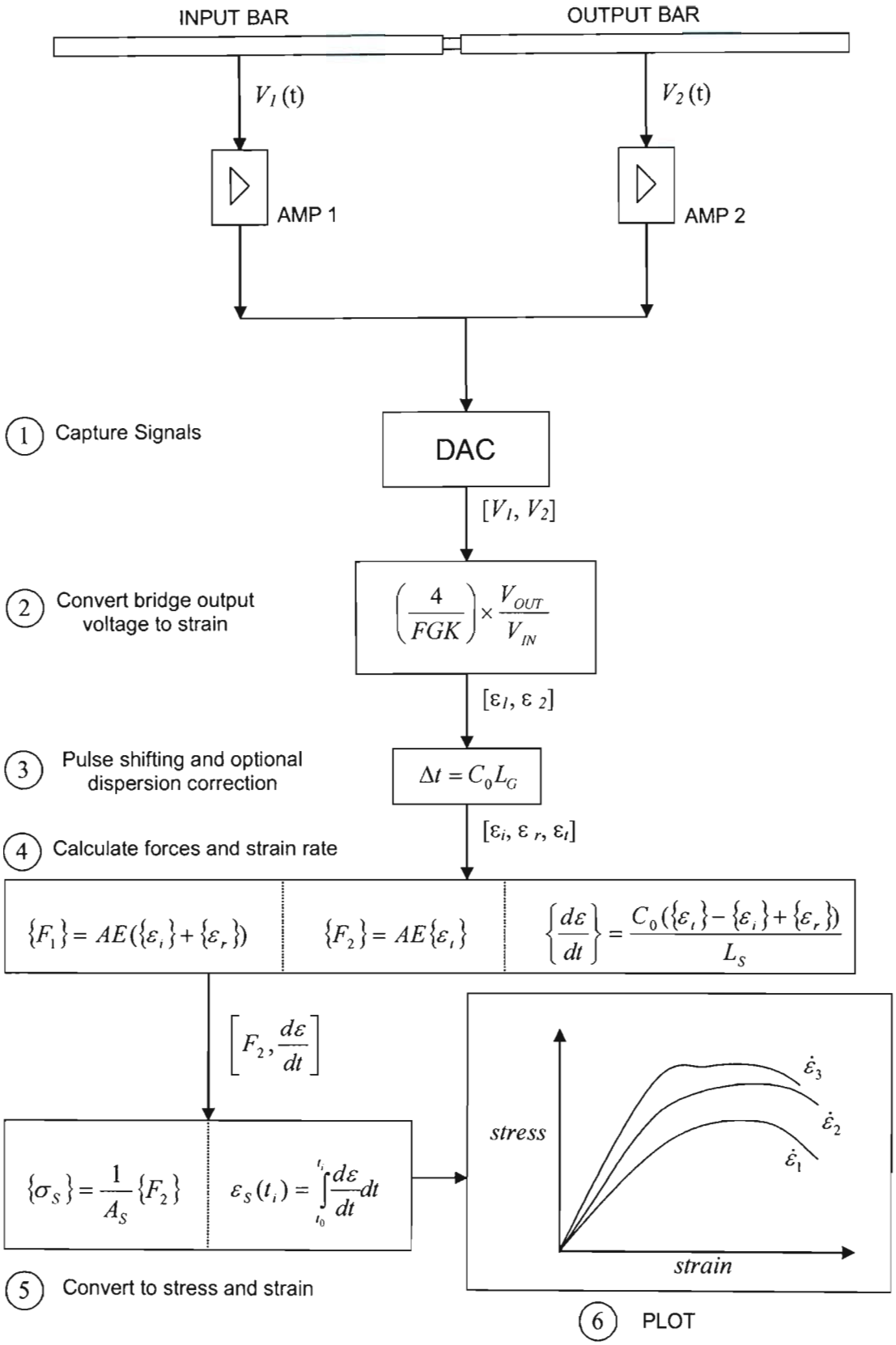

Fig. 3.11 Compressive HSPB data processing algorithm

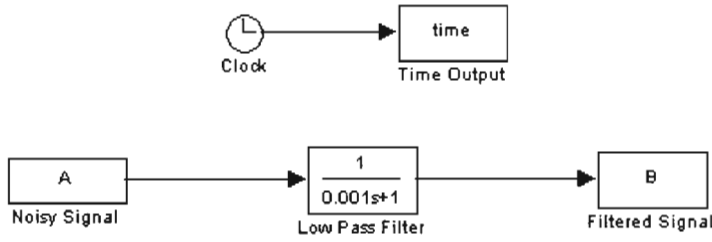

Fig. 3.12 Simulink model used to filter noisy data

3.2.2 Compressive testing of laminated specimens

Laminated specimens of cylindrical geometry were manufactured using the same glass fabric reinforcement and epoxy resin used to manufacture the demonstrator component (§ 4) and tensile test specimens (§ 3.1.1). The fabric was wrapped around a pin in order to obtain the cylindrical preform that is subsequently moulded using a resin transfer process (Fig.3.13), resulting in moulded 'sticks' around 40 mm in length with a diameter of 10 mm. Specimens of length 10.4 mm were then parted off using a turning operation and subsequently polished down to a length of 10.2 mm. The mould assembly is shown in Fig. 3.14.

Table 3.6 shows mass and length measurements taken for the laminated specimens tested. Also shown is the calculated volume and density for each specimen. A summary of the average values and sample standard deviations (for the measured and calculated values) is provided at the bottom of the table. Photographs showing a laminated specimen before testing, specimens tested at quasi-static loading rates and specimens tested at dynamic loading rates are provided in Fig's 3.15 – 3.17.

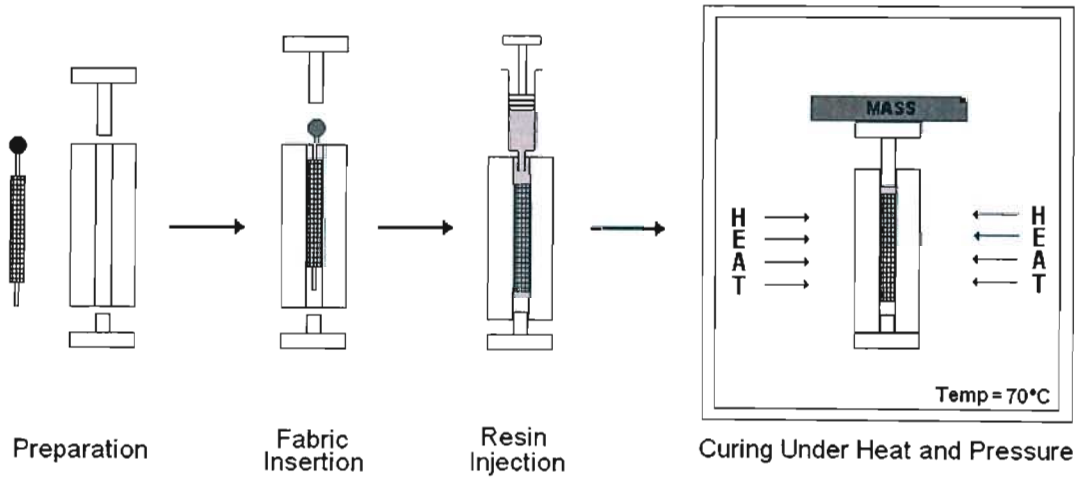

Fig. 3.13 Manufacture of the laminated specimens by resin transfer

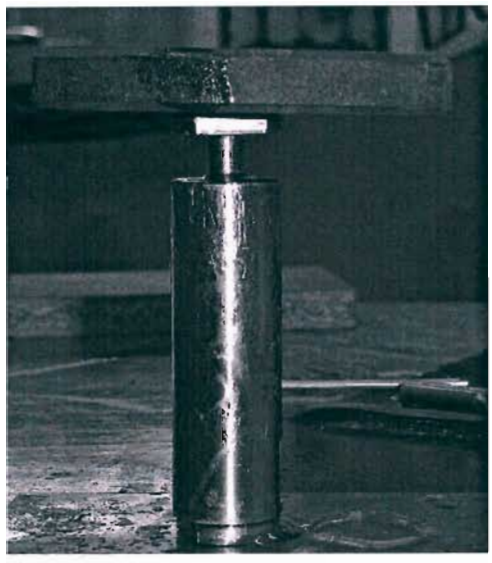

Fig.3.14 Mould assembly

Table 3.6 Laminated specimen measurements

Laminated Specimens				
	mass	length	volume	density
SPECIMEN	(g)	(mm)	(mm^3)	(kg/m^3)
2a	1.195	10.07	796.4	1500
2b	1.198	10.20	817.1	1466
3a	1.195	10.20	817.1	1462
3b	1.193	10.20	817.1	1460
3c	1.186	10.20	817.1	1451
Averages	**1.193**	**10.17**	**813.0**	**1468**
STD deviation	**0.005**	**0.06**	**9.3**	**19**

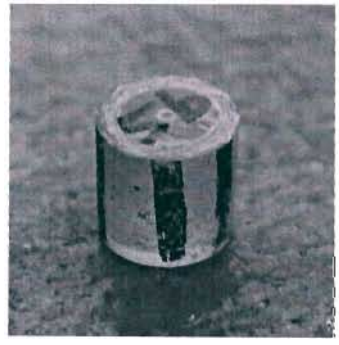

Fig. 3.15 Laminated compression specimen

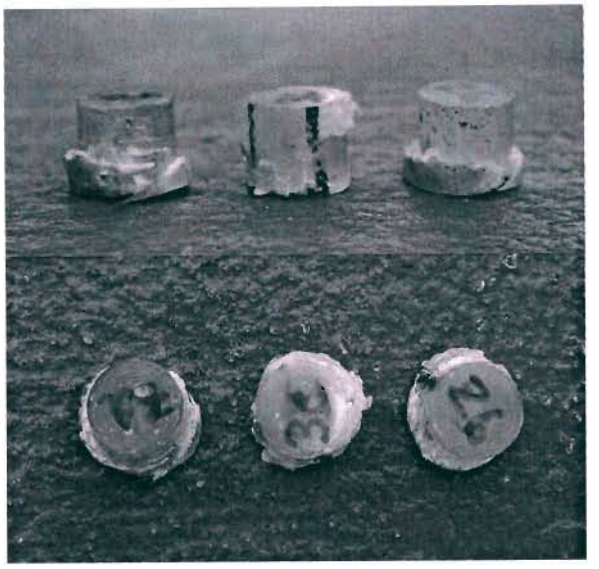

Fig. 3.16 Laminated specimens tested at quasi-static loading rate

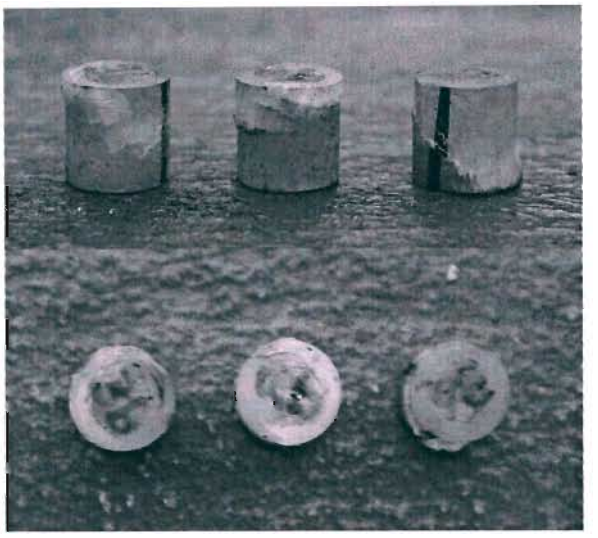

Fig. 3.17 Laminated specimens tested at dynamic loading rates

The typical stress-strain plot obtained from Hopkinson testing of the laminated specimens at a strain rate of around $700s^{-1}$ is compared with the plot obtained from quasi-static testing (Fig. 3.18). An increase in specimen strength from just over 250MPa to around 325MPa is observed when going from static to dynamic loading. The initial slope of the dynamic stress-strain curve is also greater than the initial slope of the static stress-strain curve

In order to obtain smoother curves for numerical processing and curve fitting, noise is filtered from the stress-strain curve using a first order low pass filter implemented using the MATLAB Simulink software (Fig. 3.12). The filtered curves are further processed through a 2-dimensional interpolation algorithm in order to obtain a surface plot showing how the material's stress-strain response changes with increasing magnitude of strain rate (Fig. 3.19). Since only one dynamic curve is available, it has been assumed that the material response will not change much in the range $400 < \dot{\varepsilon} < 800\ s^{-1}$, as was observed for randomly reinforced SMC specimens tested (§ 3.2.3). This assumption allows repetition of the results obtained at 700 s^{-1} for strain rates of 400 s^{-1} and 800 s^{-1}. The flat section of the surface in Fig. 3.21 is a result of constant extrapolation of the stress at failure obtained from the dynamic experiment.

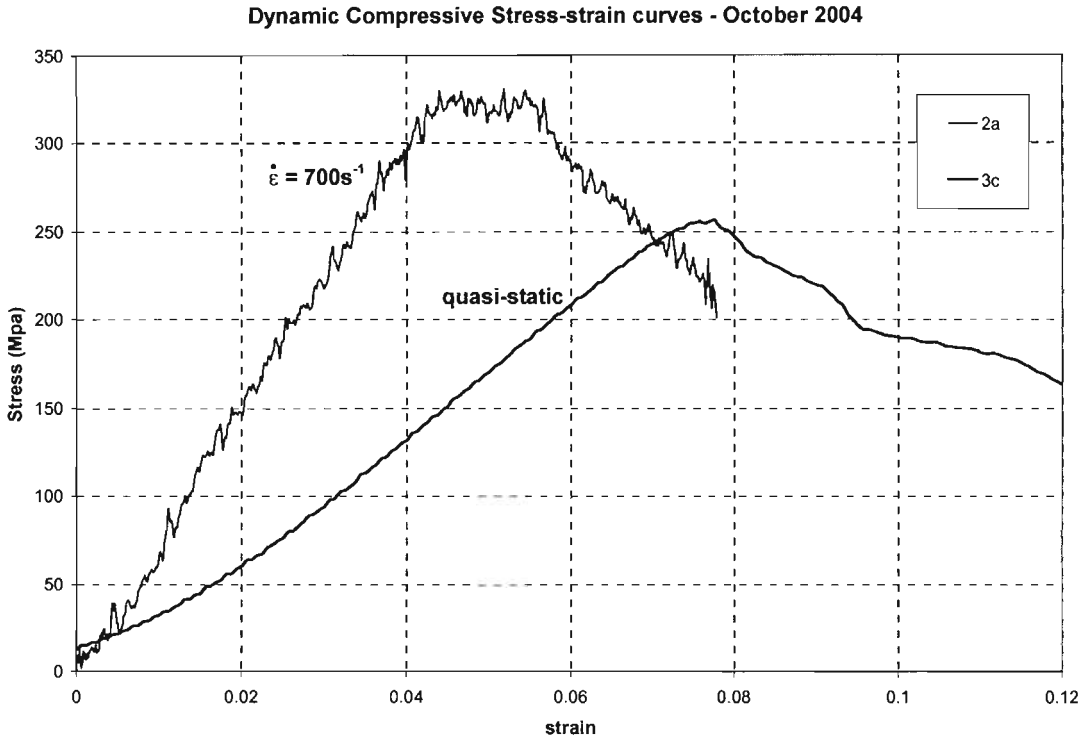

Fig. 3.18 Stress-strain response at quasi-static and dynamic strain rates, glass fabric/epoxy

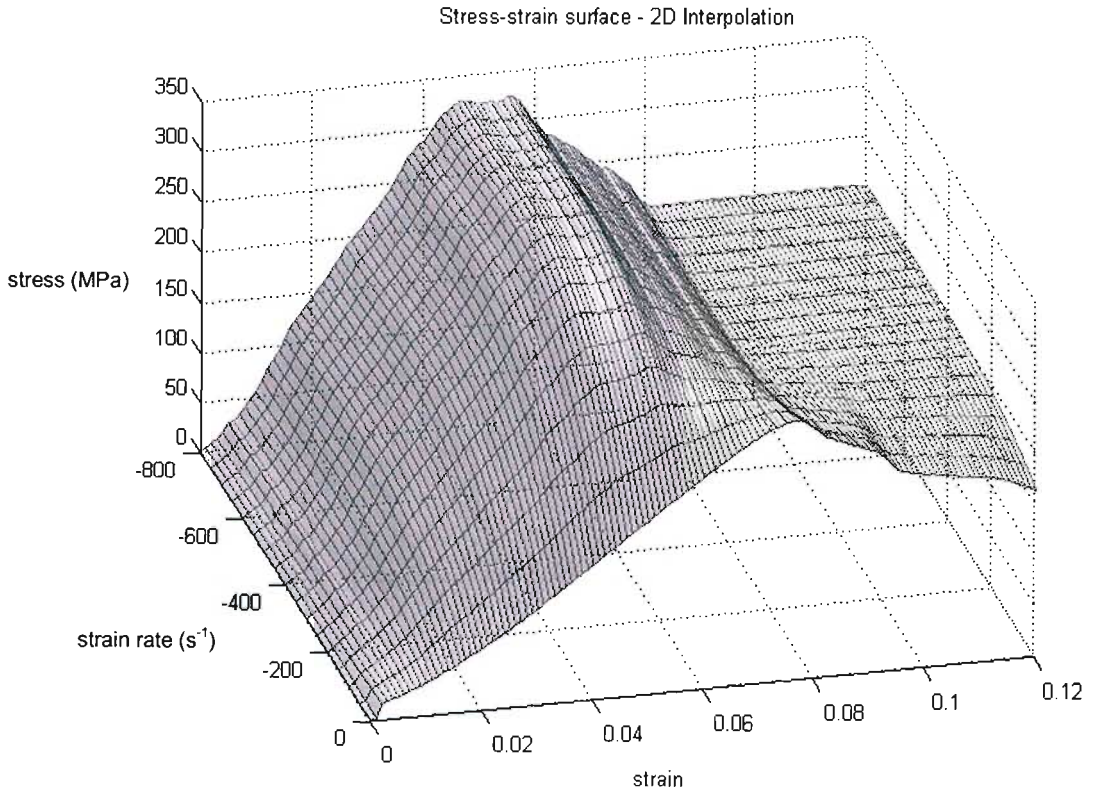

Fig. 3.19 Surface plot, showing change in material response with increasing strain rate (laminate)

3.2.3 Compressive testing of randomly reinforced specimens

Investigation of high strain rate behaviour for a randomly reinforced composite material has also been undertaken, providing strain rate data for another class of composite material. Specimens manufactured from sheet moulding compound (SMC) comprising a polyester resin reinforced with random short glass fibre (average fibre length = 25 mm; fibre volume fraction = 20%) were prepared for dynamic testing. The specimens have the same dimensions as the laminated specimens prepared for Hopkinson pressure bar testing (§ 3.2.2), with a length and diameter of 10mm. Table 3.7 shows mass and length measurements taken for all of the SMC specimens tested. Also shown is the calculated volume and density for each specimen. A summary of the average values and sample standard deviations (for the measured and calculated values) is provided at the bottom of the table. Photographs showing an SMC specimen before testing, specimens tested at quasi-static loading rates and specimens tested at dynamic loading rates are provided in Fig's 3.20 – 3.22.

Table 3.7 SMC specimen measurements

Closed mould SMC specimens				
	mass	length	volume	density
SPECIMEN	(g)	(mm)	(mm^3)	kg/m^3
c4	1.385	10.01	787.0	1760
c5	1.404	10.00	785.4	1788
c6	1.417	10.00	785.4	1804
c7	1.389	10.02	788.5	1761
c8	1.400	10.01	787.0	1779
c9	1.364	10.01	787.0	1733
c10	1.400	10.02	788.5	1775
c11	1.350	10.01	787.0	1715
c12	1.343	9.99	783.8	1713
c13	1.389	10.00	785.4	1769
c14	1.398	10.03	790.1	1769
c15	1.381	10.02	788.5	1751
c16	1.414	10.01	787.0	1797
c17	1.397	10.02	788.5	1772
c18	1.393	10.01	787.0	1770
c19	1.382	10.01	787.0	1756
c20	1.415	10.00	785.4	1802
c21	1.389	10.01	787.0	1765
c22	1.424	10.01	787.0	1809
c23	1.399	10.02	788.5	1774
c24	1.393	10.00	785.4	1774
Averages	**1.392**	**10.01**	**787.0**	**1768**
STD deviation	**0.020**	**0.01**	**1.5**	**26**

Fig. 3.20 SMC compression specimen

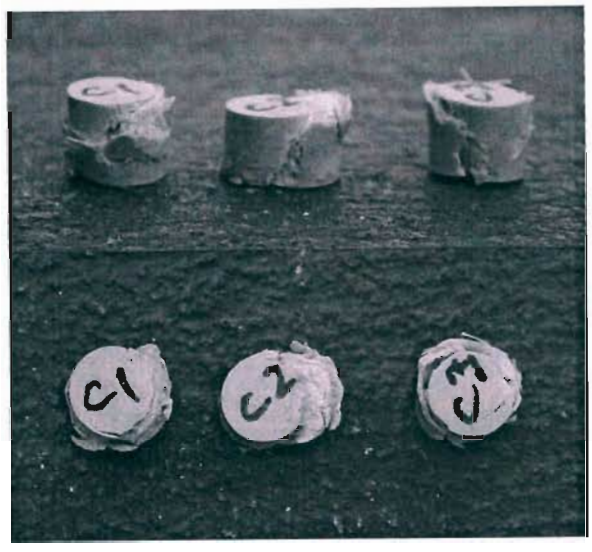

Fig. 3.21 SMC specimens tested at quasi-static loading rate

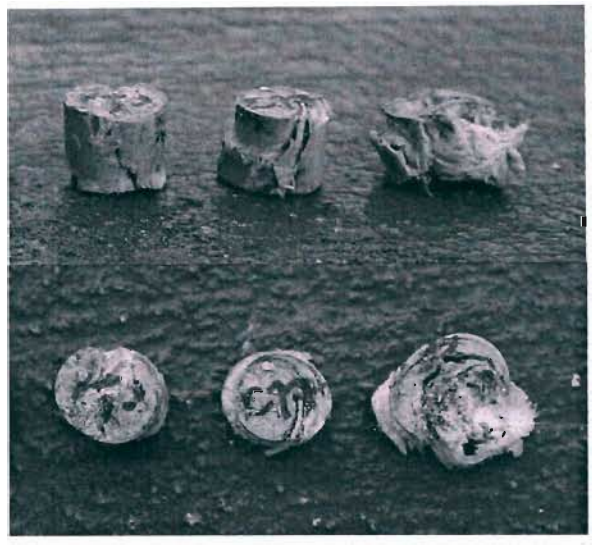

Fig. 3.22 SMC specimens tested at dynamic loading rates

The dynamic stress-strain plots for the SMC material (at three different strain rates) are shown below (Fig. 3.23), together with a stress strain plot obtained during quasi-static testing (strain rate $\approx$ 0). In order to obtain smoother curves for numerical processing and curve fitting, noise is filtered from the stress-strain curves using a first order low pass filter implemented using the

MATLAB Simulink software (Fig. 3.12). The filtered curves (Fig. 3.24) are further processed through a 2-dimensional interpolation algorithm in order to obtain a surface plot showing how the material's stress-strain response changes with increasing magnitude of strain rate (Fig. 3.25). The curves (for both the laminated and SMC material tested) serve to indicate the nature of the strain rate effect for the material concerned and may further be used to fit analytical laws to the experimental data or the curves may be input into an interpolation function for numerical description of the strain rate behaviour.

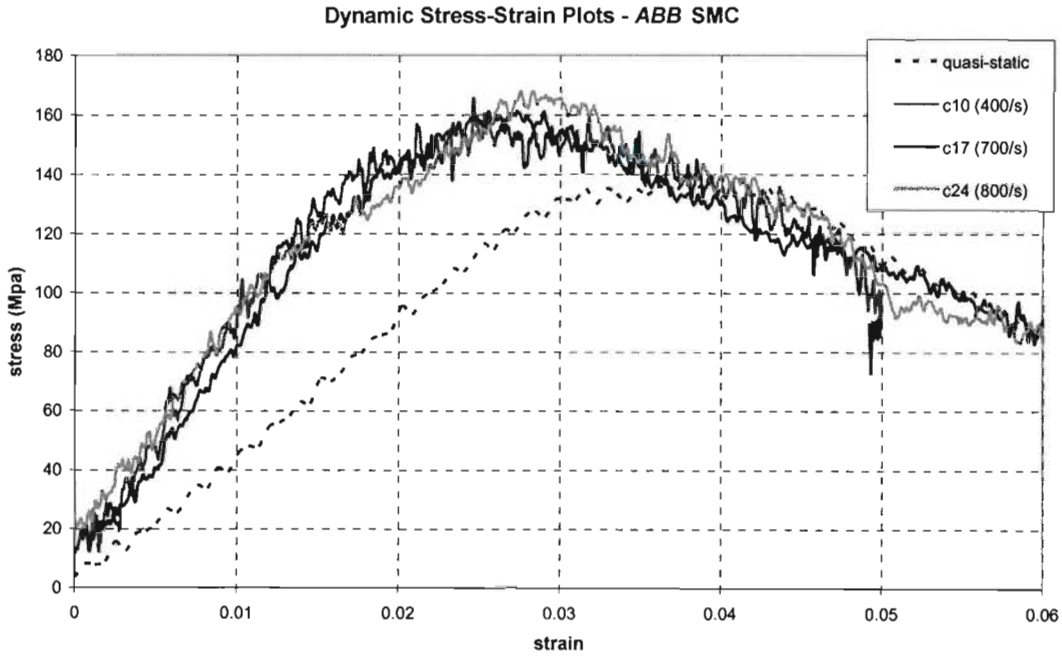

Fig. 3.23 Stress and strain rate plotted against strain, SMC material (unfiltered)

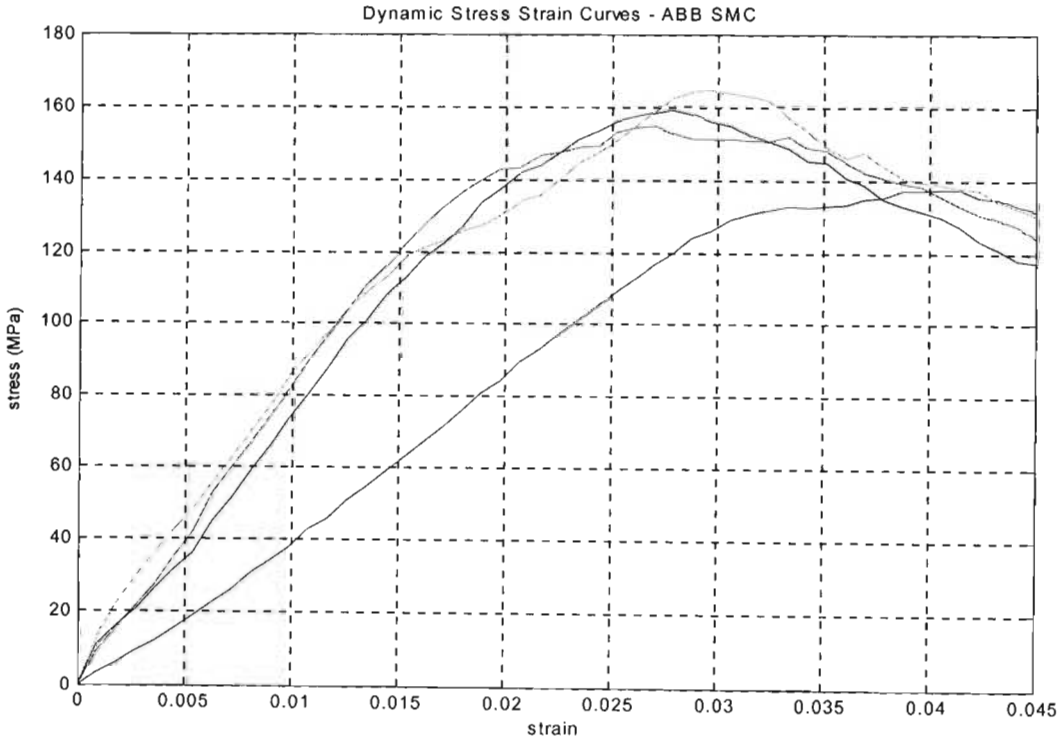

Fig. 3.24 Filtered stress-strain curves

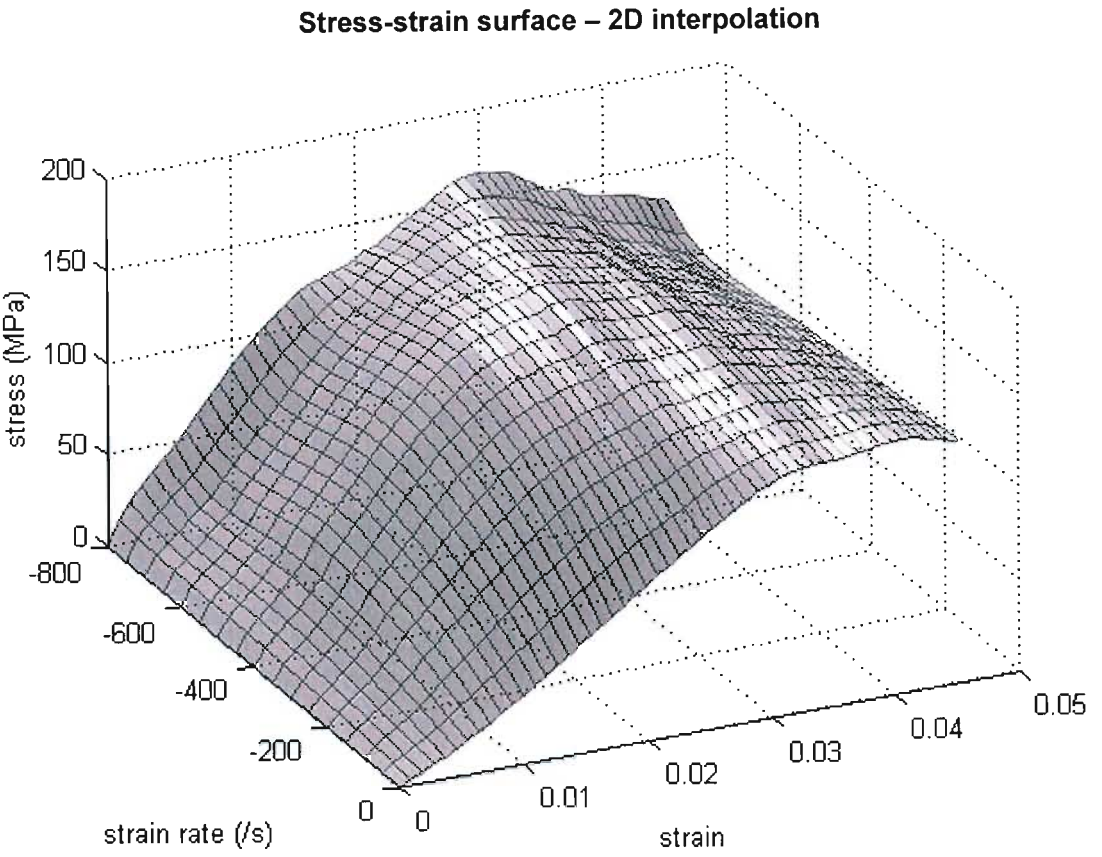

Fig. 3.25 Surface plot, showing change in material response with increasing strain rate (SMC)

3.2.4 Compressive characterisation parameters

A discussion of the theory of the bi-phase material model has already been provided (§ 2.2) and the set of material characterisation parameters required for implementation of the material model were identified. The parameters E_1, E_2, E_3, G_{12}, G_{13}, G_{23} ν_{12}, ν_{13}, ν_{23}, ε_i, ε_1, ε_u, d_1 and d_u are necessary for both tensile and compressive loadings, requiring testing of laminated specimens in tension and compression. The testing of laminated specimens in tension and subsequent calculation of the required material parameters for tensile characterisation has already been presented (§ 3.1). Data available from the compressive testing of cylindrical specimens under quasi-static loading rates, obtained for comparison with dynamic results (§ 3.2.2) is used here for the calculation of the compressive material parameters. Although the specimens are not in plate form it is felt that these specimens still give a fair representation of the thin-walled material's load response. Future modelling of the laminated demonstrator's response will require validation of the compressive characterisation through compressive testing of plate specimens. The required compressive characterisation parameters are shown in Table 3.8.

In a similar fashion as for the tensile characterisation, parameters E_1, E_2, ε_i, ε_1, ε_u, d_1 and d_u are obtained from the compressive curve (since a balanced fabric has been used $E_1 = E_2$). Poisson's ratio, ν_{12}, is taken from tensile testing and the remaining values (E_3, G_{12}, G_{23}, G_{13}, ν_{23}, ν_{13}) are taken from literature as representative of the woven fabric glass-epoxy laminate under investigation. Further, since a woven, balanced construction is used $G_{23} = G_{13}$ and $\nu_{23} = \nu_{13}$.

Table 3.8 Parameters required for compressive material characterisation

Material constants			Damage Parameters	
Tensile Modulii	Shear modulii	Poisons ratios	Critical strains	Damage values
E_1	G_{12}	ν_{12}	ε_{is}	-
E_2	G_{23}	ν_{23}	ε_{1s}	d_1
E_3	G_{13}	ν_{13}	ε_{us}	d_u

From Fig. 3.26: $$E_{11} = \frac{\sigma_i}{\varepsilon_i} = \frac{275}{0.0630} = 4.37GPa$$

The value for Poisson's ratio found during tensile testing is used also for compression, giving:

$$\nu_{12} = 0.17$$

A typical value of 0.3 is used for the out of plane Poison's ratios, giving:

$$\nu_{23} = \nu_{13} = 0.3$$

Selection of the critical points for describing the damage behaviour of the laminated material under a compressive load does not require selection of a fictitious ultimate damage point (u), as for the tensile characterisation (§ 3.1.2), since the material is able to sustain a residual crushing load and the ultimate damage point can be read directly from the curve.

The critical points taken from the compression curve (Fig. 3.26) and used to describe the compressive damaging behaviour, are:

(i): $(\varepsilon_i, \sigma_i)$ = (0.0630, 275MPa)
(1): $(\varepsilon_1, \sigma_1)$ = (0.0750, 306MPa)
(u): $(\varepsilon_u, \sigma_u)$ = (0.1260, 142Mpa)

In order to characterise damage, the strains involved must be converted to their shear equivalents, using Eq. (2.11).

$$\begin{aligned}\varepsilon_s &= \frac{\varepsilon_{11}}{\sqrt{3}}(1+\nu_{12}+\nu_{13}-\nu_{12}\nu_{13}+\nu_{12}^2+\nu_{13}^2)^{1/2} \\ &= \frac{\varepsilon_{11}}{\sqrt{3}}(1+0.17+0.3-(0.17)0.3+0.17^2+0.3^2)^{1/2} \\ &= \frac{1.24}{\sqrt{3}}\varepsilon_{11}\end{aligned} \qquad (3.10)$$

Using Eq. (3.10) and the uniaxial strains (ε_i, ε_1, ε_u) read form the graph, the equivalent shear strains are found to be:

$$\varepsilon_{is} = 0.0451$$
$$\varepsilon_{1s} = 0.0537$$
$$\varepsilon_{us} = 0.0902$$

The damage values are then found as follows:

$$d_1 = 1 - \frac{\sigma_1}{E_0 \varepsilon_1}$$
$$= 1 - \frac{306}{4365(0.0750)}$$
$$= 0.07$$

$$d_u = 1 - \frac{\sigma_u}{E_0 \varepsilon_u}$$
$$= 1 - \frac{142}{4365(0.1260)}$$
$$= 0.74$$

The shear characterisation is the same as entered for the tensile case, giving:

$$G_{12} = 5.5\text{GPa}$$

$$G_{23} = G_{13} = 3.4\text{MPa}$$

The through thickness stiffness (E_3) is set equal to the typical resin compressive modulus, giving:

$$E_3 = 3 \text{ GPa}$$

A summary of the material characterisation parameters is provided in Table 3.9.

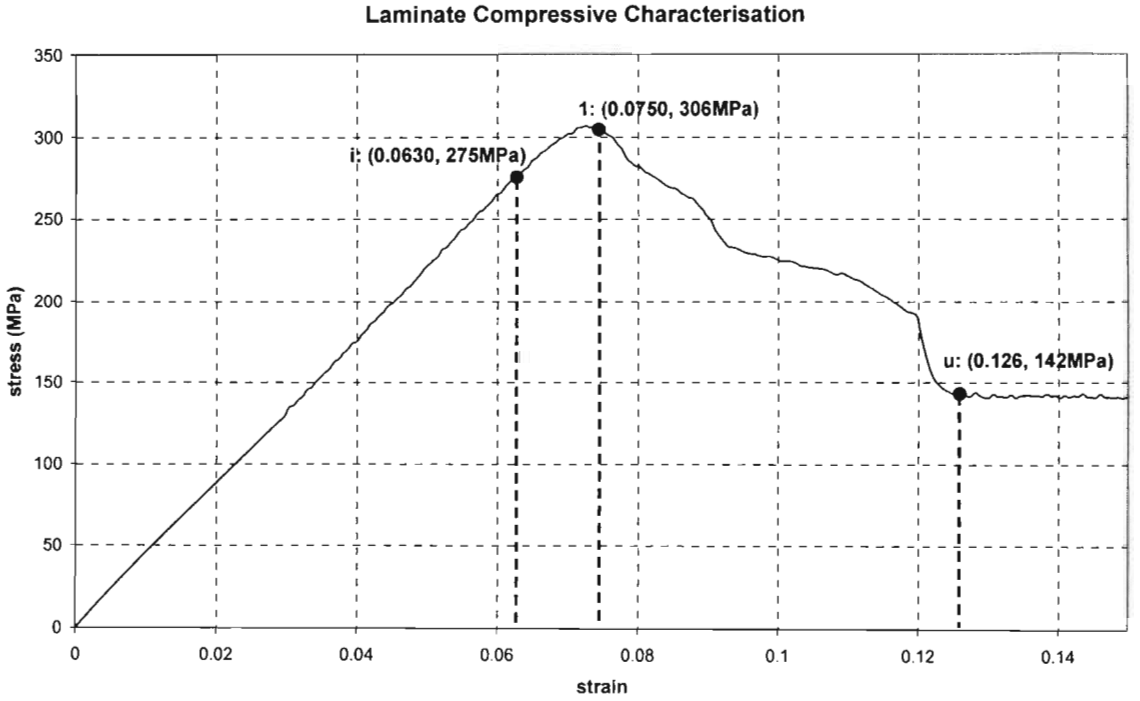

Fig. 3.26 Critical points for compressive characterisation

Table 3.9 Material compressive characterisation parameters

Material Constants						Damage Parameters			
compressive moduli (GPa)		Shear moduli (GPa)		Poisson's ratios		critical strains		damage values	
E_1	4.37	G_{12}	5.5	ν_{12}	0.17	ε_{is}	0.0451	-	-
E_2	4.37	G_{23}	3.4	ν_{23}	0.30	ε_{1s}	0.0537	d_1	0.07
E_3	3	G_{13}	3.4	ν_{13}	0.30	ε_{us}	0.0902	d_u	0.74

3.3 Calibration of material model

Modelling of the virtual material's response to separate cases of uniaxial tensile and compressive loading ensures that the enlisted characterisation parameters (Tables 3.5 and 3.9) produce the expected material response. The total thickness of the simulated specimen is 2.4mm (the same as the physical specimens). Layers of orthotropic shell elements (characterised using PAM-CRASH material 130) are used to model a laminated plate in tension or compression. The shell elements used to model the uniaxial tests have a thickness of 2.4mm, made up of 4 layers, each with a thickness of 0.6mm. This is a simplification of the real plate which is also 2.4mm thick but is made up of 8 layers of average thickness 0.3mm. The plate's width is 30mm and the length between the grips is 10mm. Both ends of the plate are clamped (all degrees of freedom fixed), with one end forced to translate with a velocity of 2mm/s in the loading direction. The model output includes the reaction force at the stationary clamp, as a function of time, as well as damage values and membrane stress resultants. Displacements have been calculated by time integration of the input velocity profile. In order to obtain a final plot for comparison with the tensile and compressive test results, it is necessary to convert the load and displacement data to stress and strain, respectively.

Conversion of force to stress is carried out using:

$$\sigma = \frac{F}{A} = \frac{F}{t \times w} = \frac{F}{(2.4 \times 10^{-3})(30 \times 10^{-3})} \tag{3.15}$$

and strain is calculated using:

$$\varepsilon = \frac{\delta}{L_0} \tag{3.16}$$

The results obtained from simulation of a tensile test on the glass-epoxy plate are compared with the experimental results, upon which the material characterisation is based (Fig. 3.27). This shows whether the characterisation is consistent. The first characterisation that uses the parameters calculated in § 3.1.2 (simulation 130A) produces an undershoot in the ultimate tensile strength. Parametric adjustments result in the material characterisations 130B and 130C which show improved agreement with the experimental stress-strain curve.

The result obtained through simulation of the laminated material's response to a uniaxial compressive load is compared to the results obtained from compression testing (Fig. 3.28). Good agreement is obtained and the compressive characterisation is accepted for further modelling purposes

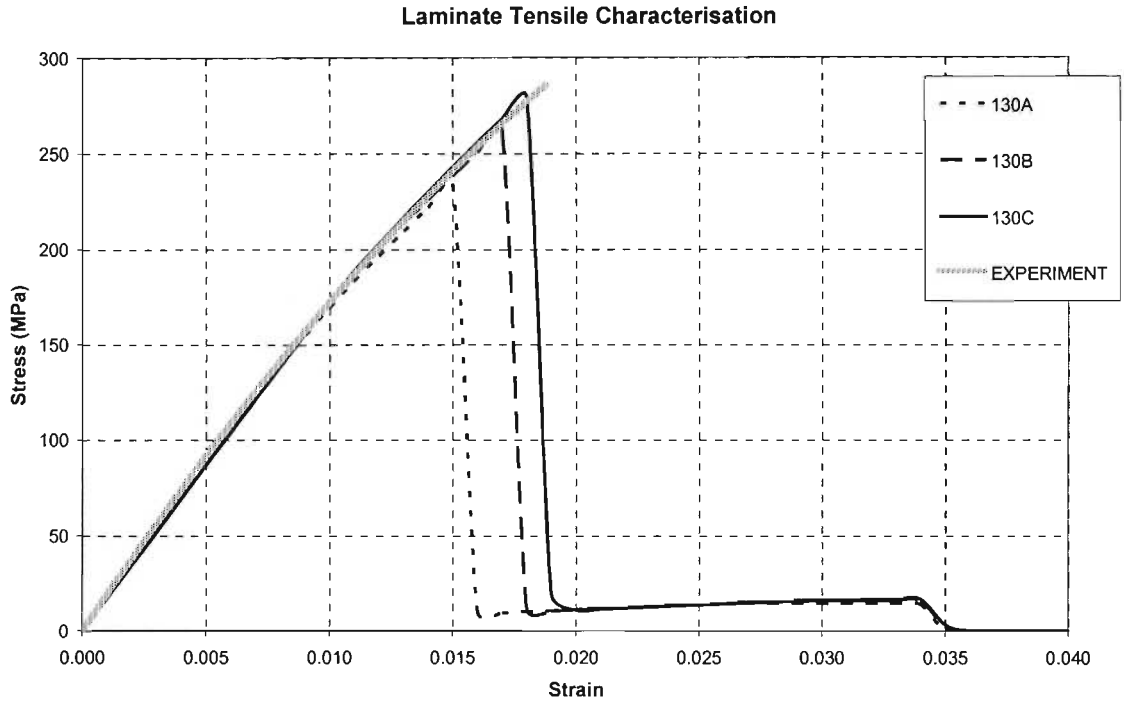

Fig. 3.27 Calibration of material model for uniaxial tension

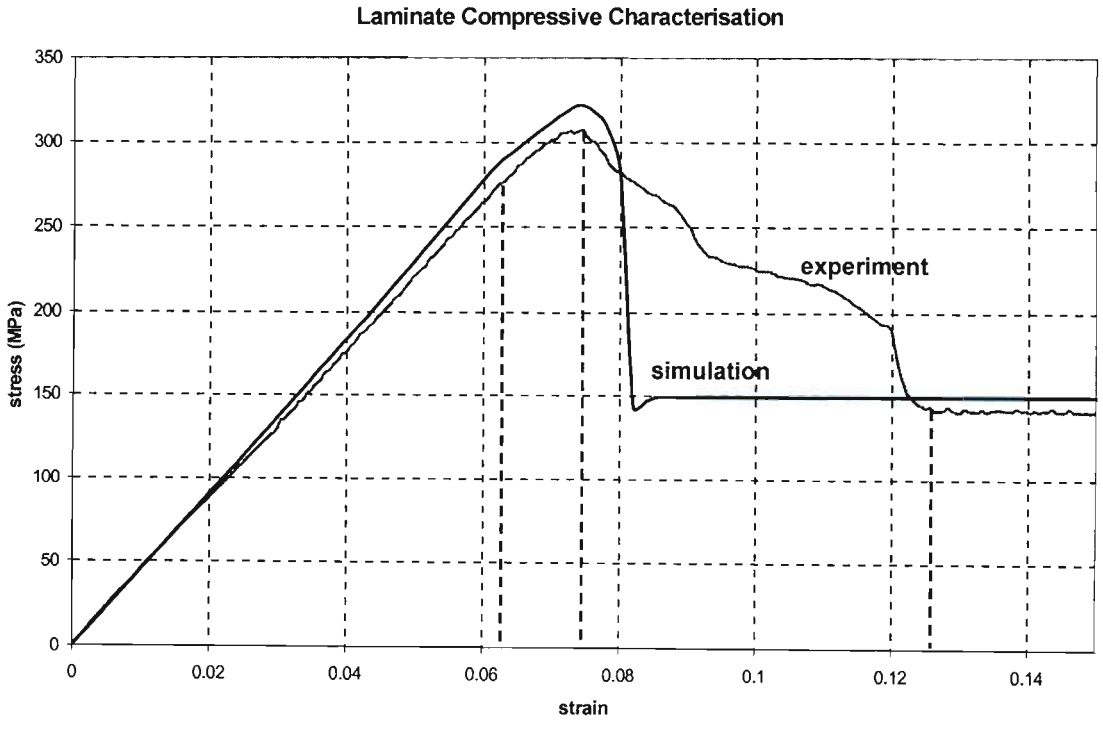

Fig. 3.28 Calibration of material model for uniaxial compression

3.4 Conclusions

Characterisation of the laminated material used to construct the demonstrator component (which serves to provide experimental data for evaluating the performance of instituted numerical models) has been completed. The process involved the tensile and compressive testing of suitably designed specimens. Plate specimens were used for tensile characterisation and cylindrical specimens were used for compressive characterisation. The selection of cylindrical specimens for compressive characterisation was influenced by the need to investigate the strain rate sensitivity of the laminated material. Material parameters for description of the bi-phase material model (which includes progressive damage modelling) were calculated using experimental recorded stress-strain curves. Calibration of the models was subsequently performed through simulation of tensile and compressive tests and satisfactory results were obtained.

Dynamic testing of the laminated material in compression, as well as for a polyester based SMC material, was completed for strain rates in the range $400 < \dot{\varepsilon} < 800\ s^{-1}$. For the cylindrical specimens tested in compression, the results showed an increase in strength when going from quasi-static loading conditions to the dynamic cases. The observed increase in strength is 13% for the laminated specimens and 11.4% for the SMC material also tested. The results also show an increase in the slope of the stress-strain curves for both materials, when the strain rate is increased. The increase in the slope of the stress-strain curve when going from static to dynamic conditions (for the strain rates concerned) is around 100% for both materials - in agreement with previously reported results (Ochola et al., 2003).

CHAPTER 4

DEMONSTRATOR DESIGN AND TESTING

A review of the progressive damage models available for modelling of laminated composite materials (§ 1) led to the selection of the bi-phase material model for the modelling of fabric reinforced laminates. Material specimens were subsequently manufactured (using the material selected for demonstrator production) and tested (§ 3) in order to obtain the material characterisation parameters necessary for implementation of the bi-phase model in the PAM-CRASH finite element code. Model calibration runs indicated that the enlisted material parameters produce a satisfactory response for simulations involving uniaxial tensile and compressive loading. The next step in developing the modelling methodology is to simulate a laminated composite component's response to a crushing load. In order to grade the performance of the model, experimental data for the crushing of a real laminated component is required. The design, manufacture and testing of the demonstrator component necessary to obtain the essential experimental data for model validation is presented here.

4.1 Laminated demonstrator design

4.1.1 Demonstrator geometry

The geometry of the demonstrator should be complex enough that successful simulation of the demonstrator's response will provide a high level of confidence in the modelling methodology. The shape of the demonstrator component is selected to be representative of an automotive compartment such as the compartment typically used to house a spare wheel (Fig. 4.1). This provides a sufficiently complex geometry consisting of flat sections (which make up the component's rectangular base plate and circular cylinder end) and a curved cylindrical sidewall. The proposed component dimensions are shown in Fig. 4.2.

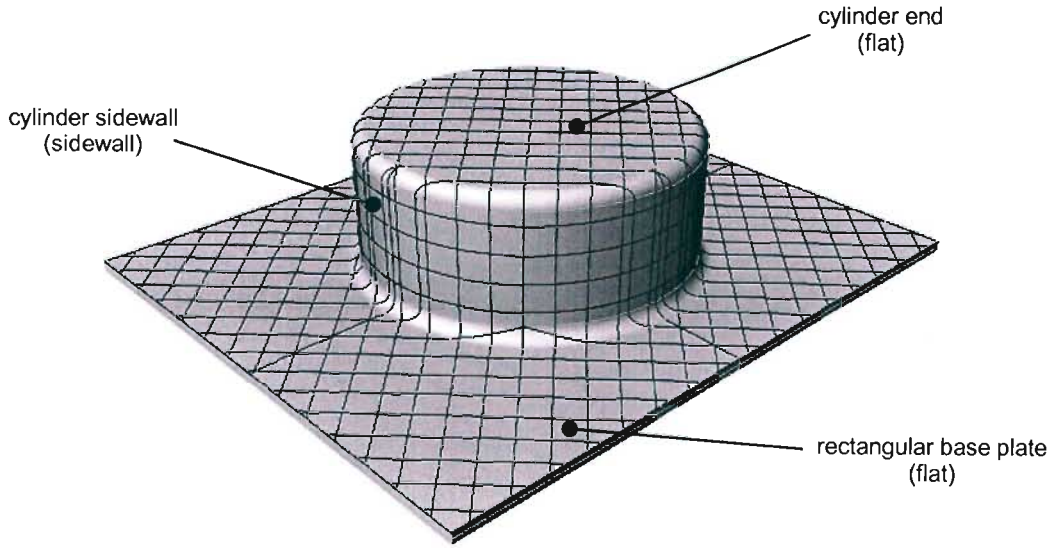

Fig. 4.1 Three-dimensional model of the prototype component

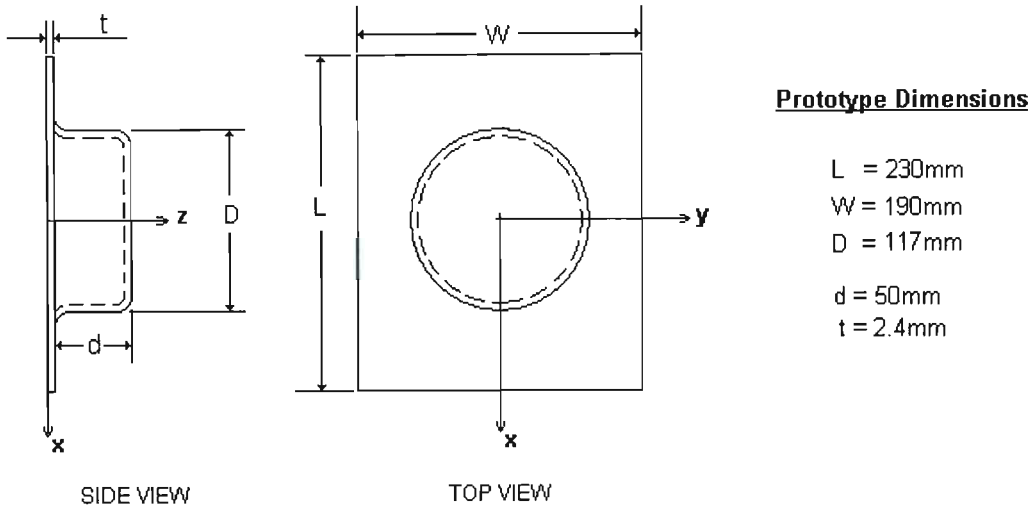

Fig. 4.2 Prototype overall dimensions

4.1.2 Design of fabric patterns

Since the laminated demonstrator component is to be used for testing so that data be made available for comparison with data obtained from numerical simulation of the demonstrator under the same conditions as the test, it is aimed to generate, by design, a structure that is repeatable and easily described using the available material models. The shape of the component is chosen for its complexity as a general automotive component, so that successful simulation of the demonstrator's response would indicate high confidence in the modelling methodology employed. With a suitable mould already available from earlier work investigating the crashworthiness of SMC components (Selvarajalu, 2003; Morozov, 2003), the development of fabric patterns and a suitable processing technique were required for production of the laminated demonstrator components.

Options for processing of the demonstrator are:

- Hand layup with hot compression moulding
- Hand layup with vacuum bagging
- Use of prepregs (fabric pre-impregnated with resin) with compression moulding
- Use of performs with a closed mould process such as RTM (resin transfer moulding)

All of these processes require the development of suitable patterns for cutting of the fabric reinforcement. The cut patterns are then either:

- Applied to the mould surface and wet with resin by hand application
- Cut from prepreg sheets and then heated in the mould for curing
- Stitched into a perform for resin injection

The development of suitable patterns and their layup to form the laminated demonstrator has been performed. Two of the options explored for building the prototype component from layers of fabric are:

1) A one piece fabric pattern, including appropriate seam lines. The pattern is made to drape over the male mould surface for the case of hand layup or use of prepregs. A preform may also be stitched together using the same basic pattern.

2) A three piece pattern with two pieces for the flats (rectangular base plate and cylinder end) and a third woven sock that may be pulled over the cylinder, to build the sidewall (see Fig. 4.1 for terminology used to describe geometry).

Two one piece patterns for the production of the laminated demonstrator component were subsequently developed. Three-dimensional views of the prototype, showing the seam lines for the two patterns (pattern A and pattern B) are provided in Fig. 4.3. The patterns' ability to drape over the quarter cylinder (between seam lines) was tested using twill weave glass fabric of 290 g/m² surface density, to confirm that this fabric will be suitable for part production. The resulting pattern profiles are shown in Figs 4.4 - 4.5. The dimensional accuracy of the patterns was tested using patterns cut from regular fabric (Figs 4.6 - 4.7). After confirming the dimensional accuracy of the patterns, templates were cut from masonite board to be used during production trials for cutting of the fabric patterns.

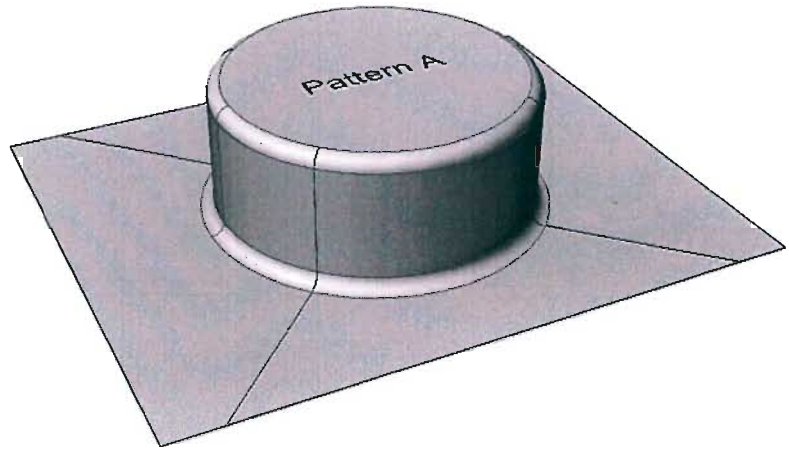

(a) Pattern A seam locations

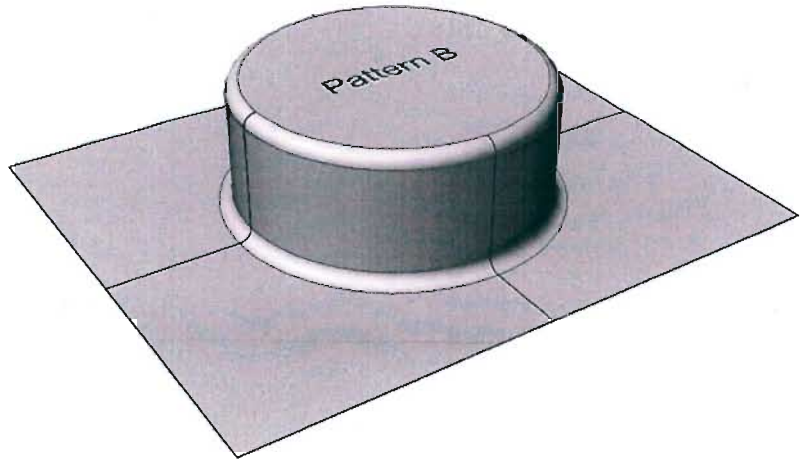

(a) Pattern A seam locations

Fig. 4.3 Seam lines for patterns A and B

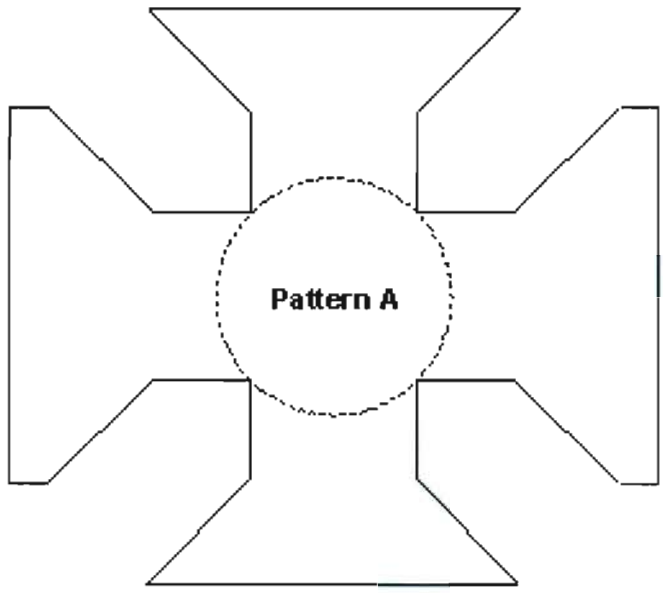

(a) Scaled pattern A

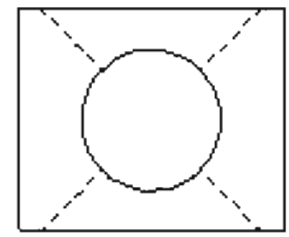

(b) Top view showing seam lines

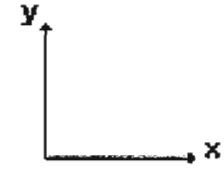

Fig. 4.4 Pattern A layout

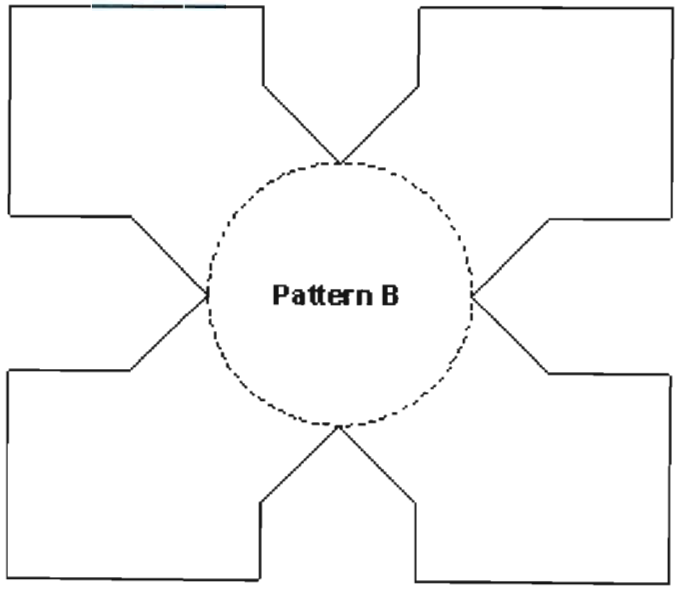

(a) Scaled pattern B

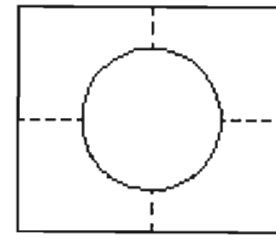

(b) Top view showing seam lines

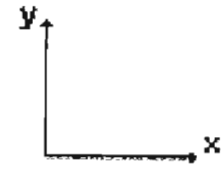

Fig. 4.5 Pattern B layout

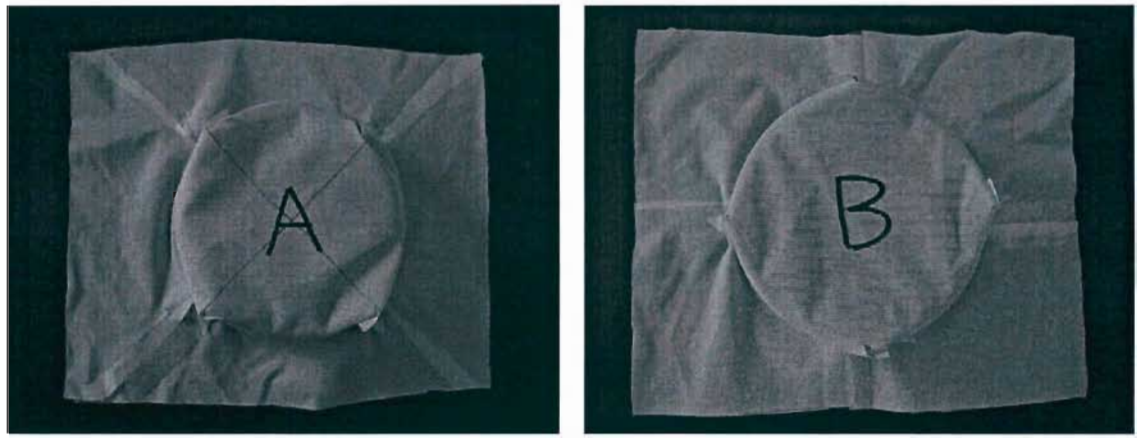

(a) Pattern A (b) Pattern B

Fig. 4.6 Top view of patterns draped over mould

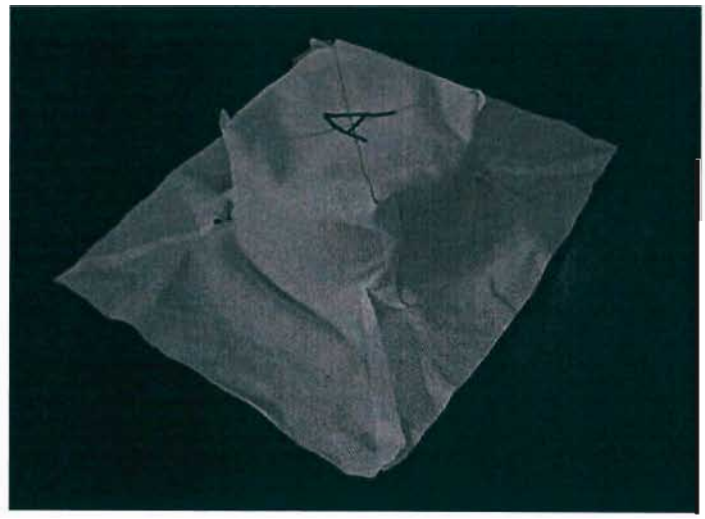

(a) Pattern A

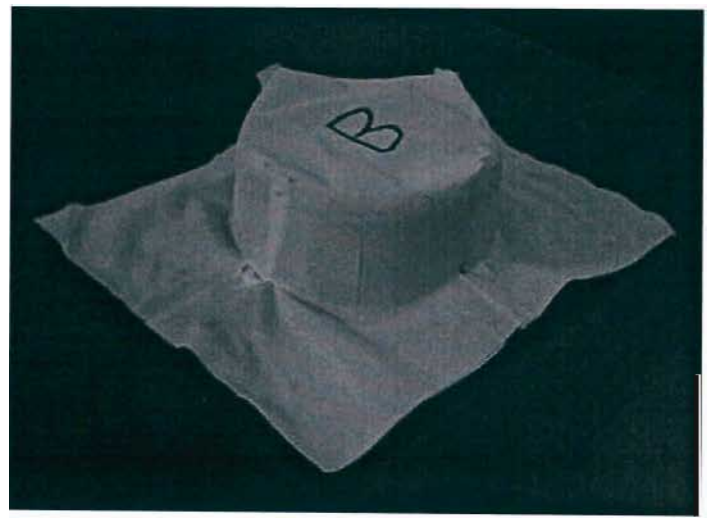

(b) Pattern B

Fig. 4.7 Perspective view of patterns draped over mould

4.1.3 Layup design and fibre orientation

In order to test the suitability of the patterns developed in § 4.1.2 for production of the laminated demonstrator, it is necessary to design the structure of the entire laminate. A symmetric laminate is preferred as numerical analysis is simplified and undesirable warping during in-plane loading is minimised. A symmetric construction also prevents warping during cooling from a higher processing temperature. Two separate coordinate systems are introduced in order to define the orientation of the fibres on separate parts of the prototype. Fibre orientation on the flat parts of the prototype (rectangular plate and cylinder end) is defined by angle ϕ_1, in terms of the *xy* Cartesian coordinate system (Fig 4.8(a)), and fibre orientation on the cylinder sidewall is defined by angle ϕ_2 (Fig. 4.8(b)), in terms of the cylindrical coordinate system shown in Fig. 4.9. Positive sense for both angles is counter clockwise. With the convention for fibre orientation defined, the following observation may be made:

- When using pattern A, fabrics with fibre orientations of 0/90° and ±45°, relative to the *x*-axis (ϕ_1), will have the same orientation on the cylinder sidewall when measured relative to the *z*-axis (ϕ_2).

- When using pattern B, the same woven fabrics will have their orientations rotated through 45°, ie: a 0/90° orientation on the flats (ϕ_1) will be transformed to a ±45° orientation on the sidewall (ϕ_2) and a ±45° orientation on the flats will be transformed to a 0/90° orientation on the sidewall. This is easily confirmed by superimposing the fibre direction on the pattern shown in Fig.4.5.

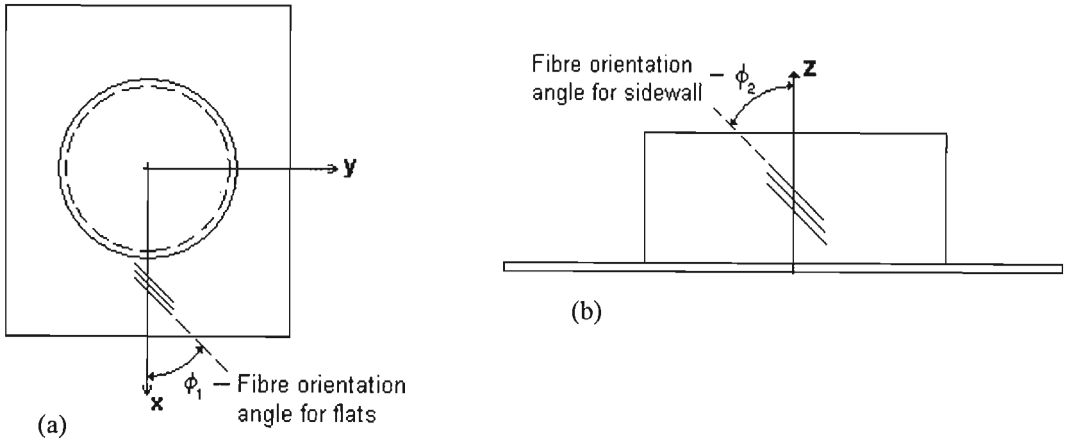

Fig. 4.8 Separate definition of fibre orientation for flats and sidewall

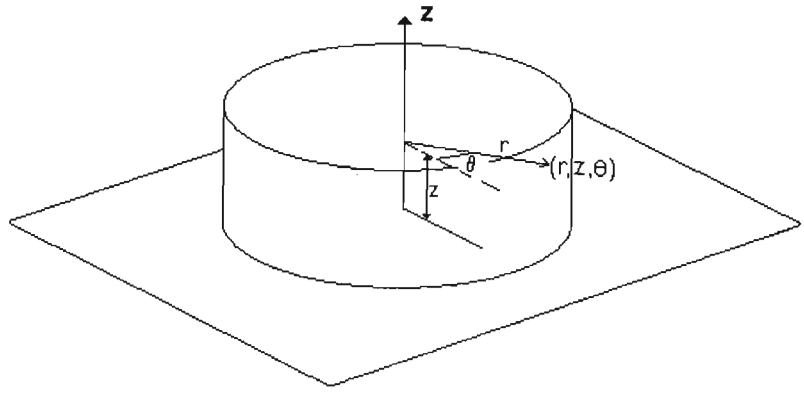

Fig. 4.9 Cylindrical coordinate system for cylindrical part of prototype

With a lamina thickness of 0.3mm (which is obtained using a locally available woven glass mat of 290g/m² surface density, at a fibre volume fraction of around 40%) it will take 8 laminae (layers) to build up a part thickness of 2.4mm.. By alternately stacking patterns A and B (except at the midplane where the same pattern is used on either side in order to conserve laminate symmetry), the following layups may be obtained:

	FLATS (ϕ_1)		SIDEWALL (ϕ_2)
1a.	$[0/90 \pm 45]_{2S}$	|	$[0/90]_8$
2a.	$[0/90 \pm 45]_{2S}$	|	$[\pm 45]_8$
3a.	$[0/90 \pm 45_2 0/90]_S$	|	$[\pm 45_2 0/90_2]_S$
4a.	$[0/90 \pm 45_2 0/90]_S$	|	$[0/90_2 \pm 45_2]_S$

or the same combinations can be reversed, giving:

	FLATS (ϕ_1)		SIDEWALL (ϕ_2)
1b.	$[0/90]_8$	|	$[0/90 \pm 45]_{2S}$
2b.	$[\pm 45]_8$	|	$[0/90 \pm 45]_{2S}$
3b.	$[\pm 45_2 0/90_2]_S$	|	$[0/90 \pm 45_2 0/90]_S$
4b.	$[0/90_2 \pm 45_2]_S$	|	$[0/90 \pm 45_2 0/90]_S$

If use of a woven sock is made, it is possible (providing the correct sock is obtained) to produce a component with the same orientation in the cylinder sidewall as obtained in the flats.

4.1.4 Designing for crashworthiness

Manipulation of the fibre orientation and reinforcement distribution over the volume of the demonstrator component can be used to control the component's response to crushing and impact loading, since variations in fibre orientation and density directly result in strength and stiffness variations over the structure. Use of different reinforcement and matrix materials, as well as employing hybrid composites (involving multiple reinforcement materials), are further ways of influencing the crush response of the composite structure. In particular, Farley et al. (1986) examined the roles of fibre and matrix on the crash energy absorption of composite tubes. Experimental work showed how the fibre and matrix ultimate strains significantly affected energy absorption. Ply stacking sequence for graphite/Kevlar hybrid laminates also significantly affected the tubes energy absorption capability. The addition of Kevlar as reinforcement was found to preserve structural integrity after crushing. The work of Schmueser and Wickliffe (1987) demonstrates increased energy absorption (per unit mass) for graphite/epoxy tubes over Kevlar/epoxy and glass/epoxy counterparts. The Kevlar/epoxy tubes also displayed more ductile accordion type buckling modes similar to soft metal tubes. So in general, the crashworthiness of a structural component can be manipulated by controlling fibre orientation, as well as fibre type and distribution over the volume of the structure.

In order to examine the effect of varied fibre orientation on the crush performance of the laminated demonstrator component, different layups employing different fibre orientations are to be selected for experimental study. Significant variations in physical response for the different demonstrators with different layups will then be sought, following which an attempt to capture these differences in the simulation output can be made. Two layups have been selected from the options developed in § 4.1.3, namely:

	FLATS (ϕ_1)	SIDEWALL (ϕ_2)
LPT1:	$[0/90]_8$	$[0/90\ \pm45]_{2S}$
LPT2:	$[0/90\ \pm45]_{2S}$	$[0/90]_8$

The third option employs only pattern B, so that the seam locations will be void of fibre reinforcement. This is to promote an alternative deformation mode that may experience a significantly varied load response. Description of option 3 is as follows:

	FLATS (ϕ_1)	SIDEWALL (ϕ_2)
LPT3:	$[0/90]_8$	$[\pm45]_8$

The above notation shows the warp and weft direction together, as a single fabric layer has been represented as a 0/90 or ±45 stackup. This notation can be simplified by only indicating the warp orientation, the weft orientation for the orthogonally woven fabric is then automatically known. This results in the following simplified notation to describe the three alternative demonstrator constructions, where the indicated angle shows the orientation of the ply warp fibres relative to the relevant reference axis (see Fig. 4.8):

	FLATS (ϕ_1)	SIDEWALL (ϕ_2)
LPT1:	$[0]_8$	$[0\ 45]_{2S}$
LPT2:	$[0\ 45]_{2S}$	$[0]_8$
LPT3:	$[0]_8$	$[45]_8$

Another alternative notation contains information on the pattern employed and the orientation of the warp fibres relative to the *x*-axis when cutting and placing the pattern. Such a notation is more practical for manufacturing schedules since the pattern stacking sequence and pattern orientation for cutting is immediately evident in the code:

LPT1:	$[A_0\ B_0]_{2S}$
LPT2:	$[A_0\ B_{45}]_{2S}$
LPT3:	$[B_0]_8$

This provides three different constructions for production of the laminated demonstrator component namely: LPT1, LPT2 and LPT3. The pattern stacking sequences associated with each construction are as described above. These different constructions will be tested with the aim of observing significant differences in the recorded response which may manifest as a varied load-time or load-displacement response, as well as varied deformation modes, associated with the varied load response. Capturing of any observed differences in the modelling environment then serves to increase confidence in the instated modelling methodology.

4.2 Laminated demonstrator production

In developing the process to be used for laminated demonstrator production, various options were explored (Fig. 4.10), including open layup on a cold mould, cold vacuum bagging, hot vacuum bagging and closed mould processing. A component produced using the vacuum bagging process is shown (Fig. 4.11) as well as a closed mould component (Fig. 4.12) produced using the closed mould process detailed in Fig. 4.13. Use of hand layup to position the separate material constituents was also compared with the use of prepreg material. The prepreg material did not conform well to the part surface and so hand layup was preferred over use of prepregs.

The quality of part obtained through vacuum bagging and closed mould production is higher than for open layup. A hot process is also preferred as curing time is reduced and fibre wet out is improved. Selection of the process to be used for further laminated prototype production requires consideration of a number of factors. With the choice being between hot vacuum bagging and a hot closed mould process, hot vacuum bagging is preferred since the process is easier to implement and less labour intensive. Although control over part thickness is higher for the closed mould process, problems with entrained aired occurred. These problems could possibly be eliminated using a resin transfer process (with a closed mould) but this option would be expensive in terms of both time and cost, since further development of the tooling and production process would be required. After some initial testing of the vacuum bagged components, sufficient repeatability in the experimental force-displacement data (which is for comparison with simulation output) was observed. Hot vacuum bag processing was thus selected for the further production of laminated prototypes for the purpose of this research.

Various material systems were tested for demonstrator production (Tables 4.1 - 4.2) and the final choice was to use the Ampreg 20 epoxy resin with 2×2 twill weave glass fabric reinforcement of 290 g/m² surface density. The selected resin is well suited to the hot vacuum bag process and the chosen fabric conforms well to the mould surface during processing.

Table 4.1 Resin systems tested (*AMT, South Africa*)

PROPERTY	UNITS	LR 20	Ampreg 20	916 Prepreg
Compressive Strength	(MPa)	100	-	151.7
Tensile Strength	(MPa)	53	75.2	50
Tensile Modulus	(GPa)		3.81	4.17
Flexural Strength	(MPa)	110	-	92
Flexural Modulus	(GPa)	3	2.58	3.78
Elongation at Break	%	3.3	1.7	1.4
Density	g/cm^3	1.1	1.176	1.30

Table 4.2 Glass reinforcement used with respective resins (*AMT, South Africa*)

PROPERTY	UNITS	LR 20	Ampreg 20	916 Prepreg
Type	-	E-glass	E-glass	E-glass
Weave	-	2/2 twill	2/2 twill	8H Satin
Surface Density	g/m²	290	290	300
Laminate thickness	mm	0.29	0.29	0.30

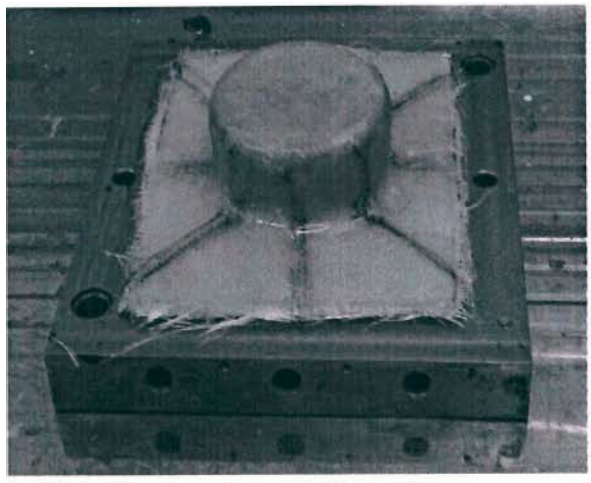

(a) open layup

(b) cold vacuum bagging

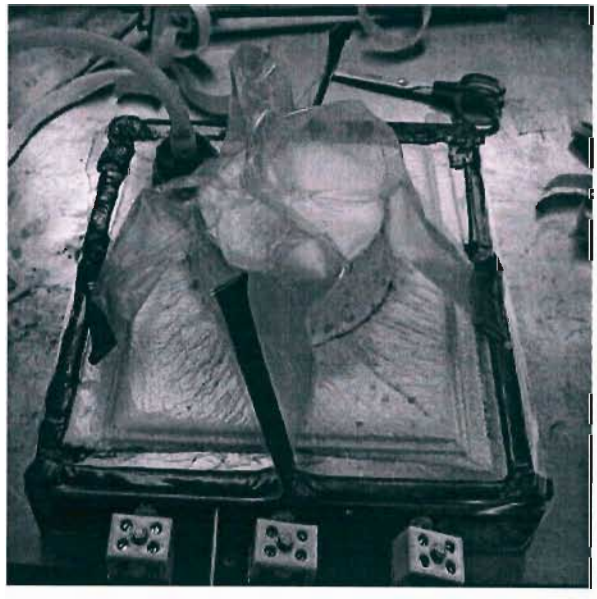

(c) hot vacuum bagging

Fig. 4.10 Alternative processing options for laminated demonstrator

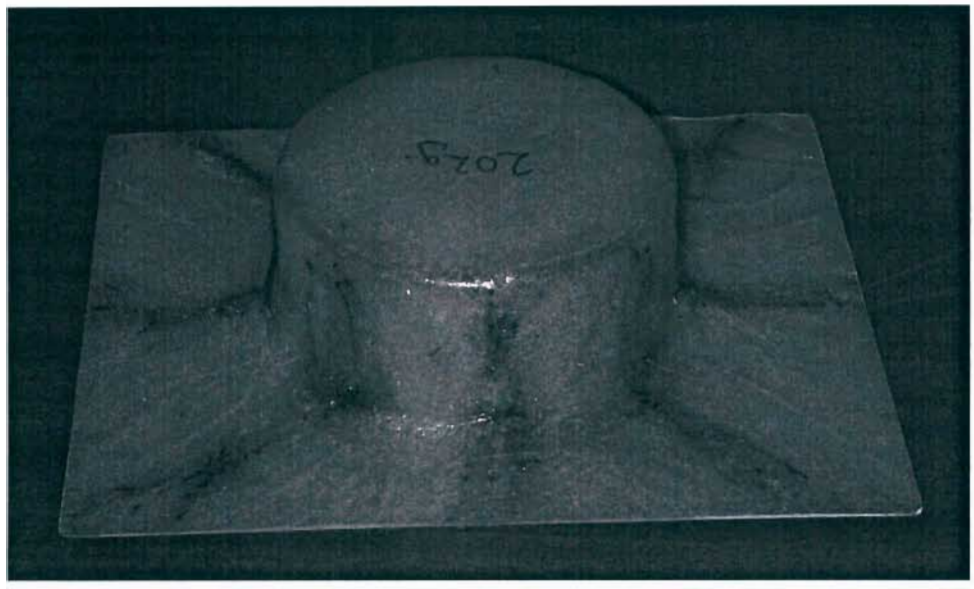

(a) Upper surface

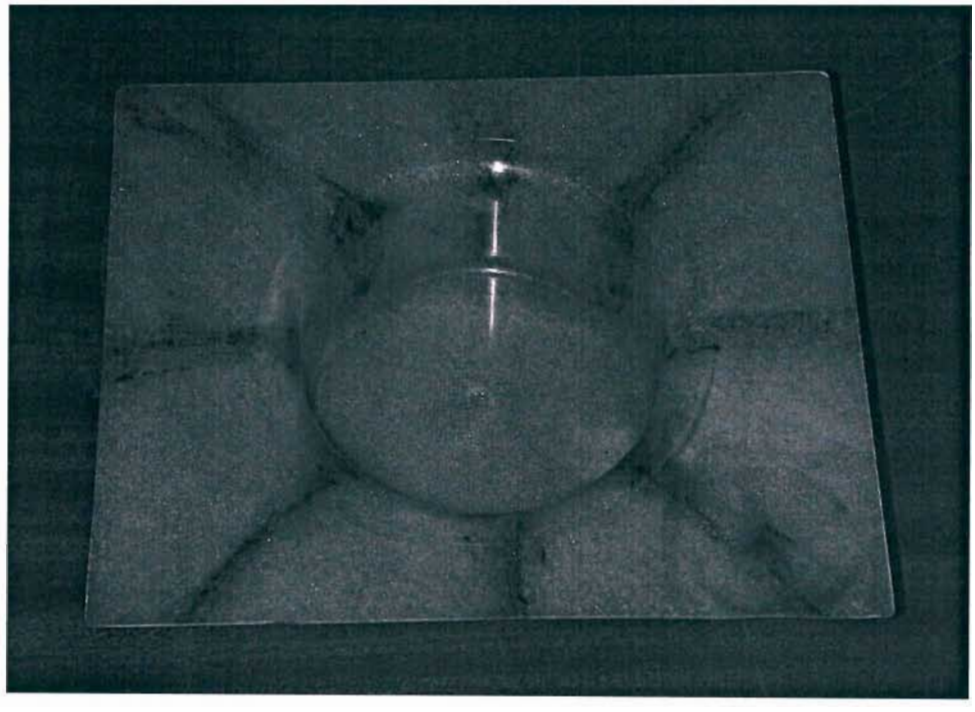

(b) Lower surface

Fig. 4.11 Vacuum bagged component

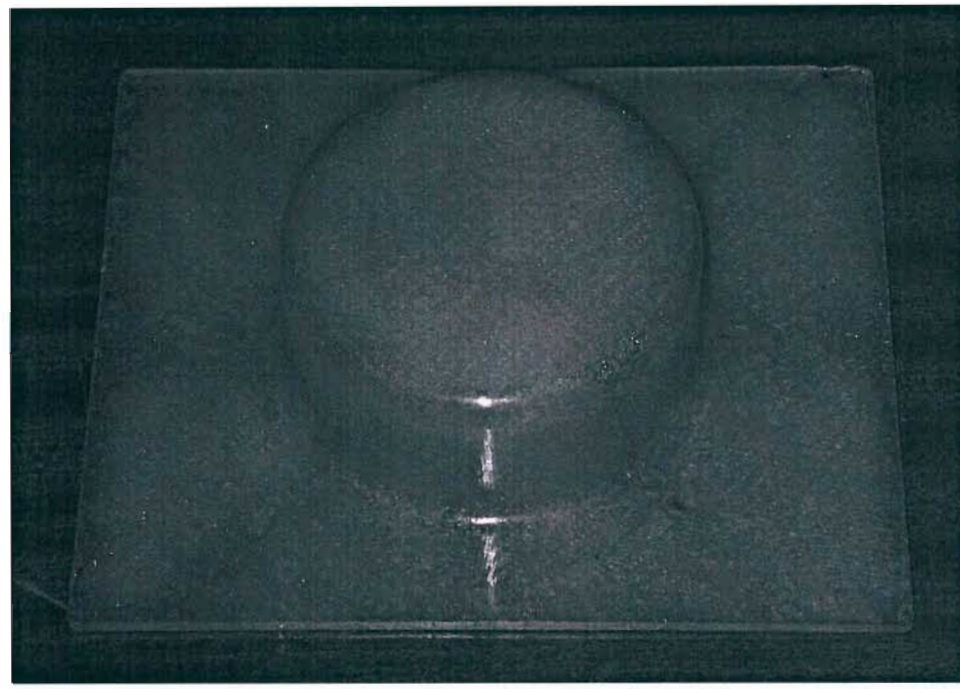

(a) Upper surface

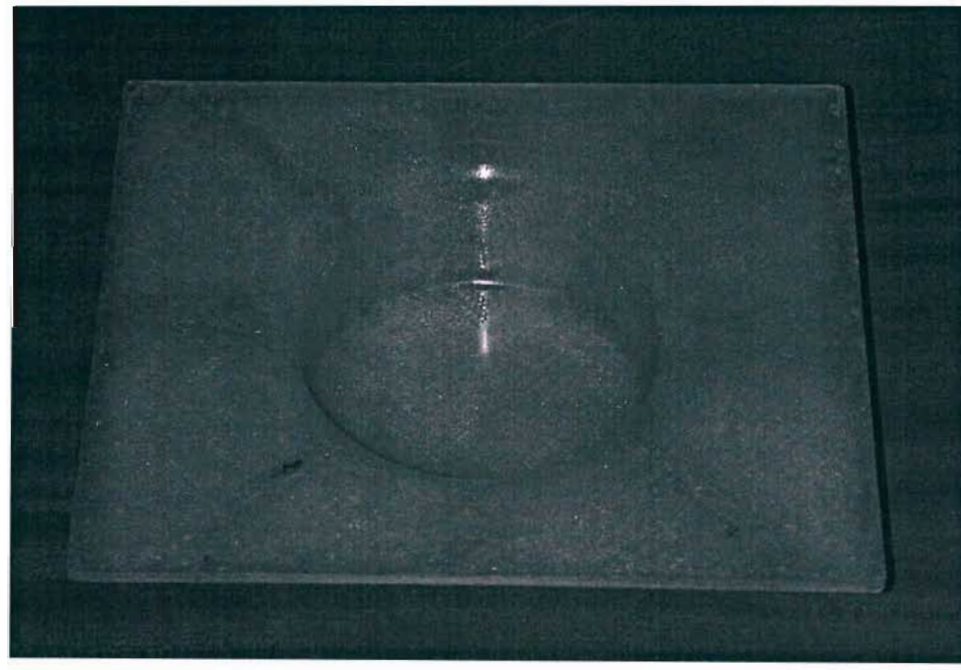

(b) Lower surface

Fig. 4.12 Closed mould laminate

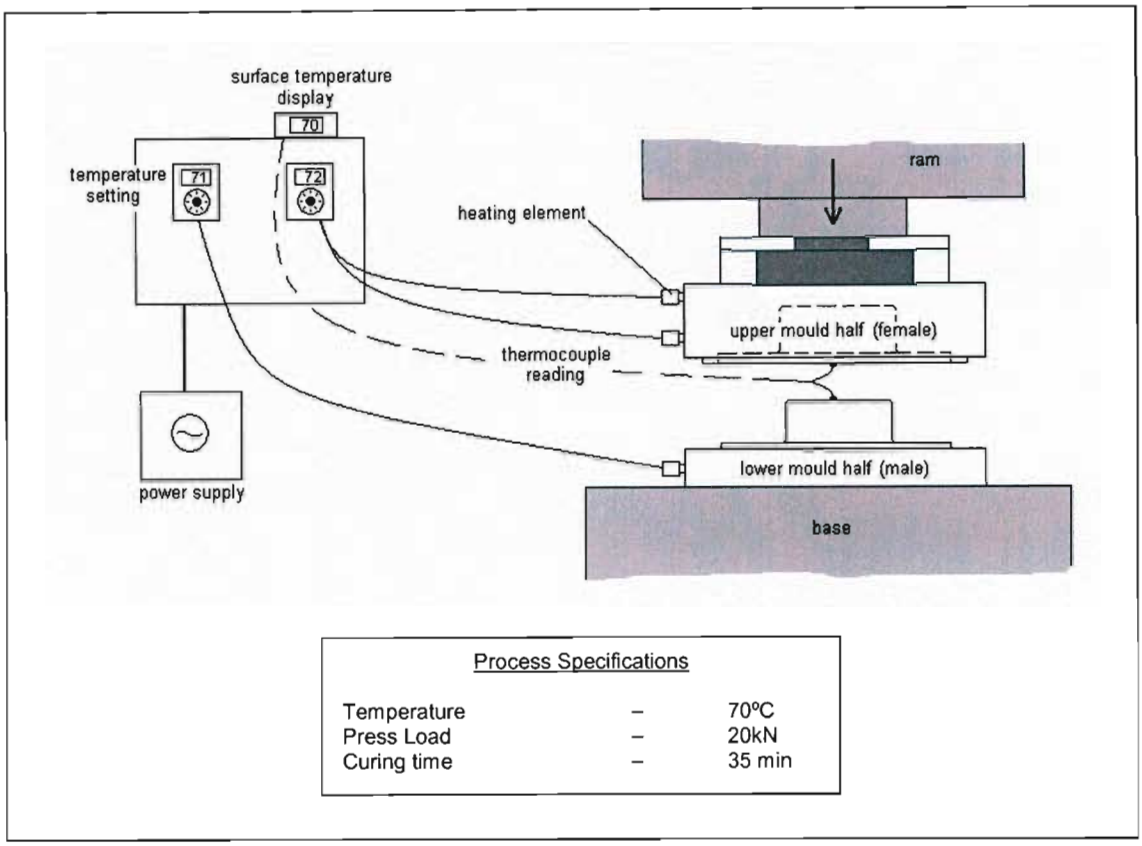

Fig. 4.13 Closed mould laminated demonstrator production process

4.2.1 Hot vacuum bag processing

Production trials exploring the use of different production processes (and materials) led to the selection of hot vacuum bagging employing E-glass fabric 1102 as reinforcement (suppliers *AMT, South Africa*, see Table 4.3) and Ampreg 20 epoxy resin as the matrix material (*SP systems International*, see Table 4.1) for production of laminated demonstrator components. The production of the demonstrator component LPT1 (§ 4.1.4) by hot vacuum bagging is demonstrated below. The patterns cut from the 290 g/m² balanced glass fabric, using masonite templates and a rolling fabric cutter, are shown in Fig. 4.14. The demonstrator production, from mould preparation to cured component, is illustrated in Figs. 4.15- 4.18 and the processing parameters are provided in Table 4.4.

Table 4.3 1102 glass fabric reinforcement specifications (*AMT, South Africa*)

Fabric Specifications: 1102 E-Glass	
Fibre designation	EC 9 68x3
Fabric weave	2 x 2 twill
Fabric weight	290g/m²
Warp / weft	Balanced - 50% / 50%
Thread count	7
Flexural Modulus **	18000MPa
Flexure Strength **	500MPa
Lamina thickness **	0.29mm

** for 40% fibre volume fraction epoxy laminate

Table 4.4 Parameters for hot processing of Ampreg 20 resin

Ampreg 20 Processing Parameters	
Cure temperature:	70 °C
Cure time:	35 min
Vacuum pressure:	0.8 bar

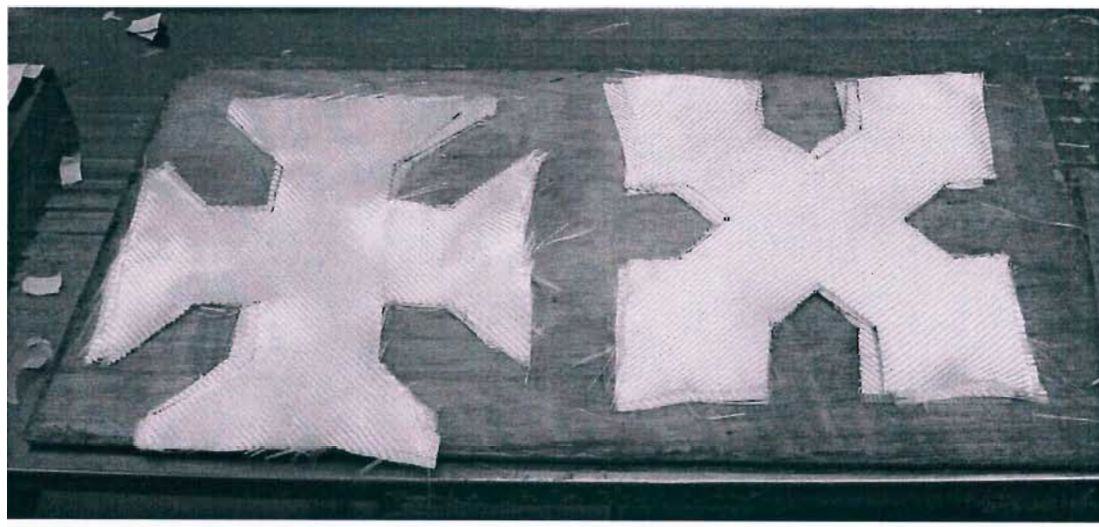

Fig. 4.14 Glass fabric patterns ready for laminating

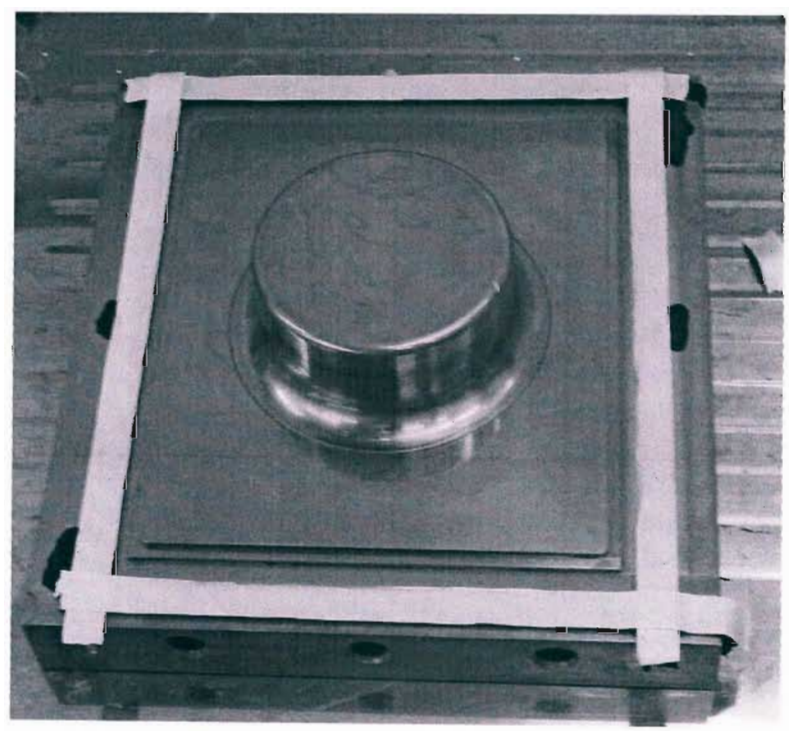

Fig. 4.15 Mould ready for laminating

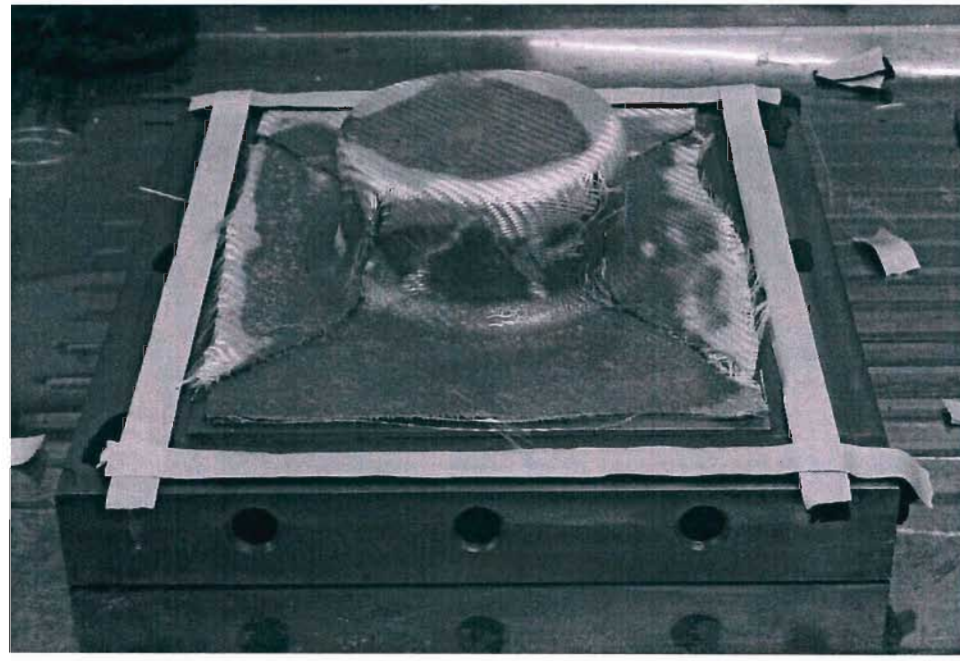

(a) First layer

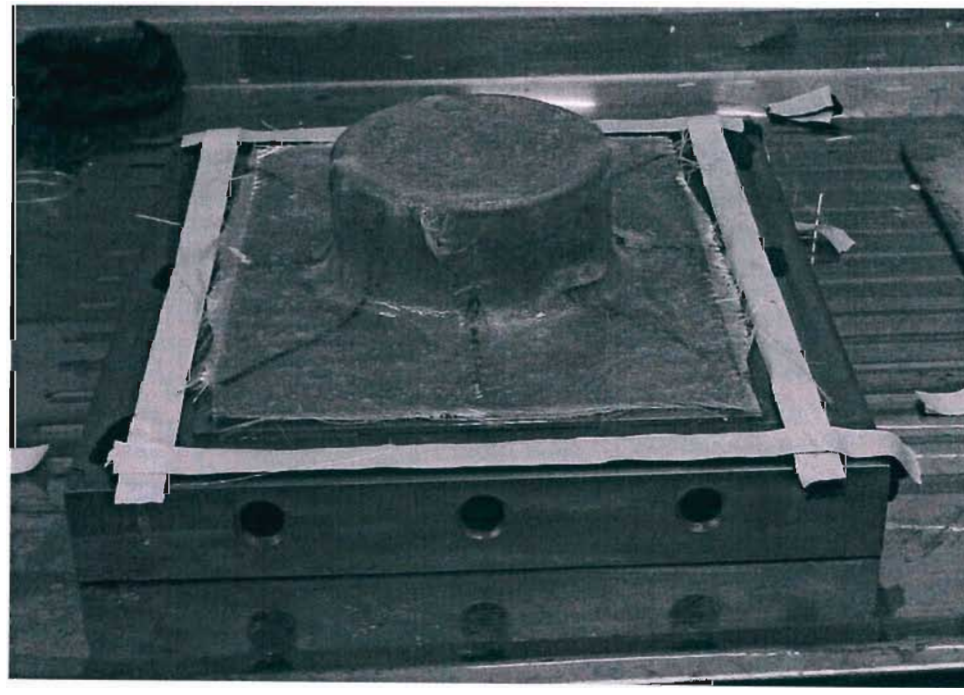

(b) Second layer

Fig. 4.16 Layup of fabric patterns

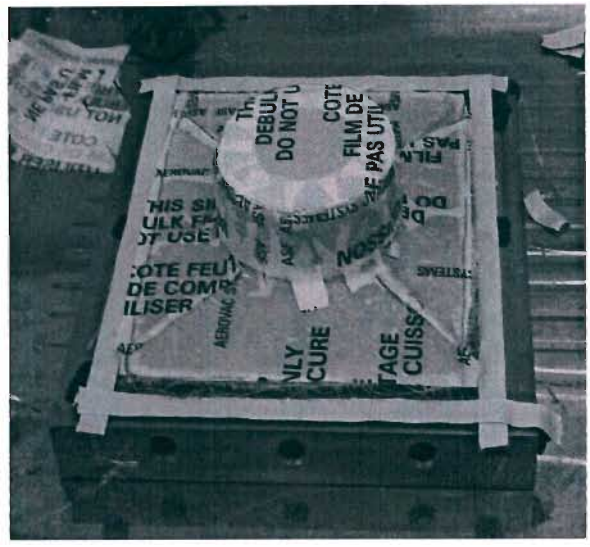

(a) Release ply in place

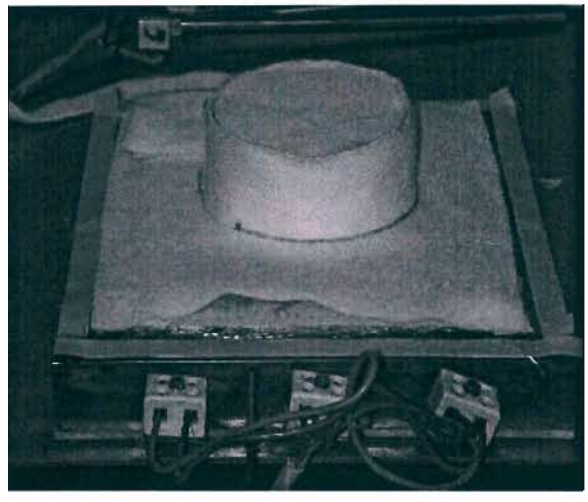

(b) Breather cloth added

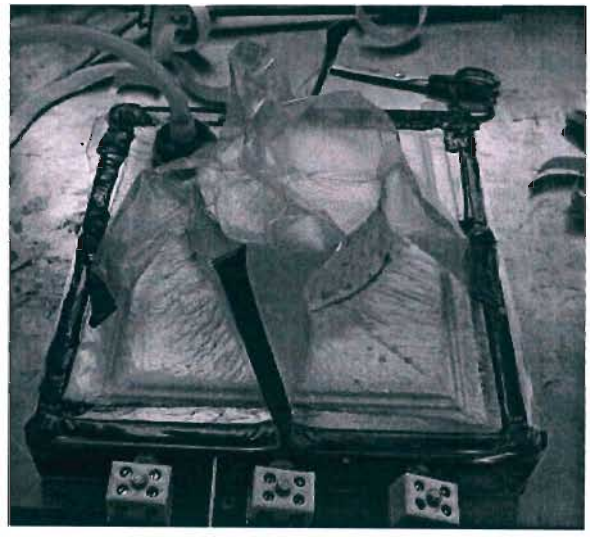

(c) Vacuum bag assembled

Fig. 4.17 Hot vacuum bagging of Ampreg 20 component

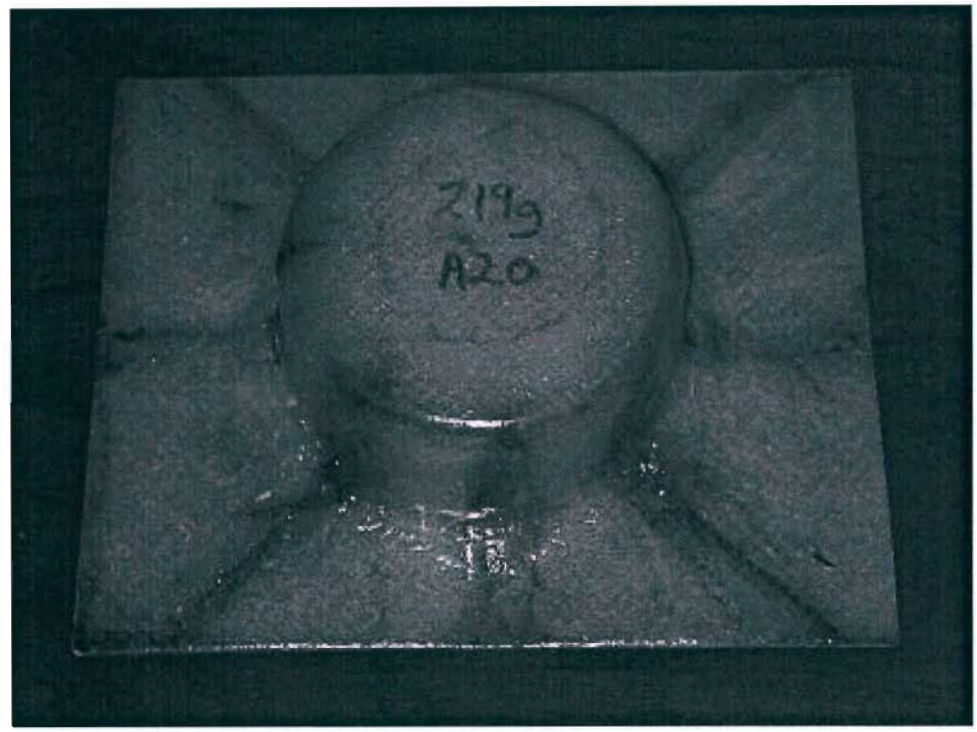

(a) Upper surface

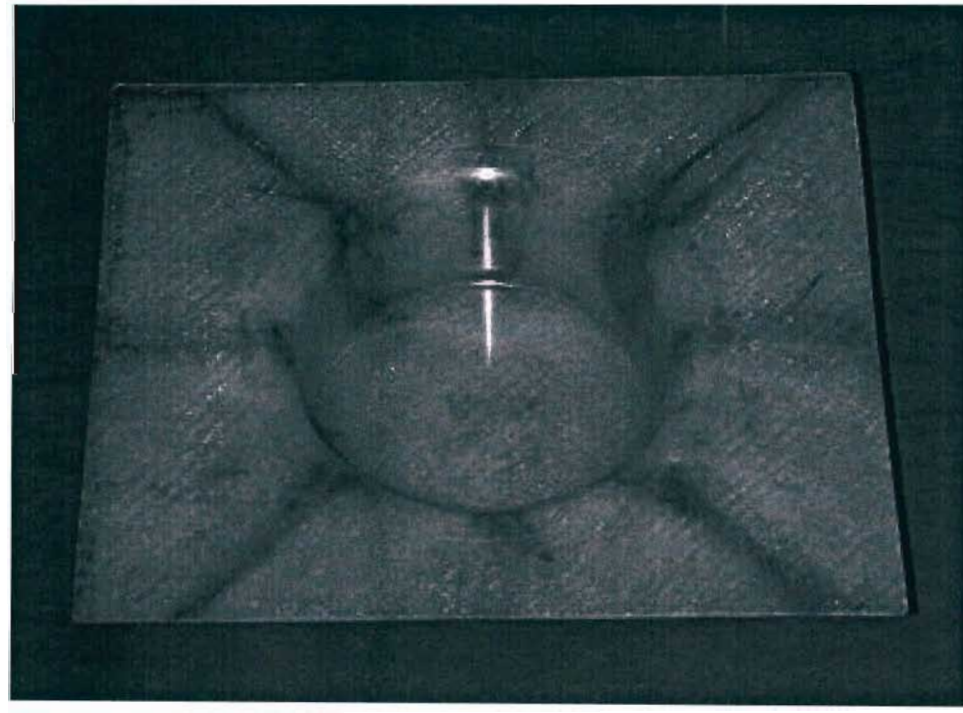

(b) Lower surface

Fig. 4.18 Hot cured Ampreg 20 component

4.3 Demonstrator testing

Demonstrator testing is necessary since the data obtained is to be used to evaluate the performance of any instituted numerical models. The primary data obtained from the test is presented as a force-displacement curve which shows the maximum load the component can withstand before failure and demonstrates the component's ability to sustain load during the impact/crushing process. In order to generate experimental data for different constructions (layups) of the laminated demonstrator, three constructions were selected and described in § 4.1.4. Six prototypes from each construction (LPT1, LPT2, LPT3) were prepared for testing and have been tested under the following separate loading cases (v is the velocity of the moving grip responsible for crushing of the prototype being tested):

Case1:	$v = 2.4$ mm/s
Case 2:	$v = 150$ mm/s
Case 3:	$v = 344$ mm/s

The coding system shown in Fig. 4.19 is used to distinguish between the results for the different constructions and load cases.

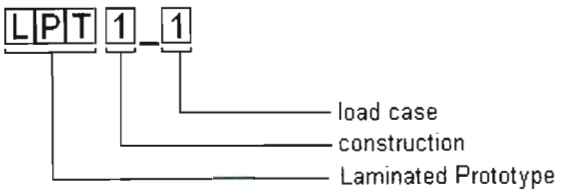

Fig. 4.19 Prototype coding system

Testing of the prototypes under a crushing load (aligned with the plane of the demonstrator base plate) is accomplished using an MTS servo-hydraulic testrig (Fig. 4.20) incorporating the MTS Model 312.21 Load Frame (S/N 1510) in combination with the MTS 458.10 Microconsole. Output from the microconsole is sent to a Wavebook 516 data acquisition system which logs the data using integrated software via the PC's Enhanced Parallel Port (EPP). The recorded data from each test is available as a set of load and displacement data sampled at a constant sampling rate.

In order to prescribe the velocity of loading for the crushing of the prototype it is necessary to use displacement feedback (Fig. 4.21). The displacement feedback from the LVDT (Linear Variable Differential Transformer) is compared to the program input and the error signal (difference between the two) is used to drive the servo-valve, which in turn drives the hydraulic actuator responsible for loading the component being tested. In order to apply constant velocity loading of the prototype in compression, it is necessary to input a ramp signal to the controller which requires input of the ramp start and end positions, as well as the ramp rate (mm/s).

The load and displacement data recorded during the test are then processed and available for plotting. In order to make reading and interpretation of the data easier, a colour coding system is introduced. When comparing how component structure influences load response, by looking at comparative force-displacement plots, separate colours are assigned to the curves for each construction (LPT1 – **Black**, LPT2 – Blue, LPT3 – **Red**, Fig. 4.22). When comparison of results is made in order to see the effect that loading rate has on an individual constructions response, different shades of the component colour are used to represent different load cases (Fig. 4.23).

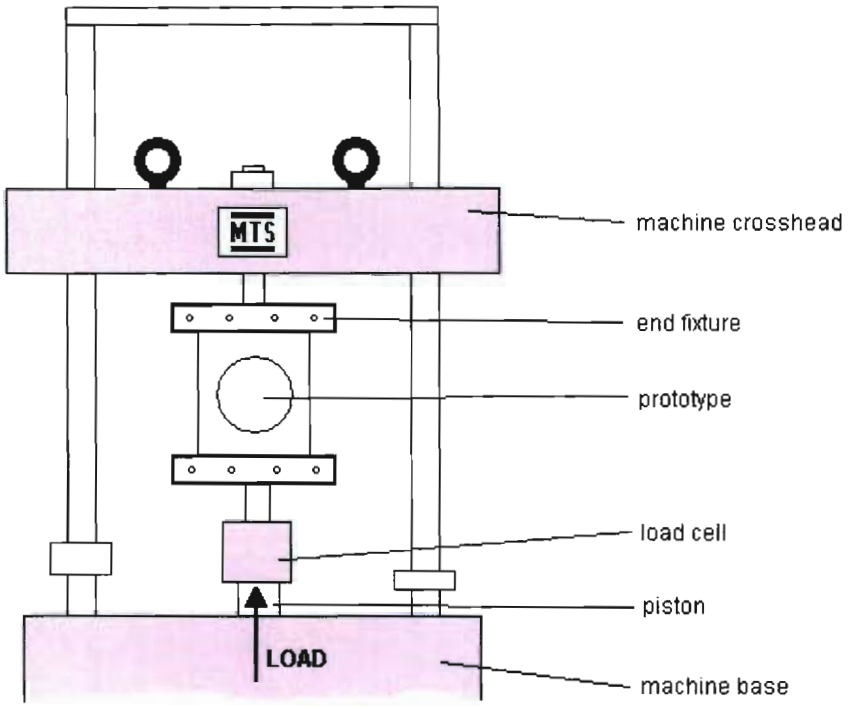

Fig. 4.20 Prototype test setup

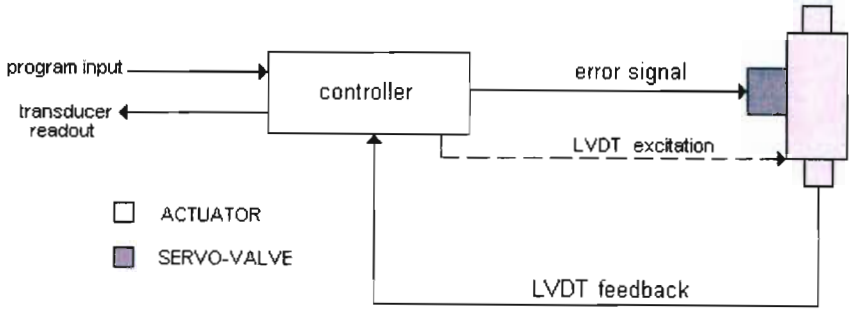

Fig. 4.21 Actuator control

Case 1	Case 2	Case 3
LPT1	LPT1	LPT1
LPT2	LPT2	LPT2
LPT3	LPT3	LPT3

Fig. 4.22 Colour coding - effect of structure

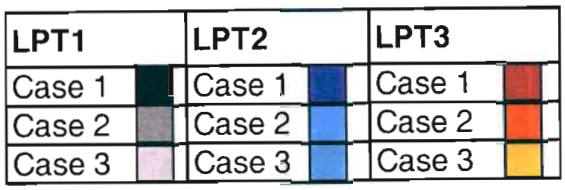

Fig. 4.23 Colour coding - effect of load rate

The comparative force-displacement plots of Fig. 4.24 show how the responses of the different demonstrators compare under the same load case. Component LPT2 is consistently stronger than the other two constructions, displaying a peak of around P_2 = (8mm, 9kN) for all three load cases. Atypical behaviour has been observed for component LPT3, case 2, which peaks at lower displacement than all other components tested. Neglecting the atypical curve, the general force-displacement response of the remaining two demonstrators, LPT1 and LPT3, are close to each other, peaking at around $P_1 = P_3$ = (6mm, 7kN). A trend of increased load oscillations with increased rate of loading is also observed for all laminated prototypes tested.

The comparative force-displacement plots of Fig. 4.25 show how the increased rate of loading affects the response for a given construction. For all three constructions the response to increased loading rate is similar to the low speed response for that construction (within the range of velocities tested) and higher oscillations in the load are seen at higher loading rates (the low velocity curve is smoother). Generally a more abrupt failure is observed for components LPT1 and LPT2 at the higher loading rate (case 3). Component LPT3, however displays a more gradual load reduction at the higher rate (Fig. 4.24(c)). Examination of deformation states from video data (Fig. 4.26) shows how the LPT3 demonstrator experiences gradual membrane tearing at the central seam locations which are void of fibre reinforcement, promoting gradual folding of demonstrator LPT3. Demonstrators LPT1 and LPT2 experience more brittle failure with no gradual membrane tearing failure being evident. This demonstrates how the inclusion of a weakened seam location has promoted a more gradual failure for demonstrator LPT3, crushed at higher velocity in the range $2.4 \leq v \leq 344$ mm/s.

A further record of the laminated demonstrators' response to the implemented load cases is provided by photographs showing the failure patterns for the demonstrators recovered after testing (Fig. 4.27). Also shown are line drawings of the particular failure patterns which provide a schematic representation of the failure. For all constructions, the existence of selectively reinforced seams appears to influence the deformation and failure patterns. Cracks migrate towards seam corner points (from the edge of the demonstrator) and favour propagation along the cylinder sidewall seamlines. This suggests the inclusion of these seams in the finite element model as a separate material zone with its own properties to be able to more accurately predict the demonstrator response. This observation also suggests how the designer may employ such selective fibre distribution in order to promote a more favourable deformation mode during a crash event that is capable of gradually reducing the crushing load whilst absorbing higher levels of energy.

Two deformation states extracted for LPT1 (loaded at 150mm/s) show how the edge of the demonstrator's baseplate snaps from one deformation mode (Fig. 4.28, s_1 = 1.9 mm) to another deformation mode (s_2 = 3.8 mm). After the transition the deformation of the demonstrator is anti-symmetric about the mid-plane (a reversed symmetry exists). This anti-symmetric deformation is the typical deformation mode observed early on in the test before major material damage develops, for all the demonstrator constructions that have been investigated here. The failure and post failure behaviour of the demonstrator is then influenced by the particular material architecture, as is the response for higher loading rates.

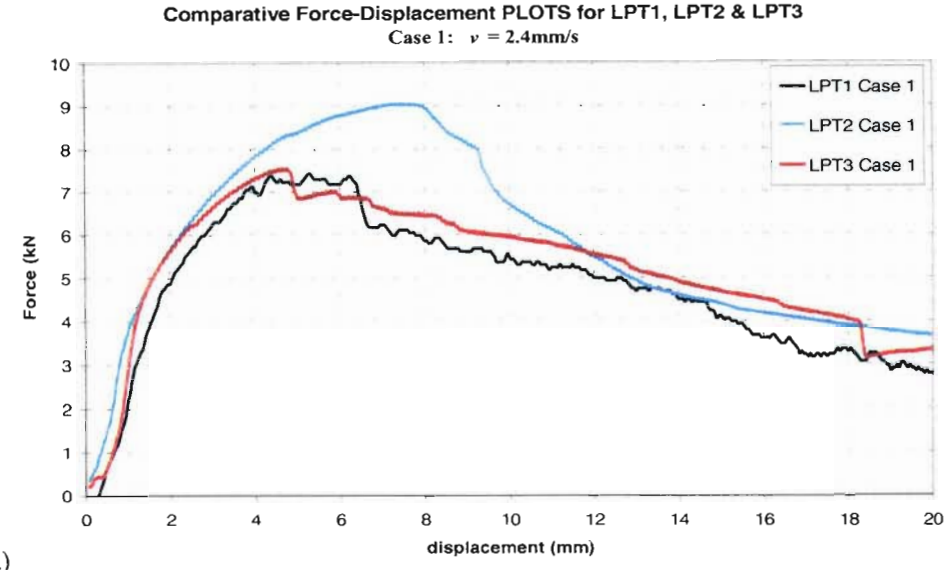

(a)

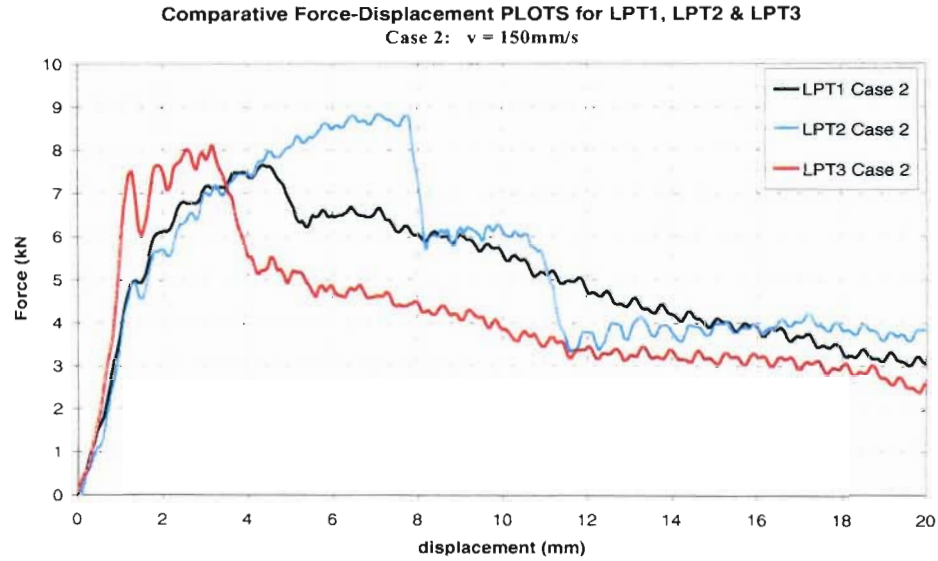

(b)

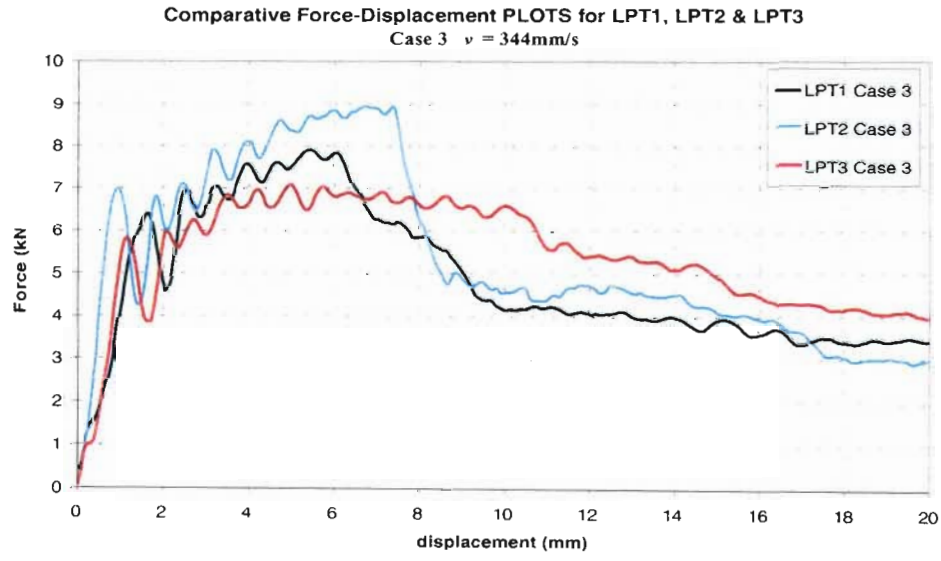

(c)

Fig. 4.24 Effect of construction on component response

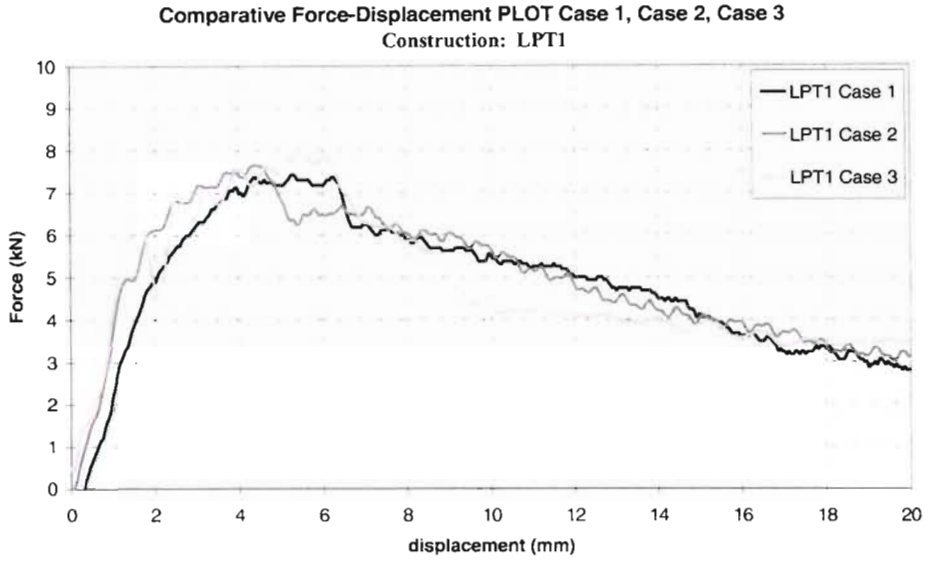

(a)

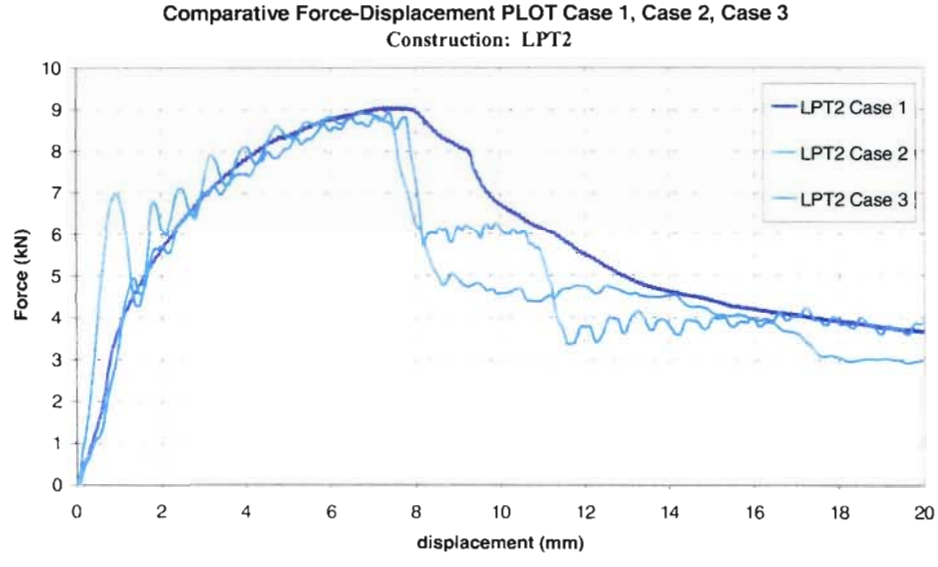

(b)

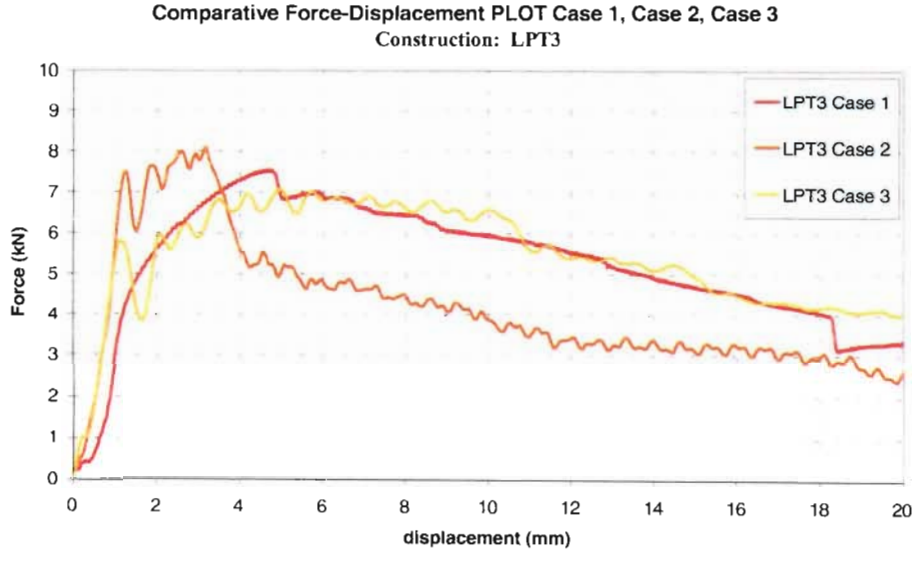

(c)

Fig. 4.25 Effect of loading rate on component response

S_1 = 4.3 mm S_2 = 8.6 mm S_3 = 12.9 mm S_4 =17.2 mm

(a) LPT1 deformation states

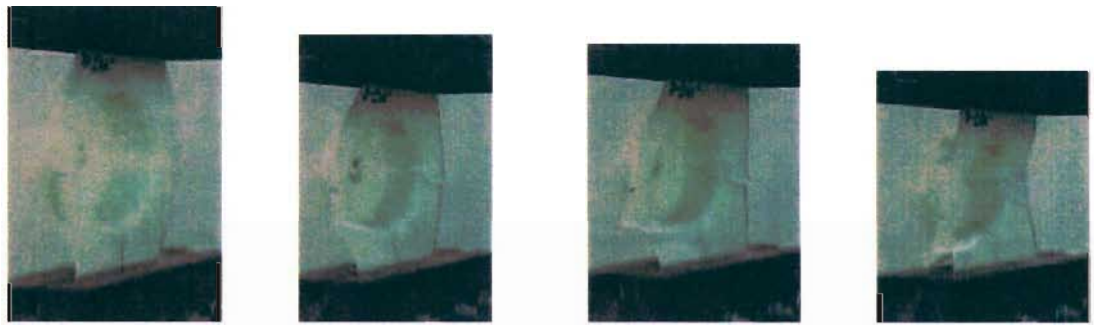

S_1 = 4.3 mm S_2 = 8.6 mm S_3 = 12.9 mm S_4 =17.2 mm

(b) LPT2 deformation states

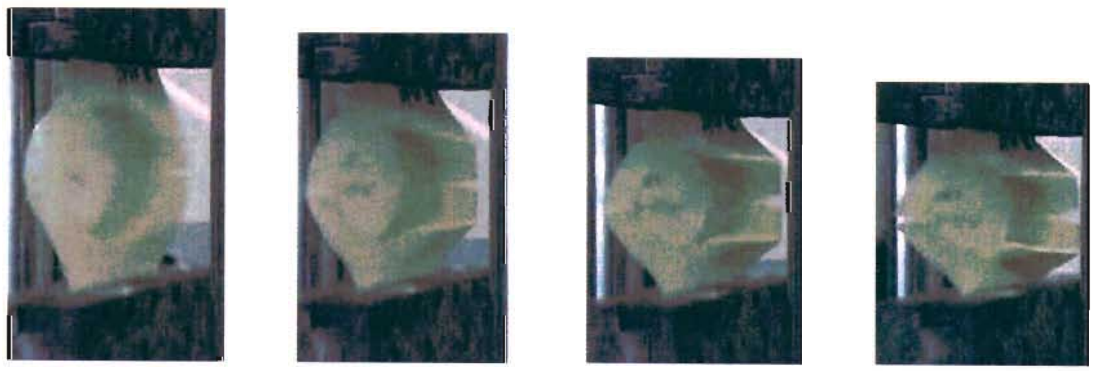

S_1 = 4.3 mm S_2 = 8.6 mm S_3 = 12.9 mm S_4 =17.2 mm

(c) LPT3 deformation states

Fig. 4.26 Comparison of deformation modes for laminated demonstrators LPT1, LPT2 and LPT3

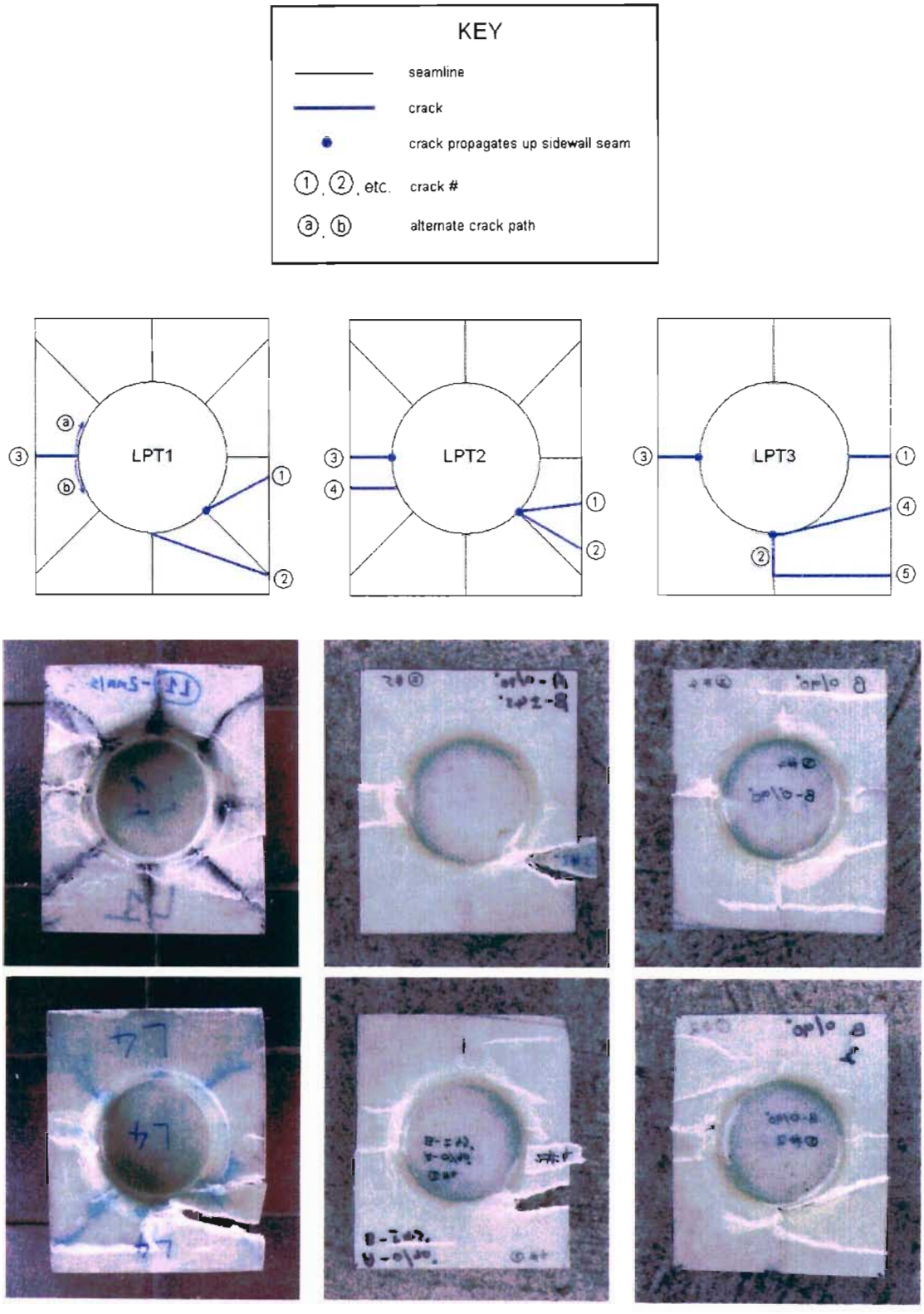

(a) LPT1 (b) LPT2 (c) LPT3

Fig. 4.27 Typical failure patterns for Demonstrators LPT1, LPT2 and LPT3
($2.4 \leq v \leq 344$ mm/s)

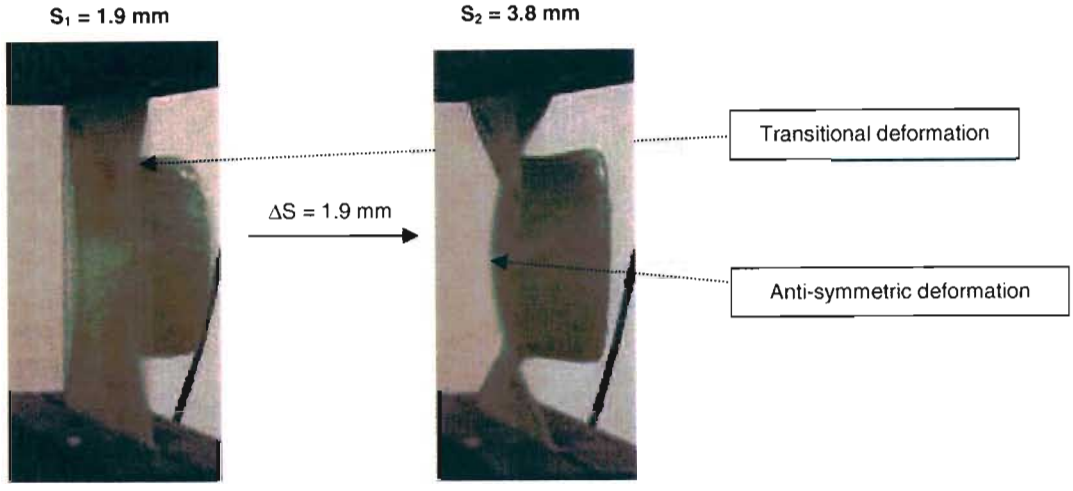

Fig. 4.28 Evidence of transitional deformation mode, LPT1 case 2 (v = 150 mm/s)

4.4 Conclusions

The successful adaptation of existing tooling (used to produce an SMC prototype component representative of an automotive spare wheel holder) for the production of a laminated prototype (with the same geometry) has been completed. Minimal modification to the tooling was required and (after modification) the same tooling is capable of producing SMC and laminated components. With the focus being on the development of the laminated demonstrator, one piece patterns were developed with the goal of controlling the fibre orientations obtained in the final product. Effective control of the fibre orientation over the component's surface allows for accurate description of the laminate construction for modelling. Three different laminated demonstrator constructions were developed (LPT1, LPT2, LPT3) to investigate the effect of fibre orientation and distribution on the demonstrator's load response.

In developing the process to be used for further laminated prototype production, various options and materials were explored, including open layup on a cold mould, cold vacuum bagging, hot vacuum bagging and closed mould processing. Vacuum bagging and closed mould production were shortlisted due to better part quality and a hot process was preferred because of the inherent improvement in fibre wet out and reduction of resin curing time associated with hot processing. Hot vacuum bagging was finally selected as it is a more practical way of producing laminated components. Although the vacuum bagged component has less uniform thickness when compared to closed moulding, early testing indicated sufficient repeatability of the vacuum bagged demonstrator's load response.

Following the production of a batch of laminated demonstrator components, testing of the laminated prototypes LPT1, LPT2 and LPT3 has been completed using an MTS servo-hydraulic rig at loading rates of 2.4 mm/s, 150 mm/s and 344 mm/s. Distinct differences in the failure patterns for the three different constructions has been observed and documented. The influence of seamlines on the demonstrator response has been observed, specifically the introduction of a fibreless seam has been observed to promote gradual membrane tearing for laminated demonstrator LPT3, as opposed to brittle cracking and folding for LPT1 and LPT2. The prevalence of gradual tearing can be advantageous for crash energy absorption. The effect of fibre orientation has also been observed in the experimental results where a higher strength for demonstrator LPT2 is reported.

CHAPTER 5

DEMONSTRATOR MODELLING

The culmination of the research involves modelling of the demonstrator's response to the conditions enforced during experimental investigation of the component's physical response. A comparison of the simulated output with the experimental observations then provides a means of evaluating the model's performance and forms a basis for model validation. Earlier work involved the careful selection of specimens to characterise the elementary ply that is used in the construction of the laminated prototype. Material specimens were then tested and the material characterisation for implementation of the bi-phase model was based upon the experimentally observed material behaviour (§ 3). Material model calibration, involving simulation of tensile and compressive tests indicated that the enlisted material characterisation parameters did indeed replicate the experimentally observed tensile and compressive material response with acceptable accuracy. This follows the procedure (outlined in § 1.3) for implementation and validation of the modelling methodology, i.e.: material characterisation and material model calibration have been completed and the next step is to validate the model for the demonstrator component.

5.1 Finite element model development

Preprocessing of the problem is an important part of the modelling process as pre-processing involves setting up the model description in an accurate and consistent way that is aimed at producing simulation results that are close to the experimentally recorded response (within the accuracy of the solver). Firstly, the spatial model of the component's geometry is generated based on the real dimensions of the part, foresight at this early stage of model development can help significantly in producing a better finite element mesh structure. Following creation of a suitably representative spatial model, the geometry must be discretised into a grid of finite elements through the creation of a suitable finite element mesh. The mesh is an array of nodal points (in space) with associated relationships determined by the underlying finite element type (brick, shell, rod, etc.) and geometrical connections. Once the mesh file has been created, application of the problem boundary conditions (which describe the load case) is made to the mesh and a solver input file is generated. The combination of software packages used to complete preprocessing of the problem is listed.

Rhinoceros 3D	- generate geometry and export IGES geometry file
MSC Nastran	- Import IGES geometry file into NASTRAN and build mesh
PAM-Generis	- Import NASTRAN mesh and apply full problem description

5.1.1 Geometry

The finite element to be employed for modelling of the prototype geometry is a four noded quadrilateral shell element. Application of the bi-phase model for shell elements in the PAM-CRASH code corresponds to material type 130 which is a multi-layered material tailored for the description of orthotropic laminates. Generation of the finite element mesh begins with the development of a suitable geometry. In this case, the geometry (developed using Rhino3D) is to be exported to MSC.NASTRAN for generation of the finite element mesh which is then

exported to PAM-CRASH. The demonstrator geometry is thus modelled using the midplane of the demonstrator component.

A step-by-step graphical overview of the geometry development (Fig.5.1) shows how the geometry is developed starting with the extrusion of the cylinder sidewall (Fig. 5.1(a)). In terms of a Cartesian coordinate system, the sidewall begins as a circle (diameter = 58mm) centred at the origin which is then extruded to a height (z) of 50mm. The rectangular baseplate is then added (Fig. 5.1(b)) by drawing a rectangular plane with corner points located at (115, 95, 0)mm and (-115,-95,0)mm. To finish off the geometry, a hole is created in the baseplate (Fig. 5.1(c)), the cylinder end is capped (Fig. 5.1(e)) and fillets are introduced where the flat sections meet the cylinder sidewall (Fig. 5.1(d), (f)). The introduction of construction lines (Fig. 5.1(g)) and cutting planes (Fig. 5.1(i)) assists in creating the partitioned quarter geometry of Fig. 5.1(j) that is saved in IGES format for importing into MSC.NASTRAN.

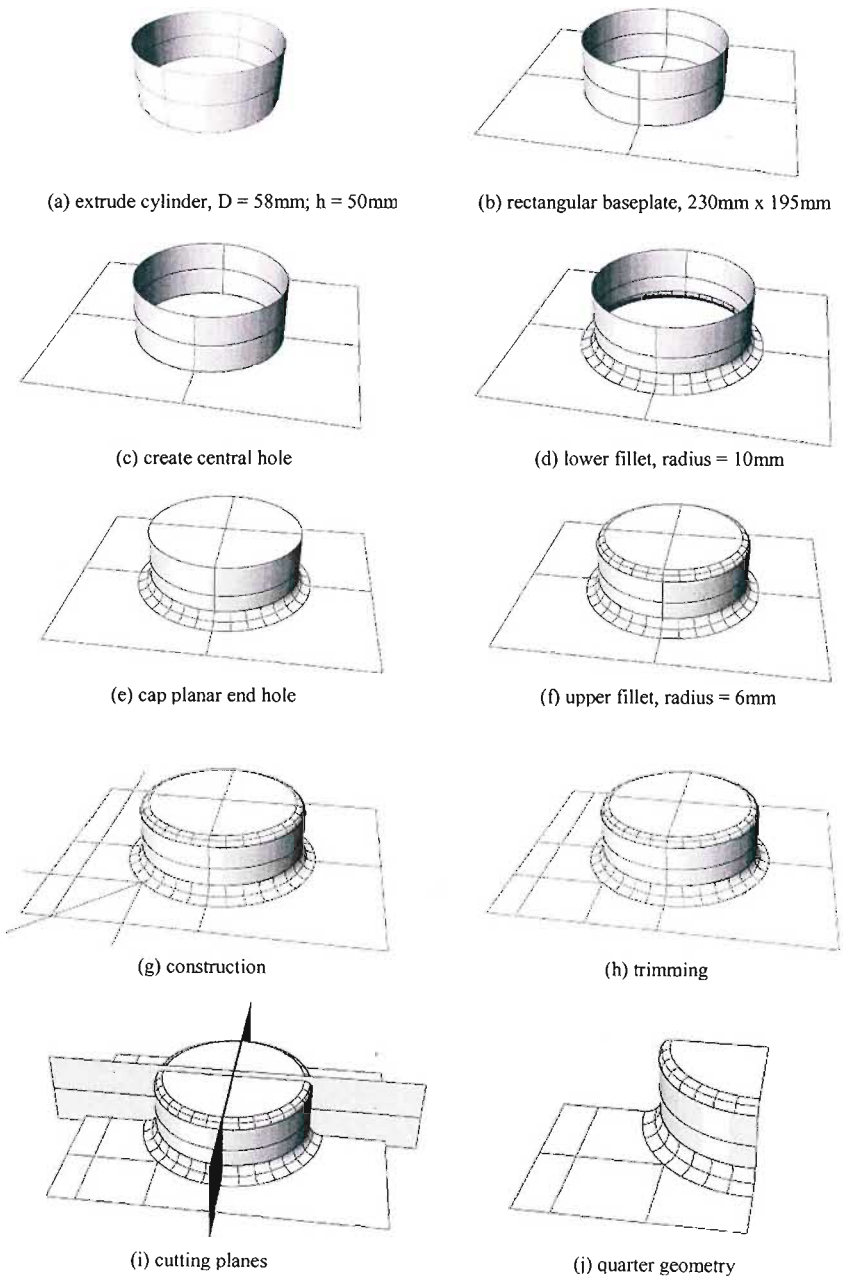

Fig. 5.1 Development of demonstrator geometry, Rhinoceros 3D

5.1.2 Meshing

The geometry developed using Rhino3D was imported into MSC.NASTRAN (Command: File >Import >Geometry) and the procedure followed to generate the finite element mesh (representing the real component) is illustrated in Fig. 5.2. To aid the generation of a structured mesh, a quarter of the geometry is initially meshed and then reflected twice in order to generate a mesh representing the full component. Establishment of a well graded and mapped mesh is also accomplished by segmenting the geometry and setting mesh sizes along the boundary curves (step 1 – Mesh >Mesh Control >Size Along Curve). Once this is done, a mesh is generated for the quarter geometry (step 2 – Mesh >Geometry >Surface) and reflected twice (steps 3 and 4 – Mesh >Reflect >Element) about orthogonal planes, ending with a mesh of elements representing the full prototype. A dummy solution using the NASTRAN solver results in the creation of a DAT file which contains a list of nodes and elements for importing into the PAM-CRASH pre-processor, PAM-Generis. To enable description of separate laminate layups for the demonstrator flats and sidewalls, the flat sections and sidewall are meshed with separate plate property ID's in the NASTRAN environment, creating two separate material regions.

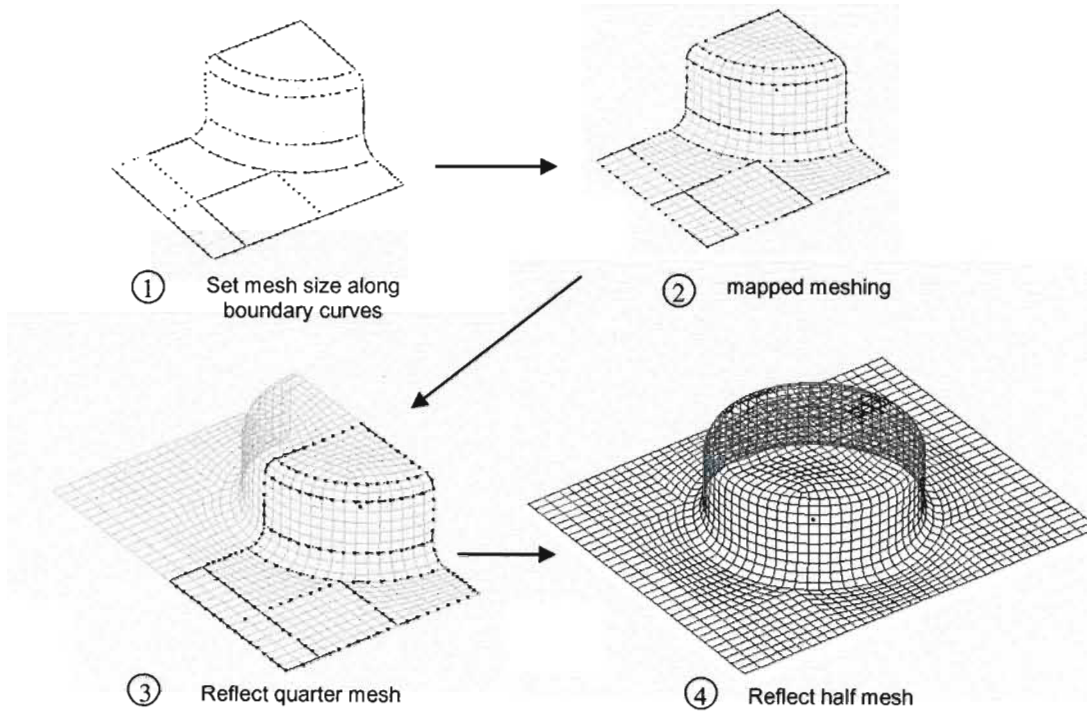

Fig. 5.2 Generating the prototype mesh

5.1.3 Boundary Conditions

In the Generis environment two separate groups of nodes have been defined (Fig. 5.3) which eases the definition of boundary conditions. The node groups are at the base of a definition hierarchy, so that any nodal constraints (or other boundary conditions) defined using the groups are updated when the elements in the group are changed. The nodes are separated into two groups, one for each clamped edge, and the constrained nodes represent the parts of the component that are clamped during physical testing. The fixed end has all nodal degrees of freedom fixed and the row of nodes at the inside edge of the fixed end are defined as a section for reporting the reaction force. In order to further represent experiment, the velocity in the x-direction of the moving edge is set to equal to the velocity of loading for the case concerned.

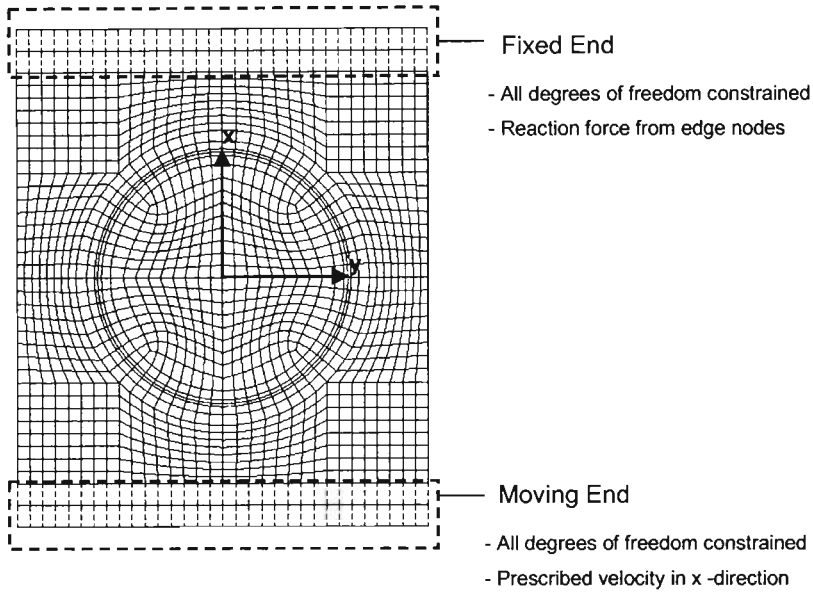

Fig. 5.3 Simulation boundary conditions

5.1.4 Material description (layup)

Testing has been conducted on the glass epoxy composite in the fibre (warp) direction, in order to determine the in-plane tensile and compressive behaviour in that direction. These test results provide response data for a ply loaded in the same direction as the test specimen. Transformation laws (in the form of a transformation matrix) allow for the elemental stresses and strains to be transformed to any orientation, so that the material response can be predicted in all directions. Of particular importance is the orientation of the orthotropic ply's principal directions, defined relative to either a stationary global coordinate system or a local coordinate system attached to the element (Fig. 5.4). Orientations defined in the global coordinate system are projected onto the shell element and transformed into the local element coordinate system.

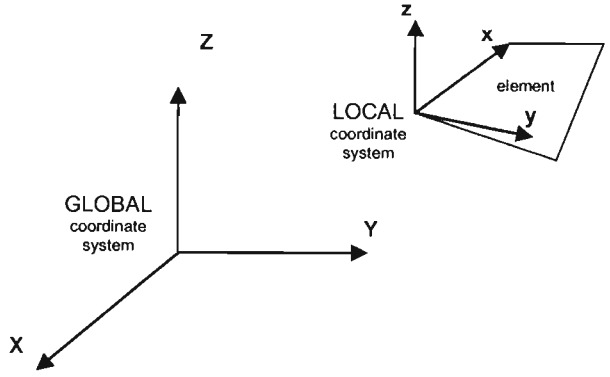

Fig. 5.4 Global and local coordinate systems

The basic tensile and compressive behaviour of the ply material in the natural directions of orthotropy have already been defined during material characterisation and the desired response was confirmed through material calibration (§ 3). For modelling of the demonstrator's response, the description of the material structure implemented in the modelling environment must be representative of the real demonstrator's structure. A mesh was already generated (NASTRAN, § 5.1.2) and nodal boundary conditions applied (PAM-Generis, § 5.1.3) and all that remains is to define the material architecture, so that a simulation can be run.

To this end, it has already been discussed how the fibre orientations on the laminated component are defined separately for separate parts of the component (§ 4.1.3) in terms of separate global coordinate systems. Orientations on the flat sections were defined relative to the global *x*-axis, in the Cartesian coordinate system shown in Fig. 5.5. Orientations on the sidewall were defined relative to the *z*-axis of a cylindrical coordinate system, centered with respect to the cylindrical sidewall. From the designed patterns (and pattern layup sequence) (§ 4.1.2) and in terms of the separate coordinate systems, it was established that the fibre orientations for the three different constructions (LPT1, LPT2, LPT3) may be represented by:

	FLATS (ϕ_1)	SIDEWALL (ϕ_2)
LPT1:	$[0/90]_8$	$[0/90\ \pm45]_{2S}$
LPT2:	$[0/90\ \pm45]_{2S}$	$[0/90]_8$
LPT3:	$[0/90]_8$	$[\pm45]_8$

This fibre coding (eg: $[0/90]_8$ / $[0/90\ \pm45]_{2S}$) shows the orientations contained in each woven layer of fabric reinforcement. A shorter way of defining the fibre orientation (which is more applicable for model definition) is only to list the orientation of the warp fibres. The other fibre direction (weft) is automatically known since the fabric is orthogonally woven. Using this shortened notation, the ply orientations are:

	FLATS (ϕ_1)	SIDEWALL (ϕ_2)
LPT1:	$[0]_8$	$[0\ 45]_{2S}$
LPT2:	$[0\ 45]_{2S}$	$[0]_8$
LPT3:	$[0]_8$	$[45]_8$

Description of material layup has been completed for laminated prototype LPT1, which consists of 8 layers on the flat sections of the part, aligned with the global x-axis, and 8 layers on the sidewall, alternately aligned at orientations of 0° and 45° with respect to the projection of the global z-axis onto the cylindrical sidewall. Identically to the tensile and compressive specimens, the real laminated components have an average thickness of 2.4mm, made up from 8 layers of woven laminae, each with average thickness of 0.3mm. As pointed out, the flat sections of the real prototype consist of 8 layers that are aligned with the global x-axis. For modelling purposes, a simplified representation, employing 4 layers each of thickness 0.6mm (also aligned with the global x-axis), is used to represent the flat sections of the prototype. The construction of the sidewall cannot be simplified in this way and the sidewall is thus modelled using eight layers each with thickness of 0.3mm. As for the real laminated component, the modelled plies of the cylinder sidewall are alternately stacked at 0° and 45°, relative to the local element coordinate systems of the sidewall elements. Description of the sidewall ply orientations in terms of the local element coordinate system is made possible by the structure of the sidewall mesh, which is aligned with the global z-axis. Confirmation of the local coordinate orientations for the sidewall elements is provided by viewing the local element directions in the NASTRAN environment (Fig. 5.5). A comparison of the real component's construction and the construction of the modelled prototype is provided in Fig. 5.6.

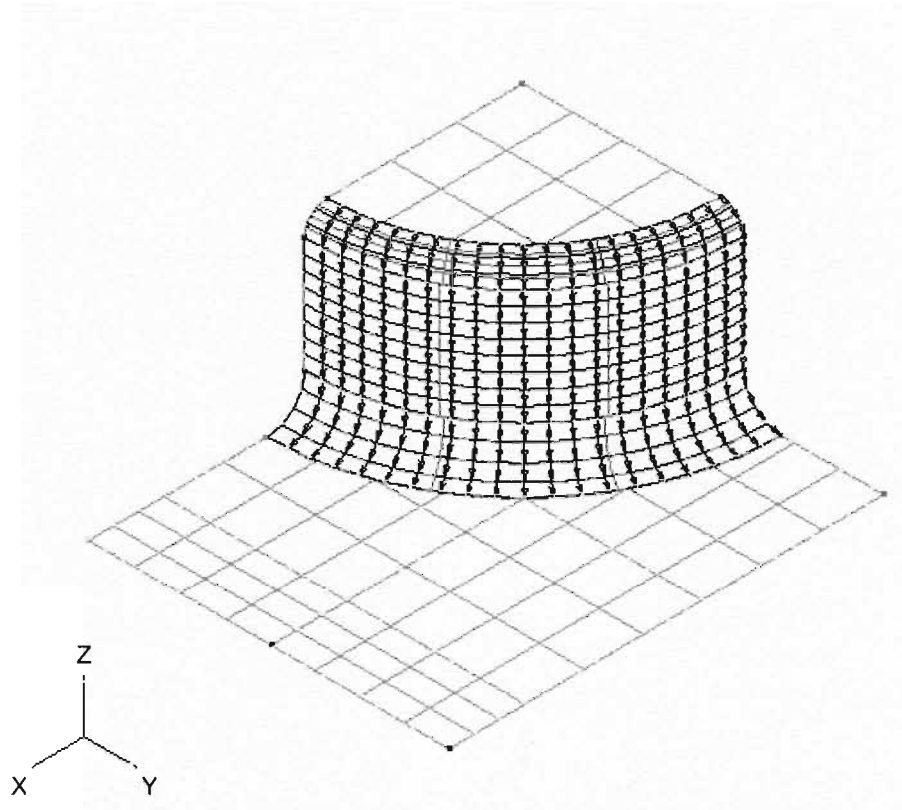

Fig. 5.5 Confirmation of local element directions for the modelled prototype sidewall

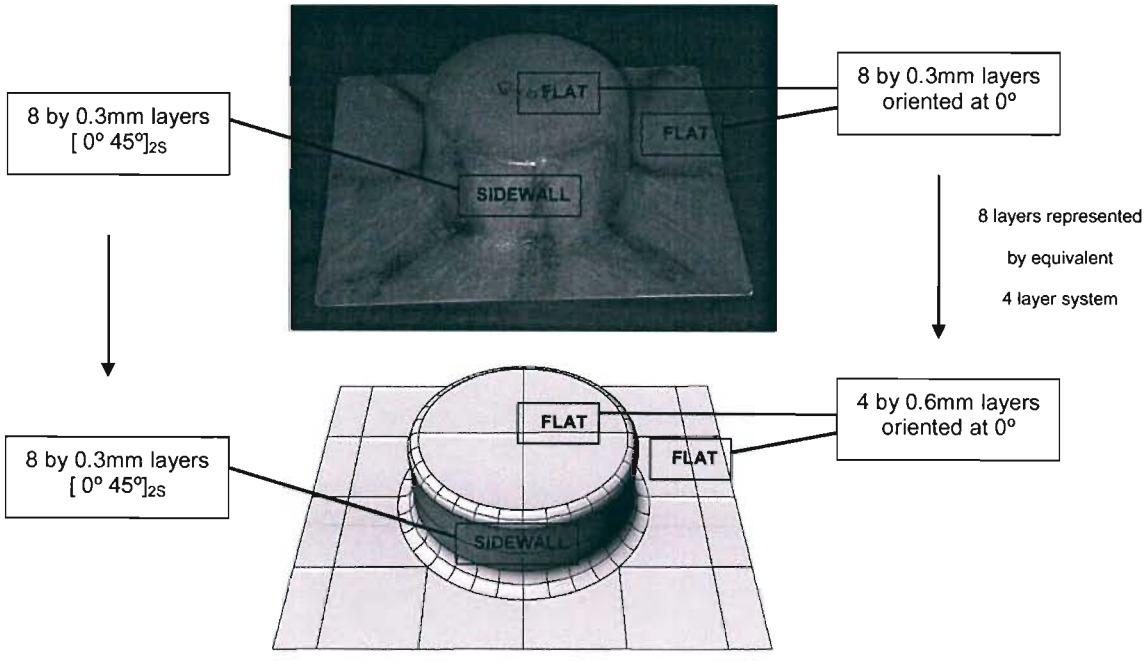

Fig. 5.6 Comparison of real and modelled stacking sequence

5.2 Numerical simulation

5.2.1 Simulation of the laminated demonstrator

During the material characterisation and calibration process, parametric adjustments resulted in three tensile material characterisations that displayed increasing agreement with the experimentally recorded tensile curve. These were material 130A, 130B and 130C (see § 3.3) and all of these materials relied on the same compressive characterisation (that was derived and calibrated based on available compressive data). The calculated material characterisation parameters are repeated here in Tables 5.1 and 5.2.

Table 5.1 Material 130A tensile characterisation parameters

Material Constants						**Damage Parameters**			
tensile moduli (GPa)		shear moduli (GPa)		Poisson's ratios		critical strains		damage values	
E_1	17	G_{12}	5.5	ν_{12}	0.17	ε_{iv}	0.0053	-	-
E_2	17	G_{23}	3.4	ν_{23}	0.30	ε_{1v}	0.0100	d_1	0.12
E_3	13	G_{13}	3.4	ν_{13}	0.30	ε_{uv}	0.0106	d_u	0.95

Table 5.2 Material 130A, 130B and 130C compressive characterisation parameters

Material Constants						**Damage Parameters**			
tensile moduli (GPa)		Shear moduli (GPa)		Poisson's ratios		critical strains		damage values	
E_1	4.37	G_{12}	5.5	ν_{12}	0.17	ε_{is}	0.0451	-	-
E_2	4.37	G_{23}	3.4	ν_{23}	0.30	ε_{1s}	0.0537	d_1	0.07
E_3	3	G_{13}	3.4	ν_{13}	0.30	ε_{us}	0.0902	d_u	0.74

Simulation of the response of laminated prototype LPT1 (described in § 4.1.4) to a loading with constant velocity of 150mm/s has been undertaken. This represents the intermediate loading velocity employed during testing of the laminated demonstrator and is equivalent to experiment LPT1 case 2 (components were tested at load speeds of 2.4mm/s, 150mm/s and 344mm/s, § 4.3).

The essential components for implementation of this model have been outlined and are reviewed as follows:

1) Material characterisation – Specimens were manufactured and tested in order to characterise an individual layer of the woven fabric glass epoxy laminate that is used in the construction of the laminated prototype component. These were subsequently tested and material characterisation parameters were extracted from the experimental curves.

2) Material calibration – During the material calibration process, the specimen tests are simulated in order to verify that the enlisted material characterisation parameters do indeed represent the experimentally recorded response.

3) Meshing – Due to the complexity of the geometry and material structure, the geometry is divided into segments so that parts of the component may be meshed separately. This allows for definition of different material layups over separate parts of the geometry and aids in the development of a structured mesh.

4) Boundary conditions – Boundary conditions are applied, which describe the support conditions and the applied loading. For the prototype under investigation, the groups of nodes representing the clamped parts of the component were constrained (in all degrees of freedom) and the moving end was prescribed to translate with a constant velocity of 150mm/s (as for experiment LPT1 case 2).

5) Material layup – Here the construction of the real laminated component must be represented and described in the modelling environment. This involves description of ply orientations with respect to either a global or local (element) coordinate system. Each ply has properties as determined during the characterisation and calibration phase and is assigned a density ($1635kg/m^3$) and thickness.

For simulation of experiment LPT1 case 2, it was found that the three alternative material characterisations (130A, 130B, 130C) produced results with little variation. A comparison of the simulated results obtained using material 130B (PT130B) has been made with the results obtained from testing prototype LPT1, at a loading velocity of 150mm/s (Fig. 5.7). The figure provides a direct comparison of the force-displacement history recorded during the experiment and the force-displacement output from the simulation, in the form of a graph. A comparison is also made between deformation states recorded during the experiment (using a digital camera) and the deformation states, at the corresponding point in time, obtained from the simulation.

The simulated deformation states show good resemblance to the real deformations. In the first instance, close to the point of peak load (at displacement $s_1 = 4mm$), the anti-symmetric state of deformation that is observed from experiment is repeated in the simulations (Fig. 5.7). As the displacement continues further, the typical deformation of the real component is seen in the simulated output ($s_2 = 11mm$, $s_3 = 22mm$). A comparison of the failure patterns for the simulated and real component show the areas of damage reported from the simulation that correspond to cracking in the real component (Fig. 5.8). Turning attention to the force-displacement plots, it is seen that the simulated response follows the experimentally recorded curve, up to a displacement of around 2mm. The peak load recorded during experiment occurs at a displacement of 4.5mm and has a recorded value of 7.7kN. This is compared to a predicted peak of 6.5kN, after a displacement of 3.9mm. The predicted peak load undershoots the recorded value by 15.6% and the predicted displacement (at peak) undershoots the recorded displacement (at peak) by 13.3%. After the peak is passed, the predicted load sustained by the component is lower than the load sustained by the component during experiment.

During experiment, a transition from one buckling mode to another was observed at the demonstrator baseplate's free edge (§ 4.3). Component LPT1 was seen to 'snap' from its original shape to take on an anti-symmetric state of deformation. With reference to Fig. 5.9(a), it is seen how the plate edge takes on a transitional deformation mode ($s_1 = 1.9$ mm) as the structure snaps through to the anti-symmetric mode ($s_2 = 3.8$ mm) that prevails until major crack growth results in folding of the structure. The same behaviour is observed during simulation, where the transitional deformation mode prevails up to 3mm of displacement during the simulation (Fig. 5.9(b)). The simulation predicts the change from the original deformation mode to the anti-symmetric deformation mode at a slightly higher displacement ($s_1 = 3.0$ mm).

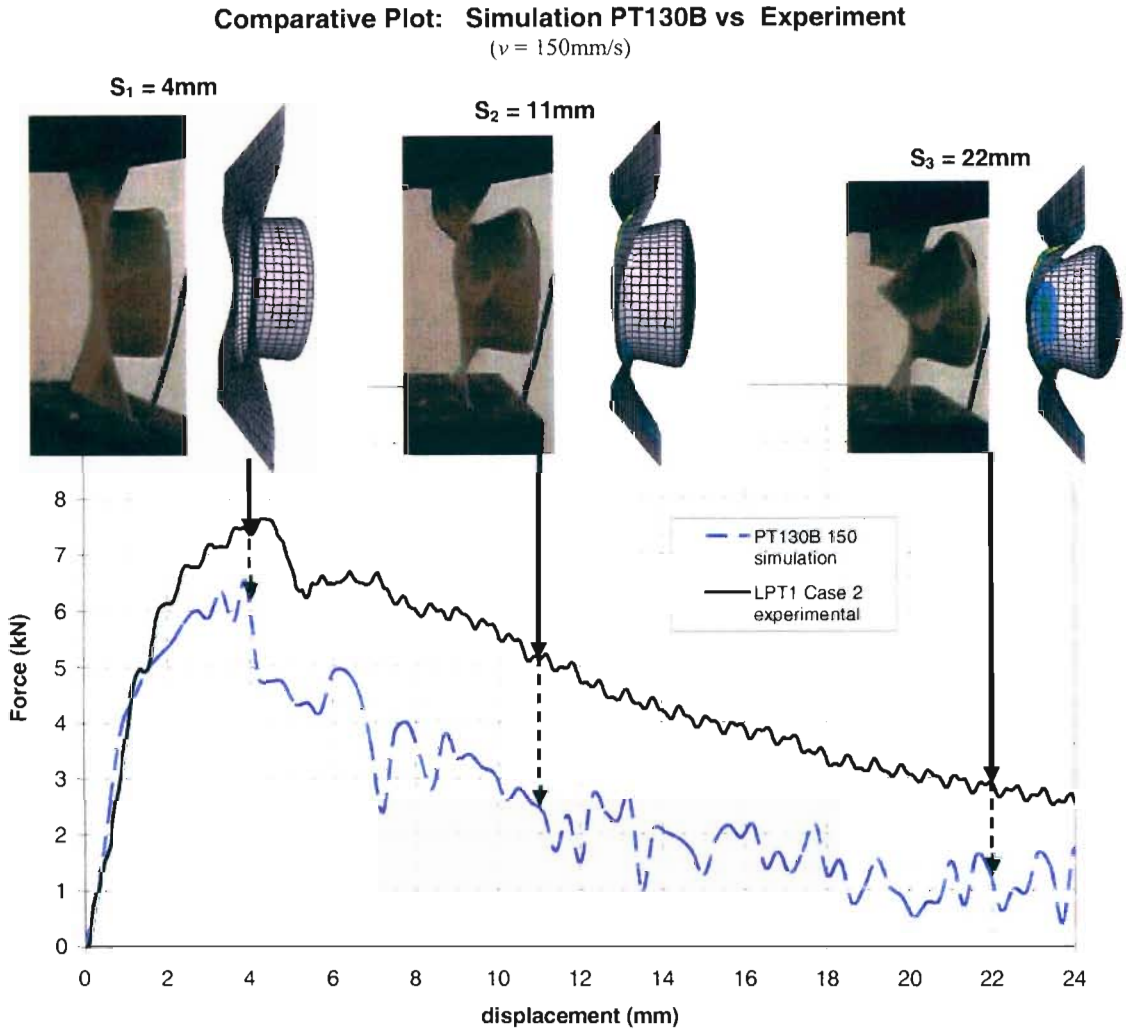

Fig. 5.7 Comparison of simulated and experimental response for LPT1, v = 150mm/s

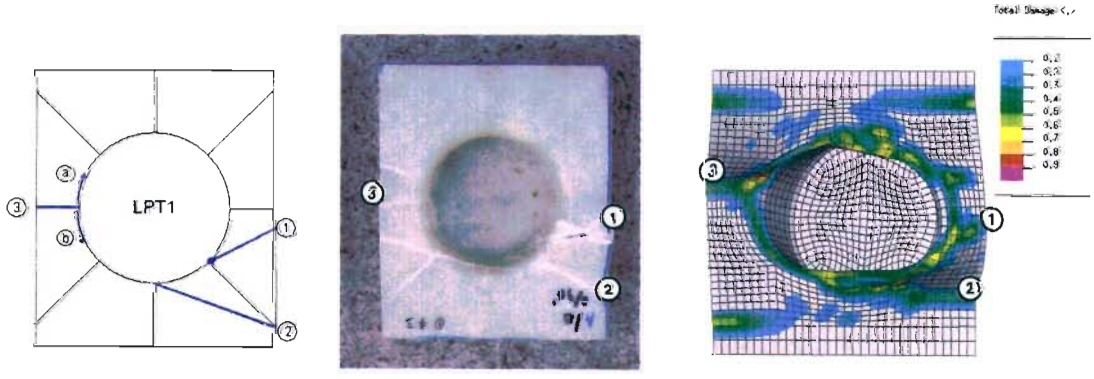

(a) schematic failure pattern (b) real failure pattern (c) simulated damage pattern

Fig. 5.8 Comparison of LPT1 failure patterns (schematic, real and simulated)

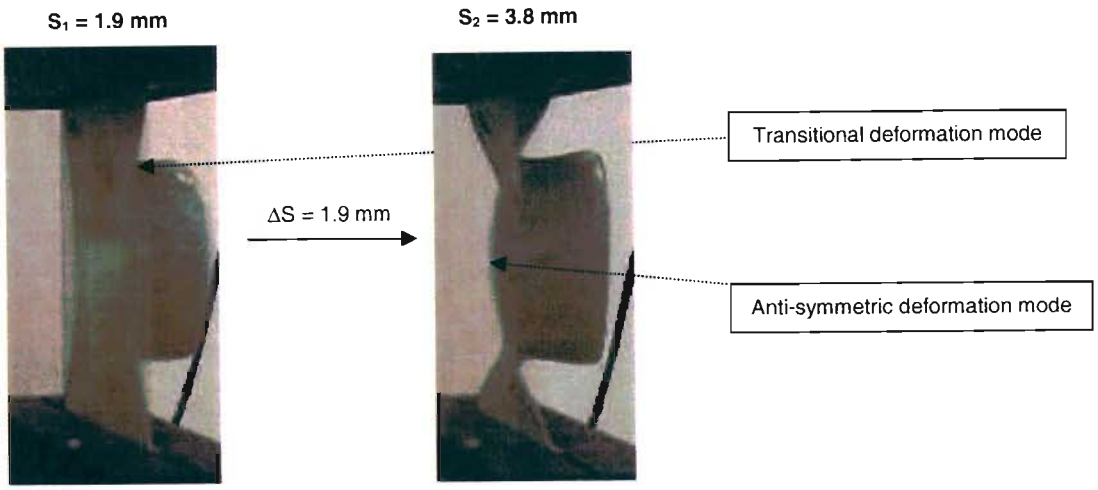

(a) real deformation mode transition at 1.9 mm displacement, LPT1 v = 150mm/s

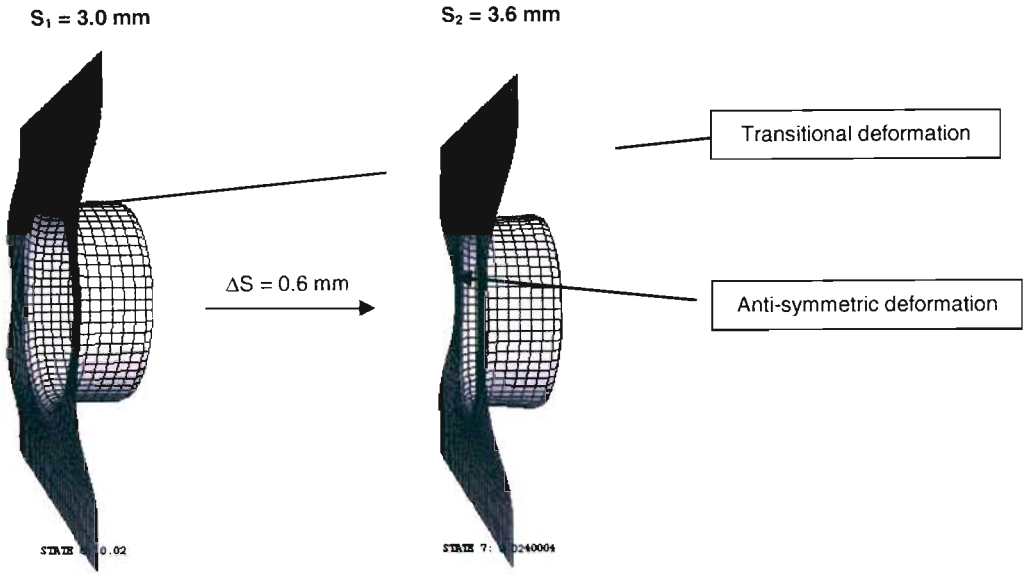

(b) simulated deformation mode transition at 3 mm displacement, LPT1 v = 150mm/s

Fig. 5.9 Capturing of transitional deformation mode from experimentation and simulation

Comparison of the output obtained through simulation of demonstrator LPT1, crushed at a constant rate of 150mm/s, with experimental data includes comparison of the force-displacement history recorded at the clamped edge and the deformation states recorded over time. The force-displacement history and deformation states have been accurately reproduced in the simulation before major cracking and folding of the component occurs. The load that is sustained during the destruction of the demonstrator (after the peak load is passed) is less accurately reproduced during simulation and further model refinements can be aimed at improving the accuracy of the predictions over the full crush event. Overall, the deformation states predicted during simulation compare favourably with the deformation states recorded during experiment and the simulated results reproduce, within an accuracy of 16%, the peak load recorded during experiment and the displacement at peak load has been reproduced with an accuracy of 13%.

5.2.2 Demonstrator reinforced with random oriented short fibres

Performance of the instituted modelling methodology for the demonstrator component constructed using fabric reinforcement has already been investigated (§ 5.2.1). The results demonstrate the capability of the instituted model (and modelling method) to predict the nature of the demonstrator's deformation, as well as the peak load and displacement at peak, which were predicted within an accuracy of 16%. In order to investigate the performance of the instituted modelling methodology for the same demonstrator, constructed using a different material (that requires an alternative material model), the simulation of the demonstrator reinforced with randomly oriented short fibres has been undertaken. Material characterisation and the comparison of simulation results with experimental data are made possible using the results presented by Morozov (2003). In a similar fashion as for the work undertaken by Morozov, simulation of the short fibre reinforced demonstrator's response has been completed using PAM-CRASH isotropic shell elements that employ either an elastic-plastic or elastic-plastic damaging material definition.

The polyester based SMC material with fibre glass reinforcement of average length 25mm and volume fraction of 20% (obtained from *ABB, South Africa*) was tested in tension in order to produce an experimental characterisation of the material behaviour in tension. Subsequent description of this response has been undertaken using available PAM-CRASH isotropic shell elements. The material behaviour is described using PAM-CRASH Material Type 105 which is an elastic-plastic material that includes damage. Three alternative descriptions have been used and these are:

105A – Elastic-plastic + damage
105B – Elastic-plastic + damage, lower ultimate damage than material 105A
105C – Elastic-plastic material with zero damage

The modelled stress-strain behaviour is based upon the SMC material's average response, as represented by one of the specimens tested. Since the specimen with most average response displayed a failure strength 13% lower than the mean material strength, extrapolation of the average response up to the mean failure strength of 60MPa was necessary. The resulting material descriptions are shown graphically in Fig. 5.10, and the extracted characterisation parameters (that have been entered into the PAM-CRASH user interface) are indicated in Tables 5.3. A comparison of the simulated stress-strain response (obtained from the various material models) with the experimentally recorded stress-strain diagram is made (Fig. 5.11). This serves to validate the material characterisation employed in the modelling environment.

Table 5.3 Implemented Material Types 105

		105A	105B	105C
ELASTIC	E_0 (GPa)	11	11	11
	ν	0.3	0.3	0.3
	σ_y (MPa)	30	30	30
PLASTIC	E_i, σ_i (GPa, MPa)	(6, 42)	(6, 42)	(6, 42)
		(4, 60)	(4, 60)	(4, 60)
DAMAGE	ε_i	0.0092	0.0092	0.0092
	ε_f	0.011	0.011	0.0092
	ε_u	0.012	0.0128	0.0092
	d_1	0.35	0.35	0
	d_2	0.85	0.67	0

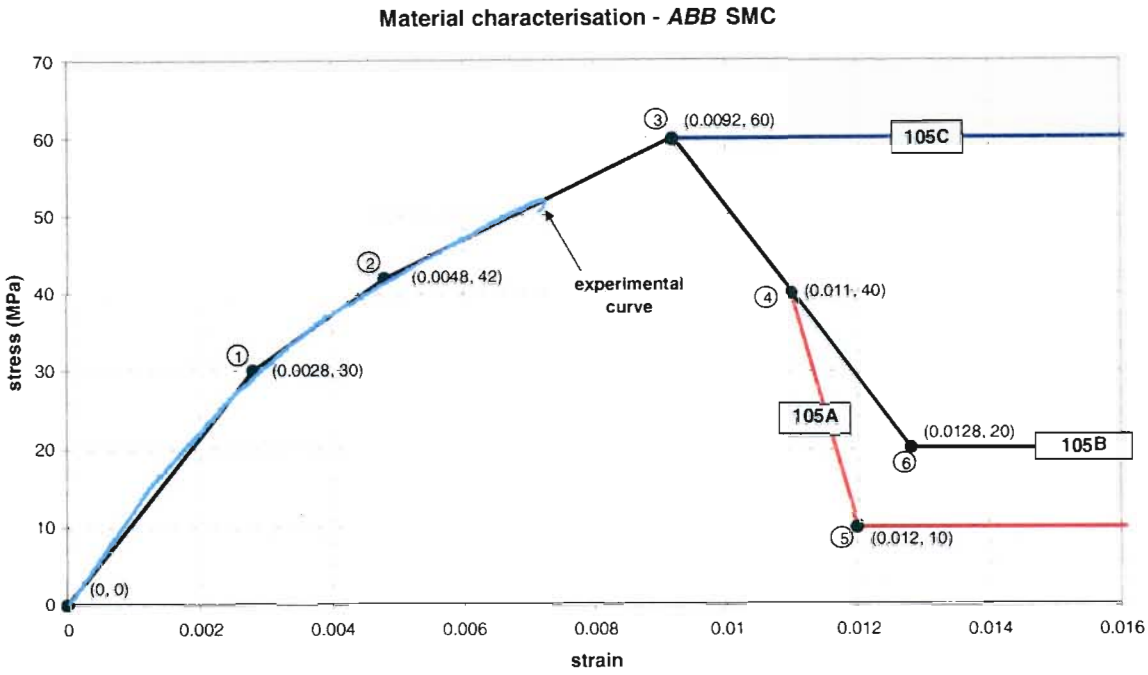

Fig. 5.10 Material characterisation curves, SMC material

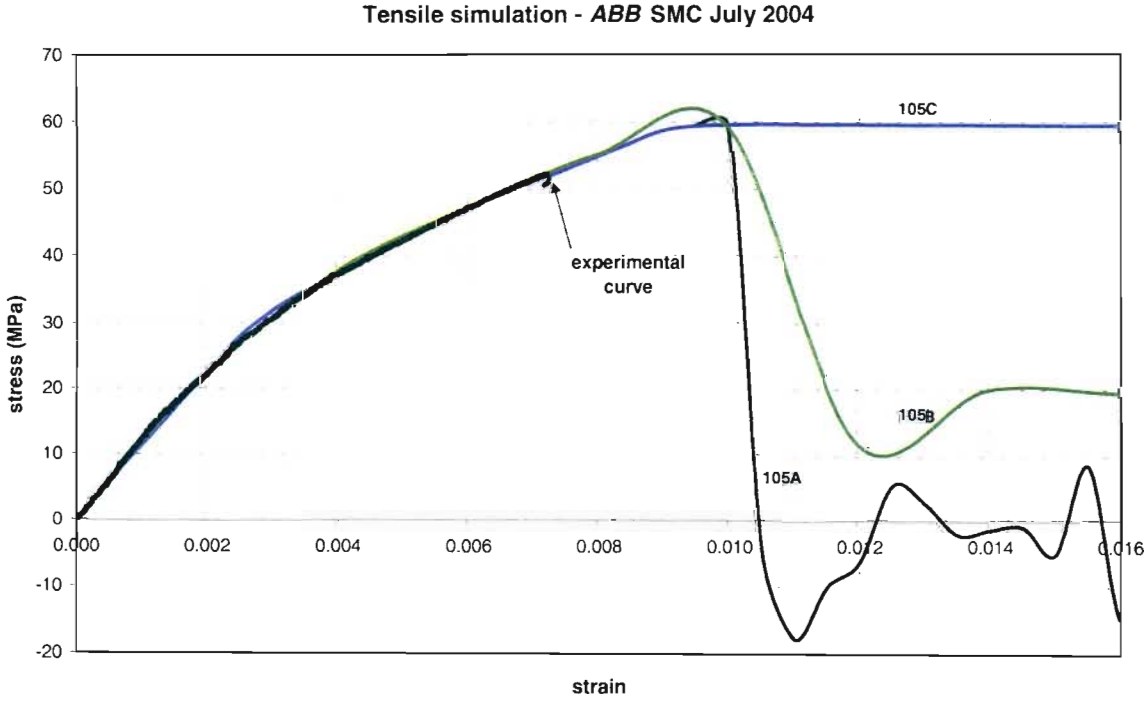

Fig. 5.11 Laminate simulated tensile response obtained through various characterisations

The structure of the finite element model employed for simulation of the SMC demonstrator's response to crushing is the same as already detailed for laminated demonstrator (§ 5.1). The only difference is in the material model employed. The results obtained from the respective prototype simulation runs PT105A, PT105B and PT105C are provided in Figs 5.12 – 5.15. The presented results provide a comparison of the real and simulated force-displacement history and provide simulated deformation states at critical points during the crushing of the component. The points on the simulated curve (at which the deformation states apply) are indicated by leader lines and a contour legend (to the right of the figure) shows the limit values used to obtain the stress and damage contour plots (which are superimposed on the deformation states). The damage values are unitless, ranging from zero to unity, and the reported maximum equivalent stress over the shell thickness has units of MPa.

Comparison of the output obtained from a simulation employing material 105C with the experimental force-displacement history for one of the SMC prototypes tested at 2mm/s is shown in Fig. 5.12. For the simulation, the moving edge of the prototype is forced to also travel at 2mm/s, in the same direction as for the experiment, and the other edge of the prototype is fixed. The results show good agreement between the simulated and experimentally recorded initial behaviour, where the peak load (about 15kN) and displacement at peak load (1.2mm) are nearly equal for the simulated and real case. This model does, however, over predict the load which is sustained by the component for displacements greater than 4mm.

Following (Fig. 5.14) is a comparison of the output obtained from a simulation employing material 105A with the experimental force displacement history for an SMC prototype tested at 100mm/s. As for the previous case, velocity of the moving edge for the simulation is set equal to the real loading velocity, recorded from experiment (v = 100mm/s) and the opposite edge is fixed. An increase in the peak load supported by the real component at the different loading velocities is observed from the experimental data (the peak load increases from 15kN to 16kN, when comparing the experimental curves for the 2mm/s and 100mm/s cases). An increase in peak load is also registered by the simulation, which increases from 15kN (at 2mm/s) to 18kN (at 100mm/s). The displacement at peak is accurately reproduced (1.8mm) but the simulated curve undershoots the experimentally recorded curve up to a displacement of 5mm. Good agreement is seen for the remaining displacement.

Finally a comparison of the output obtained from a simulation employing material 105B with the experimental results for the 100mm/s case is provided in Fig. 5.15. It is expected that the simulated initial response obtained from this model will follow the simulated response obtained from the model employing material 105A, since the materials have identical definitions up to a strain of 0.01 (see Figs 5.10 and 5.11). This is clear from the comparative plot (Fig. 5.15), where the two simulated response curves are equal up to the peak load. The difference in the two model outputs manifests itself in the crushing load sustained by the component. Material 105B is expected to sustain higher load, since the material definition calls for material 105B to have a higher load carrying capability for strains higher than 0.01, due to a reduced ultimate damage value (see Table 5.3). The sustained crushing load reported from this simulation is indeed higher than that reported from simulation PT105A, resulting in good agreement between simulation PT105B and the experimental curve up to a displacement of 5mm. Thereafter the simulated sustained load overshoots the experimental curve, gradually reducing to a value of just over 4kN, equal to the final load after 10mm of displacement reported from simulation PT105A.

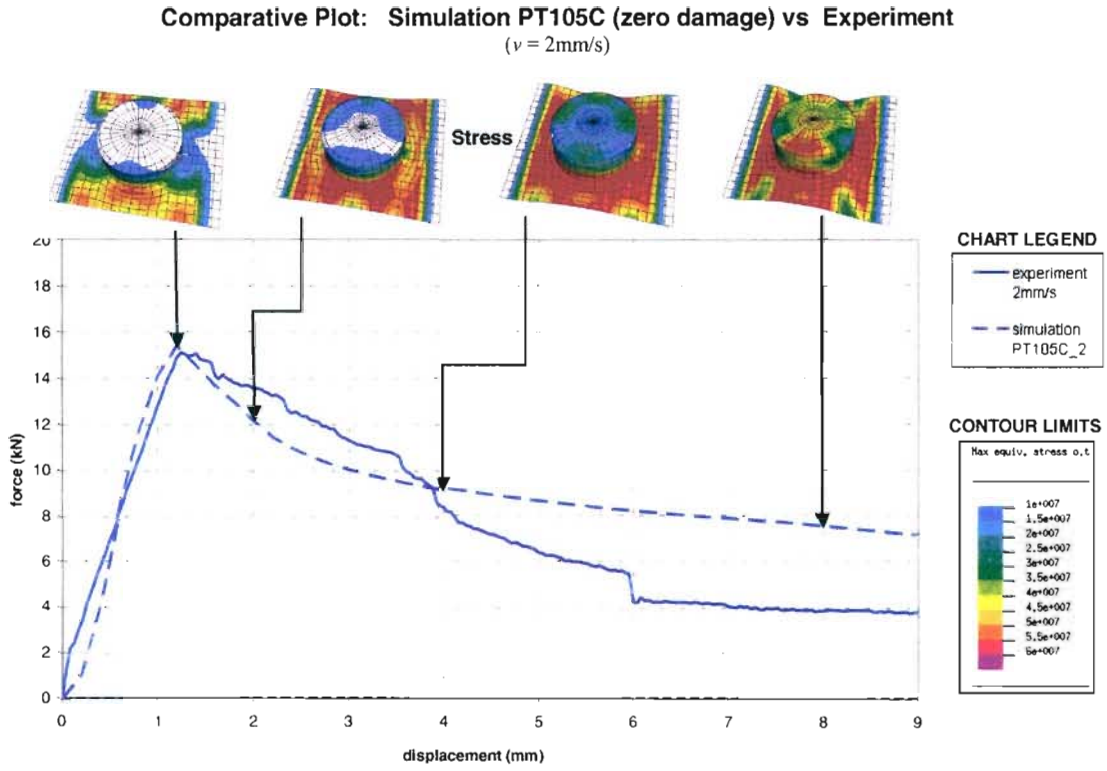

Fig. 5.12 Simulation output vs experiment, materials 103A & 105C, v = 2mm/s

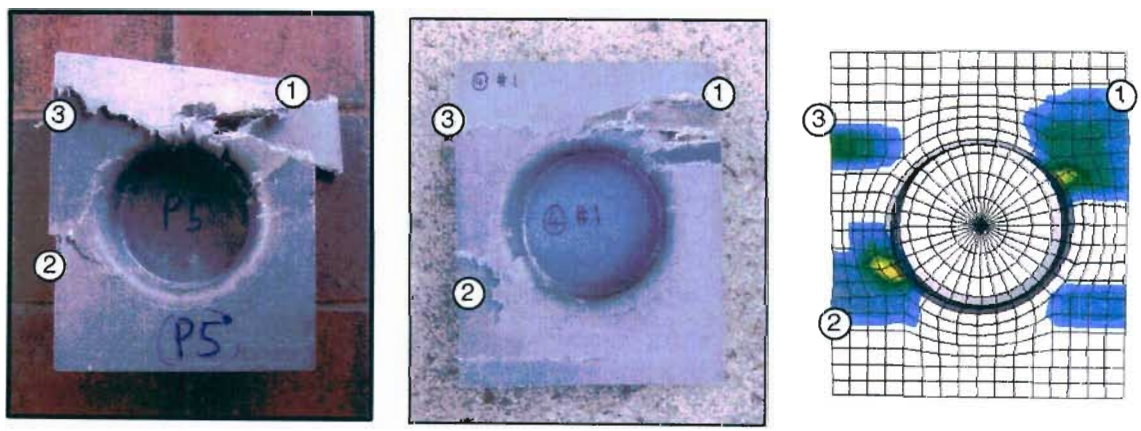

(a) real failure pattern (v = 100mm/s)

(b) real failure pattern (v =330mm/s)

(c) simulated damage pattern (v = 100mm/s)

Fig. 5.13 Comparison of the SMC prototype failure patterns (real and simulated PT105A)

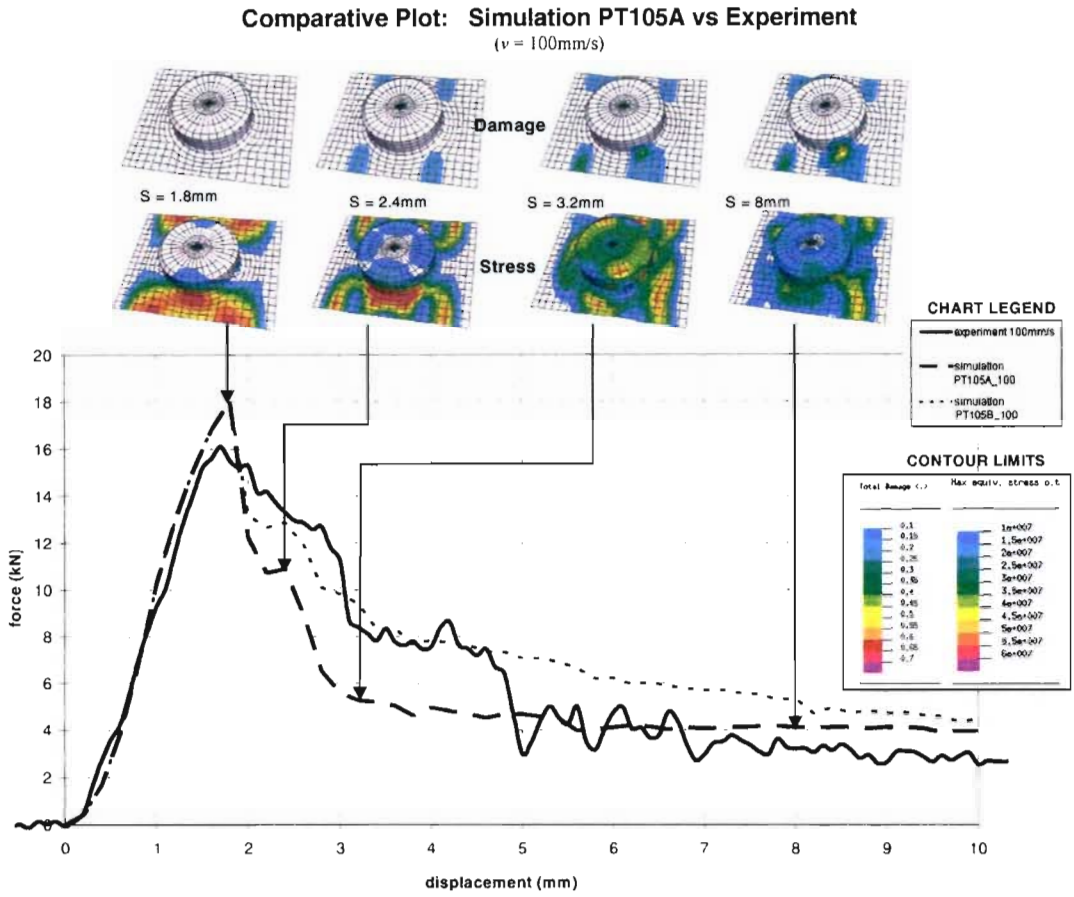

Fig. 5.14 Simulation output vs experiment, material 105A, v = 100mm/s

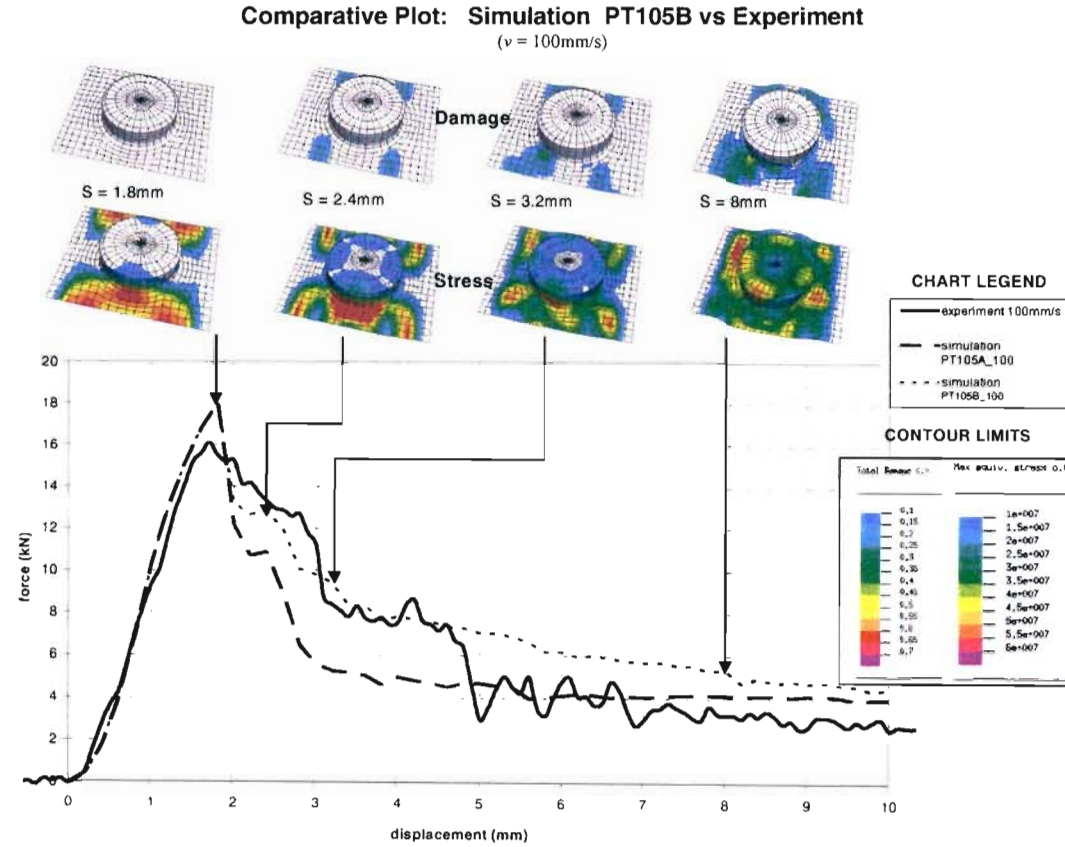

Fig. 5.15 Simulation output vs experiment, material 105B, v = 100mm/s

Important observations which are made, through comparing the deformation plots with the force-displacement curves, are as follows:

1) For all of the simulations, when the peak load is reached the maximum equivalent stress in those parts of the structure that are close to failure (indicated by the onset of damage) reaches the pre-defined material strength of 60MPa (see contour plots).

2) For simulation PT105C (with zero damage, Fig. 5.12) a similar peak occurs (even though no damage is defined) and as the displacement increases further, a greater portion of the baseplate reaches a state of maximum stress. This follows from the original material definition for material 105C which is able to sustain the ultimate stress of 60MPa for large values of strain. As a consequence, the deformation plot remains smooth (with no folding) as does the simulated curve (the curve is piecewise smooth)

3) The deformation plots most agreeable with the experiment are obtained from simulation employing material 105A. Folding occurs in the same locations as has been observed during experiment and a comparison of the real and simulated failure patterns (Fig. 5.14) shows good agreement.

4) For those models that incorporate damage to reduce the material load carrying ability (PT105A and PT105B), damage is an indicator of material failure. A careful examination of the stress and damage contours (Figs 5.14 and 5.15) shows how a state of maximum stress is reached at the same time that the peak load is reached (s = 1.8mm). Once the peak load is passed (which indicates initial failure of the prototype component) parts of the structure that display damage are relaxed (s = 2.4mm). This is shown by a reduced stress in those parts of the structure where damage prevails (through comparison of the damage and stress contours at the same displacement). Further relaxation and stress redistribution occur as the structure is further crushed and folded, under a significantly reduced load.

5.3 Conclusions

The bi-phase material model applied to a four noded quadrilateral Mindlin-Reissner type shell element (possessing six degrees of freedom) has been successfully used to model the laminated demonstrator component LPT1's response to a constant velocity crushing load, with the aid of the PAM-CRASH analysis tool. Implementation of the model required material characterisation, material calibration and finite element model development. The concurrent development of a physical laminated demonstrator component (with three alternative material architectures), together with a repeatable testing program, resulted in the generation of experimental data necessary for grading the performance of the instituted FE model(s).

A comparison of the predicted response for the virtual prototype LPT1 and the real demonstrator component, tested at a loading rate of 150 mm/s, shows how the modelled force-displacement response agrees well with the experimentally recorded response, for the initial displacements up to around 2mm. Once significant damage occurs, some discrepancy between LPT1's simulated load carrying and recorded load carrying exists, with the predicted sustained load lower than the experimentally recorded load sustained by the demonstrator during progressive crushing. Despite the reduced accuracy in the level of load sustained by the damaged component as crushing progresses, the existence of a transitional deformation mode has been observed during experiment and is also predicted by the instituted model.

Furthermore, the predicted deformed shape and failure patterns show good resemblance to the experimentally observed deformed shape and failure patterns. It is thus concluded, in general, that the above method of application of the PAM-CRASH analysis tool is capable of predicting effectively the crush response of thin-walled laminated structures like the demonstrator component.

Model refinements that can be aimed at improving the accuracy of the predictions over the full crush event include use of another element type, refinement of the FE mesh or use of an alternative material/damage model. It should also be noted that experimental imperfections as well as inherent uncertainty in the experimental results also influence the correlation between the experimental and theoretical data. Future developments could also include the consideration of failure initiators and selectively reinforced structural segments during the construction of the FE model. Shear and through thickness stiffness were inferred from theory and literature, suggesting that further experimental work to characterise the material shear response is another avenue to explore that could result in improved accuracy in the material characterisation which would influence the demonstrator simulation results.

Further research to determine suitability of alternative element types for application to the problem of modelling thin-walled shell structures response to crushing loads would help to identify other finite elements for simulation of the demonstrator's crash response. Refinement of the FE mesh in the region of sharp hinge folding lines could improve the accuracy of the simulated folding and failure pattern. Finally, use of alternative material models, such as the global ply model (Ladeveze and Le Dantec, 1992) and/or the global ply model modified for the description of fabric plies (Johnson et al., 2001) could provide improved correlation between the experimental and theoretical results for the crushing of the laminated demonstrator. Augmentation of an alternative failure/damage model with the existing bi-phase model might also be investigated as an option to improve the correlation between results.

CHAPTER 6

MODELLING UNDER IMPACT CONDITIONS

Simulation of the laminated demonstrator's response to a case of impact loading has been undertaken in order to demonstrate the capability of the model to simulate the crash response of laminated structures. For the crash simulation an added mass of 1000kg is applied and distributed over the nodes that make up the moving end of the demonstrator. The nodes with added mass are then assigned an initial velocity and the two cases investigated are for an initial velocity of 1m/s and an initial velocity of 5m/s, respectively.

6.1 Laminated demonstrator crash model

For implementation of the demonstrator crash models, alternative boundary conditions are applied to the FE model previously developed for simulation of the laminated demonstrator's response to a constant velocity crushing load (§ 5.1). As shown in Fig. 6.1, one end of the component is fixed and has all nodal degrees of freedom constrained and the row of nodes at the inside edge of the fixed end are defined as a section for reporting the reaction force. The moving end is allowed to translate in the x-direction and has all other degrees of freedom fixed. Loading applied to the moving end consists of an added mass of 1000kg, distributed over the constrained nodes, and an initial velocity of either $1ms^{-1}$ or $5ms^{-1}$, depending on the case being investigated, is applied to the same nodes.

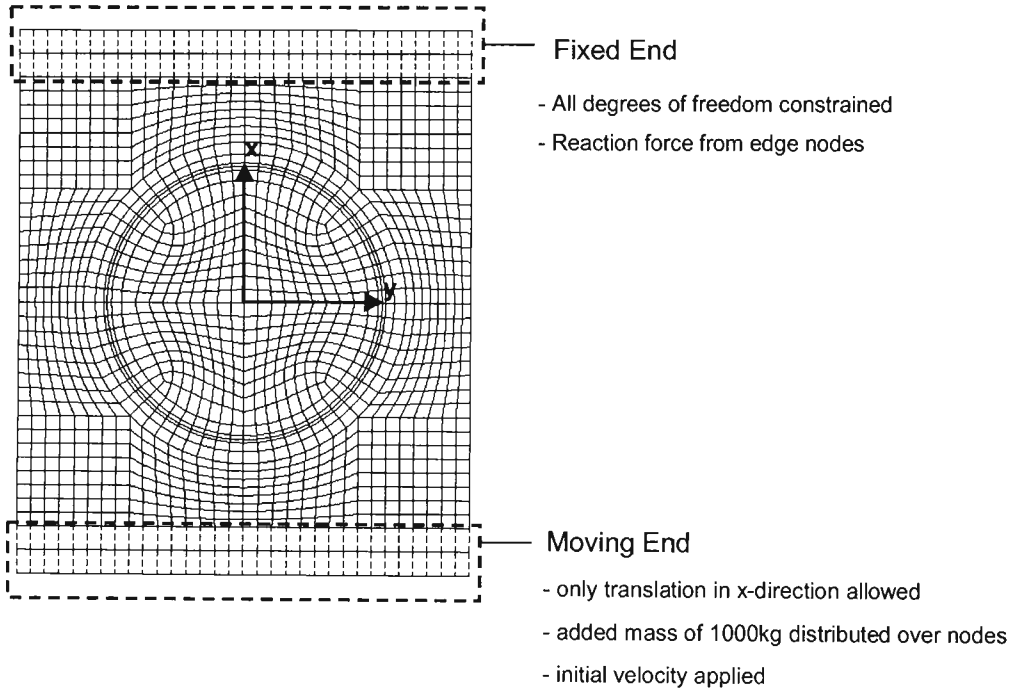

Fig. 6.1 Crash simulation boundary conditions

The results obtained from the crash simulation in the form of a force-displacement plot (Fig. 6.2) show how an increase in the initial velocity results in an increase in the peak load reached, as well as more noticeable oscillations in the force displacement response. New deformation modes are predicted for the crash simulation of the laminated demonstrator LPT1 (Fig. 6.2) when compared to the simulated deformation obtained for lower velocity loading (Fig. 6.3), accounting for the significantly varied load-displacement behaviour. In particular the transitional deformation mode identified during lower velocity loading (Fig. 5.9) which prevailed only for small displacements (up to 1.9mm during experiment and up to 3.0mm during simulation) is predicted during crash modelling to be prevalent right up to failure for the 1m/s crash simulation of LPT1. For the crash simulation at 1m/s, complete folding of the base plate occurs which accounts for the abrupt drop in load carrying capability between 8 and 10mm of displacement. For the 5m/s crash, a high peak load is predicted (just over 14 kN) and folding at the sides of the cylindrical shell, as well as large oscillations in the load transmitted to the fixed support, are predicted.

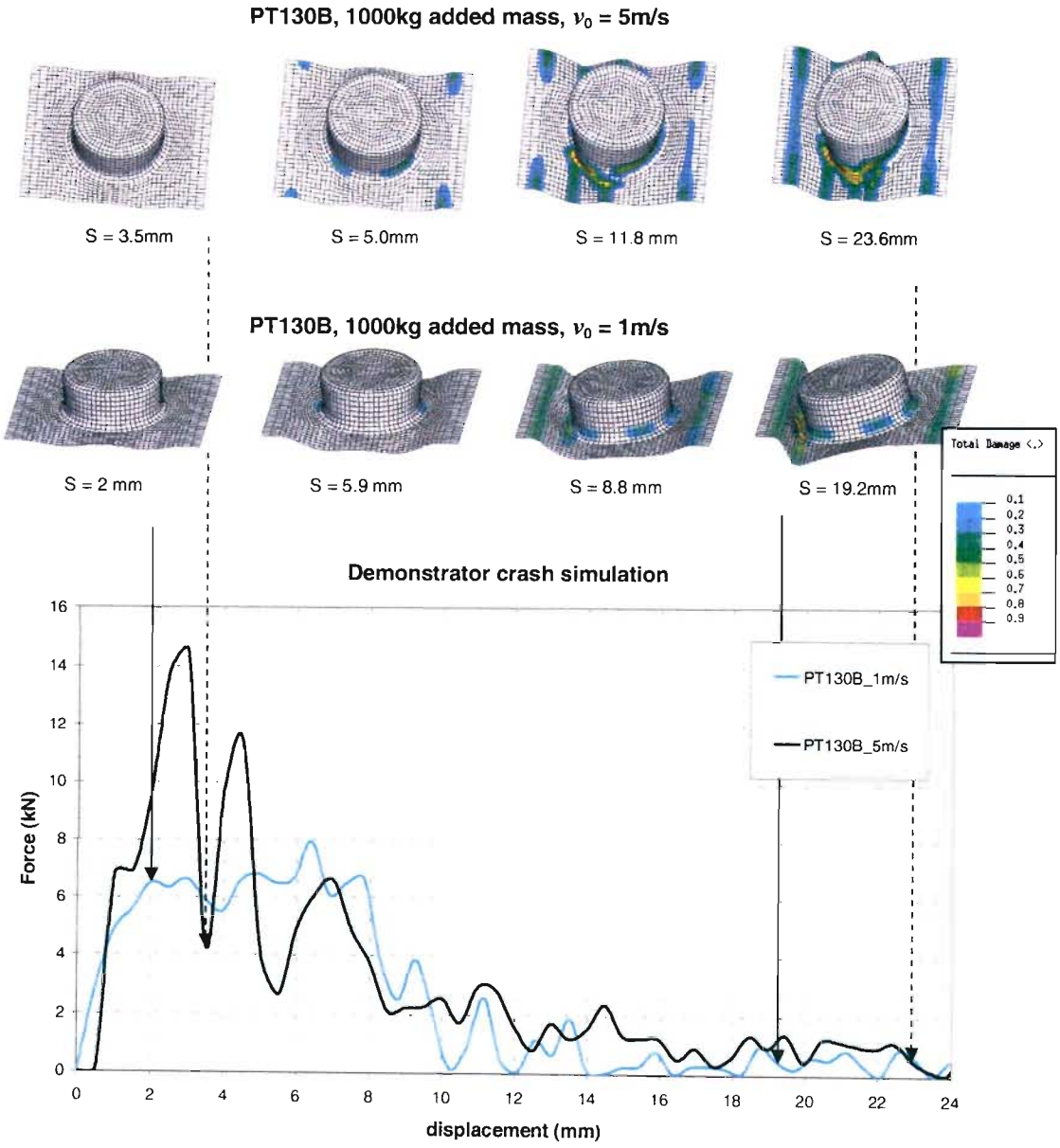

Fig. 6.2 Simulated crash response for laminated demonstrator LPT1, 1000kg added mass

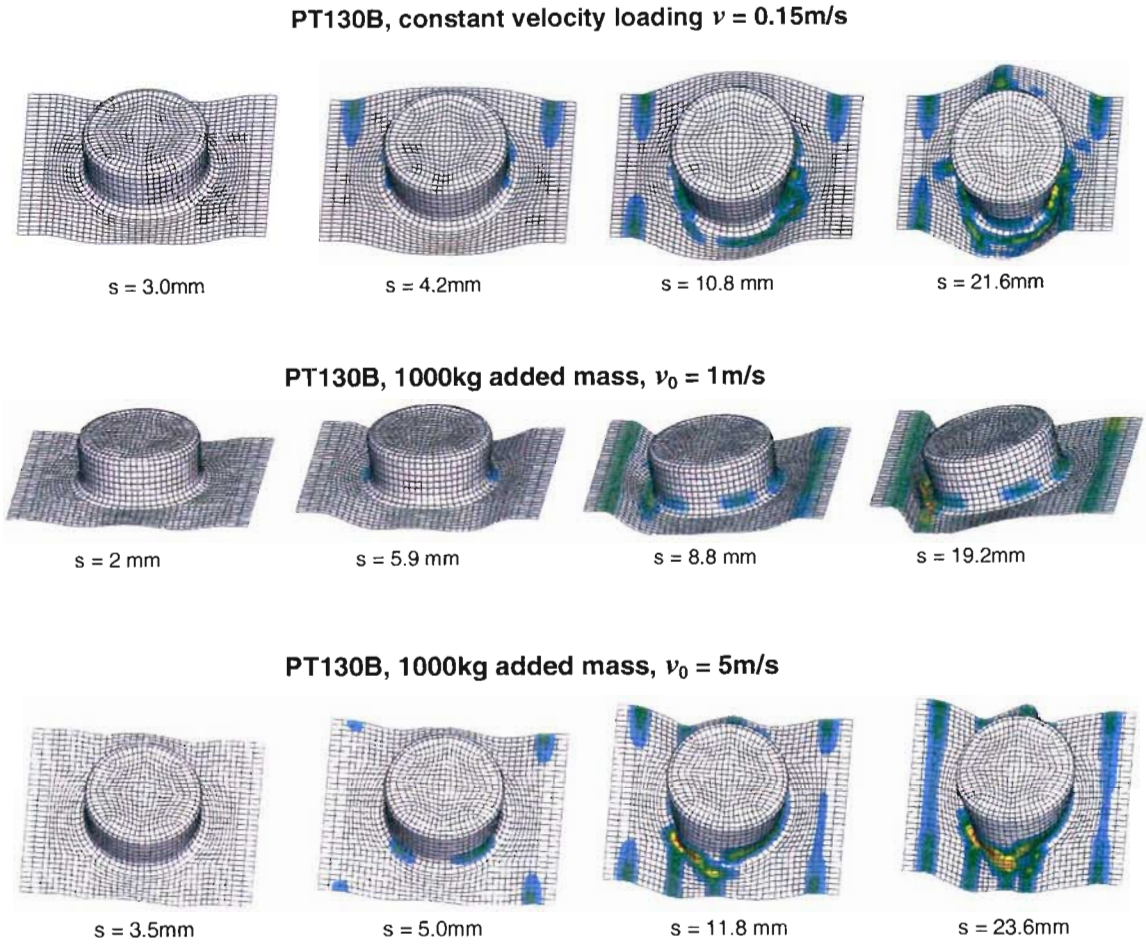

Fig. 6.3 Comparison of deformation modes with increased loading rate

6.2 Conclusions

Simulation of a thin-walled laminated component's response to a constant velocity crushing load was previously completed and experimental validation indicated high confidence in the predicted deformation modes and failure patterns for the laminated demonstrator component.

Using the same modelling methodology, the simulation of the laminated demonstrator LPT1's response to crash conditions was undertaken, employing an added mass of 1000kg with initial velocity of 1m/s and 5m/s, respectively. Simulation of the demonstrator's response to the impact loading indicates alternative deformation modes and failure patterns when compared to deformation modes and failure patterns observed through simulation of the demonstrator's response to lower velocity loading. A significant increase in the peak load (from 8kN to around 14kN) is also observed when changing from an initial velocity of 1m/s, to an initial velocity of 5m/s.

CHAPTER 7

CONCLUSIONS

Research presented herein has been aimed at developing the methodology for modelling of laminated structures' response to crushing loads. The bi-phase progressive damaging material model was adapted to the modelling of the elementary fabric reinforced ply and modelling was undertaken using the PAM-CRASH code as an analysis tool. Application of the bi-phase model to thin-walled laminates is accomplished using a multi-layered Mindlin-Reissner type shell element that allows for description of laminate layups through specification of the ply orientation with respect to a reference coordinate frame. Once the appropriate material model is selected and adequately described and understood, the modelling procedure involves the formulation of a material testing program for identification of material characterisation parameters. This was completed for the bi-phase model for material tensile and compressive characterisations (which are separately treated) and material calibration runs were implemented in order to confirm adequate material description. Further work that could result in an improvement of the material characterisation includes the testing of plate specimens in compression, as the compressive characterisation employed herein relied on the compressive testing of cylindrical specimens which are particularly suited to dynamic testing. Shear and through thickness stiffness were inferred from theory and literature, suggesting that further experimental work to characterise the material shear response could result in improved accuracy.

Development of the finite element model for the modelling of a laminated demonstrator component was completed and required a geometrical model (developed using Rhino3D) that was subsequently discretised in to a structured mesh (MSC.NASTRAN). Application of the problem boundary conditions and material description, including material layup, was required so that the FE model of the demonstrator component (completed using PAM-CRASH) could be made ready for calculation. The concurrent design and development of laminated demonstrator components with the same geometry (but different material structures) was undertaken and three separate constructions, (LPT1, LPT2 and LPT3) were tested under constant velocity crushing at loading speeds of 2.4 mm/s, 150 mm/s and 344 mm/s. The design and experimental work highlights the ability of control over fibre distribution and fibre orientation to influence the final crash response of the laminated structure. Simulation of laminated demonstrator LPT1, loaded at 150 mm/s, was undertaken and produced results showing good agreement between the components initial response, deformation modes and failure patterns recorded during component testing. The load sustained for further crushing of the demonstrator was less accurately predicted and refinement of the material characterisation process and use of alternative material models, such as the global ply model (Ladeveze and Le Dantec, 1992) and global ply model adapted for fabric plies (Johnson et al., 2001), could be used in an effort to improve the accuracy over the full range of displacement experienced during the progressive crushing process.

Extension of the work to cases involving impact (in order to have relevance for crashworthiness applications such as automotive and aeronautics virtual prototyping) required the investigation of material strain rate behaviour. Dynamic testing at a strain rate of $700s^{-1}$ indicates that the laminated material is sensitive to strain at this rate of loading, where an altered stress-strain

response was observed. Modelling of the laminated demonstrator LPT1's crash response was completed and the results from the crash simulations highlight variations in the structure's response under increased impact velocity. Alternative deformation modes and failure patterns are predicted for the different load cases (v_1 = 0.15m/s, v_2 = 1m/s, v_3 = 5m/s) and an increase in the peak load supported by the laminated demonstrator at higher loading rates is also predicted.

The modelling procedure used to simulate the response of the thin-walled laminated component has involved material characterisation, material calibration, finite element mesh development, implementation of appropriate problem boundary conditions and complete description of the material layup over the volume of the component. During the development of the FE mesh, consideration must be made of the material layup which is to be modelled. This influences the selection of separate material regions and careful choice of the finite elements' spatial orientation can aid the description of the layup. During specification of the problem boundary conditions, the classification of boundary elements by group names further aids in structuring the problem, as boundary conditions are easily applied and updated for all of the elements in the group. The meshing process employed also demonstrates how the control of mesh grading along boundary curves of individual surface segments can be used to manipulate the final structure of the finite element mesh.

The results obtained lead to the conclusion that the crash simulation methodology employed can be used as a design aid for the conception of new composite structures. Further developments could include the consideration of failure initiators and selectively reinforced structural segments during the construction of the finite element model. The investigation also shows how the bi-phase material option can be used in the PAM-CRASH code to obtain feasible solutions for the virtual prototyping of composite components that are prone to impact loading. Development of the modelling methodology has been completed to a level that produces accurate simulation of the prototype's mode of deformation under crushing and effectively predicts critical regions of failure, indicated by the onset and further development of damage in those elements of the discretised structure where failure occurs in the real component.

A paper (based on research contained herein) has been accepted for publication in the *Proceedings of the Fifteenth International Conference on Composite Materials* (2005), under the title 'Simulating the progressive crushing of fabric reinforced composite structures'.

References

Agarawal, B.D. and Broutman, L.J. (1990). *Analysis and Performance of Fiber Composites*, 2nd edition. John Wiley and Sons.

Al-Mousawi, M.M., Reid S.R. and Deans, W.F. (1997). The use of the split Hopkinson pressure bar techniques in high strain rate materials testing. *Journal of Mechanical Engineering Science*. **211** Part C, 273-292.

Belytschko, T., Lin, J.L. and Tsay, C. (1984). Explicit algorithms for the non linear dynamics of shells. *Computer Methods for Applied Mechanics and Engineering* **42**, 225-251.

Berry, J. and Hull, D. (1984). Effect of speed on progressive crushing of epoxy-glass cloth tubes. In *Mechanical Properties at High Rates of Strain* (Harding ed.). Institute of Physics Conference Series No. 70, Bristol, 1984, pp. 463-470.

Bravo, E., Larrode, E., Ullod, J. and Alba, J.J. (1993). Analysis of crash absorbing elements for automotive applications. In *Proceedings of The Ninth International Conference on Composite Materials* (ICCM-9), Vol.5, Composites Application and Design, Madrid, 1993, pp. 374-385.

Capello, F. and Nigrelli, V. (2001). Impact Response of racing-car composite nose-box. In *Eighth International Conference on Composites Engineering* (ICCE/8), (Hui ed.). Spain, 2001, pp. 109-110.

Coutellier, D. and Rozycki, P. (2000), Multi-layered multi-material finite element for crashworthiness studies. *Composites: Part A* **31**, 841 – 851.

Dehn, A., Denzer, R. and Maier, M. (1999). Crash energy absorption of fabric reinforced thermoplastic composites at elevated temperatures. In *Sixth International Conference on Composites Engineering* (ICCE/6), (Hui ed.). Orlando, Florida, 1999, pp.161-162.

Farley, G., Bird, R.K. and Modlin, J.T. (1986). The role of fiber and matrix in crash energy absorption of composite materials. In *Proceedings of the American Helicopter Society National Meeting: Crashworthy Design of Rotorcraft*, 1986.

Gray G.T. (2000). Classic Split-Hopkinson Pressure Bar Technique, *ASM Handbook Volume 8, Mechanical Testing and Evaluation*, ASM, pp. 462-476.

Gray, G.T., Blumenthal, W.R., Trujillo, C.P. and Carpenter, R.W. (1997). Influence of temperature and strain rate on the mechanical behaviour of Adiprene L-100. Journal of Physics IV **7**, 523-528.

Haug, E. and De Rouvray, A (1992). Crash response of Composite Structures. In *Structural Crashworthiness and Failure* (Jones and Wierzbicki Eds), Elsevier, Amsterdam, 1992, Chapter 7, 237-294

Hamada, H. (1997). Can braided composites be used for crushing elements in cars?. In *Proceedings of the Eleventh International Conference on Composite Materials, Vol.1, Composites Application and Design*, Australia, 1997, pp. 219-246.

Hashin, Z. (1980). Failure criteria for unidirectional fibre composites. *Journal of Applied Mechanics* **47**, 329 – 334.

Hull, D. (1983). Axial crushing of fiber reinforced composite tubes. In *Structural Crashworthiness* (Jones and Wierzbicki eds). Butterworths, London, 1983, pp. 118-135.

Johnson, A.F. and Holzapfel, M. (2002). Computational methods for predicting impact damage in engineering composite structures. In *Fifth World Congress on Computational Mechanics* (WCCM V), (Mang, Rammerstorfer and Eberhardsteiner eds.). Vienna, Austria, 2002

Johnson, A.F., Pickett, A.K. and Rozycki, P. (2001). Computational methods for predicting impact damage in composite structures. *Composites Science and Technology* **61**, 2183 – 2192.

Kaiser M.A.(1998), *Advancements in the Split Hopkinson Bar Test*, MSc Thesis, Virginia Polytechnic Institute, Blacksburg, Virginia, 1998

Ladeveze, P. and Le Dantec, E. (1992). Damage Modelling of the elementary ply for laminated composites. *Composites Science and Technology* **43**, 257 – 267.

Mamalis, A.G., Manolakos, D.E., Demosthenous G.A. and Ioannidis, M.B. (1998). *Crashworthiness of Thin-Walled Structural Components*. Technomic Publishing Company.

Morozov, K.E. (2003). *Crashworthiness Modelling of Thin-walled Composite Structures*, Doctoral Thesis, University of KwaZulu-Natal, South Africa, 2003.

Naik, N.K. (1994). *Woven Fabric Composites*. Technomic Publishing Company

Ochola, R.B., Marcus, K., Nurick, G.N. and Franz, T. (2003) Mechanical Behaviour of Glass and Carbon Fibre Reinforced Composites at Varying Strain Rates. In *Composite Structures*, 2003.

PAM-CRASH Solver Notes, 2000, Pam System International.

PAM-CRASH Theory Notes, 2000, Pam System International.

Savona, S.C., Daniel, L. and Hogg, P.J. (2001). Crash Energy Management. In *Eighth International Conference on Composites Engineering* (ICCE/8), (Hui ed.). Spain, 2001, pp. 815-816

Schmueser, D.W. and Wickliffe, L.E. (1987). Impact energy absorption of continuous fiber composite tubes. *Journal of Engineering Material Technology* **109**, 72-77.

Selvarajalu, V. (2003). *Crashworthiness Modelling of SMC Composite Materials*, Masters Thesis, University of KwaZulu-Natal, South Africa, 2003

Spotts M.F. (1964). *Mechanical Design Analysis*, Prentice-Hall, pp. 345-359.

Vasiliev, V.V. and Morozov, E.V. (2001). *Mechanics and Analysis of Composite Materials*, Elsevier, 2001.

Wu, X.J. and Gorham, D.A. (1997). Stress equilibrium in the split Hopkinson pressure bar test. *Journal of Physics IV* **7**, 91-96.

Yen, C., Cassin, T., Patterson, J. and Tripplett, M. Progressive failure analysis of thin walled composite tubes under low energy impact. *Materials Sciences Corporation publication* (www.materials-sciences.com).